

AN ABSTRACT OF THE DISSERTATION OF

Rachael D. Mueller for the degree of Doctor of Philosophy in Oceanography presented on May 16, 2014.

Title: The Effects of Thermodynamic Parameterizations, Ice Shelf Geometry, and Tides on Modeled Basal Melting of Weddell Sea Ice Shelves.

Abstract approved:

Eric D. Skyllingstad

Laurence Padman

Antarctic Ice Sheet mass balance and, hence, sea level change is affected by the floating extensions of outlet glaciers and ice streams that take up about 44% of the coastline (*Drewry et al.*, 1982) and are referred to as “ice shelves”. Ice sheet mass loss accelerates when these ice shelves lose mass through basal melting at the ice-ocean interface or calving along the ice shelf front. The focus of this dissertation is to explore the uncertainties in basal melt predictions, as affected by ocean temperatures, ocean currents, and model geometries.

Uncertainties in tidal currents and the corresponding affect on sub ice shelf basal melt was explored using the Regional Ocean Modeling System (ROMS 3.2), adapted to represent the thermodynamics of ice shelf basal melt at the ice/ocean interface. Plausible representations of present and future sub ice shelf topographies were used to explore

potential errors in tidal forcing and ocean circulation beneath the Larsen-C and Filchner-Ronne ice shelves of the Weddell Sea, Antarctica. The influence of thermal forcing and thermodynamic parameterizations was also explored.

The results presented here demonstrate that two plausible Larsen-C Ice Shelf (LCIS) topographies could yield shelf-averaged basal melt rates that differ by nearly a factor of two. The difference in these two cases is due to regional variations in tidal currents. The standard grid topography, based on realistic modern bathymetry and ice draft, supported topographic vorticity waves at diurnal frequencies in the northeast LCIS while an alternate model geometry did not. As such, these two grid topographies not only affected the shelf-averaged value of basal melting but also the regional variation in basal melting. Regional variation is important because it determines whether basal melting will have a greater impact on the rate at which ice moves off-shore, as in grounding line melt, or the rate of calving, as in melting along the ice shelf front. Out of all parameterizations, grounding line melt is shown to be largest in a commonly used parameterization that applies a uniform “friction velocity” to estimate basal melting. These model results confirm that both topographic errors and choice of thermodynamic parameterization have a significant influence on the spatial characteristic of basal melt.

In a separate study of basal melting of the much larger Filchner-Ronne Ice Shelf (FRIS), simulations shows that a future scenario of warmer ocean conditions may lead to a change in the FRIS cavity shape that strongly affects the map of tidal currents and, hence, regional characteristics of basal melting. In general, the change in FRIS cavity shape due to a warming ocean introduces a negative feedback where increased melting reduces the overall

magnitude of tidal currents (by increasing the thickness of the water column) which then results in less basal melting; however, there are large regional variations in these results. In one region, south of Henry Ice Rise, the change in cavity shape reduces basal melting from 5 m a^{-1} to 1.5 m a^{-1} due to the corresponding change in tidal forcing. In contrast, basal melting increases from 1 m a^{-1} to 1.5 m a^{-1} in the nearby region of the Institute Ice Stream outlet owing to a reduction in the upstream basal melting and, hence, cooling of inflowing water.

In summary, uncertainties in cavity geometry have a large impact on the regional characteristics of tidal current predictions and, hence, ice shelf basal melting. These uncertainties introduce significant, regional errors to ice shelf mass balance. Critical processes that influence the evolution of the Antarctic Ice Sheet cannot be accurately represented without the inclusion of small grid spacing ($\sim 1 \text{ km}$), accurate topography, and tidal forcing in the predictions of ice shelf basal melt.

©Copyright by Rachael D. Mueller

May 16, 2014

All Rights Reserved

The Effects of Thermodynamic Parameterizations, Ice Shelf Geometry, and Tides on
Modeled Basal Melting of Weddell Sea Ice Shelves.

by
Rachael D. Mueller

A DISSERTATION

submitted to

Oregon State University

in partial fulfillment of
the requirements for the
degree of

Doctor of Philosophy

Presented May 16, 2014
Commencement June 2014

Doctor of Philosophy dissertation of Rachael D. Mueller presented on May 16, 2014.

APPROVED:

Co-Major Professor, representing Oceanography

Co-Major Professor, representing Oceanography

Dean of the College of Earth, Ocean, and Atmospheric Sciences

Dean of the Graduate School

I understand that my dissertation will become part of the permanent collection of Oregon State University libraries. My signature below authorizes release of my dissertation to any reader upon request.

Rachael D. Mueller, Author

ACKNOWLEDGMENTS

When I arrived at Oregon State University eleven years ago, I could not have fathomed the depth of experiences that lay ahead. I started graduate school thinking that I was on a path to get a Ph.D. in physical oceanography. I couldn't anticipate that I would arrive at the end of my degree with the understanding that an acronym is the least important contribution to my life that this degree will impart. Its important, to be sure, but what is of greater value to me is what I will carry forward in the indelible imprinting of other people's influence on my life.

I had intended to offer my gratitude to these people in a simple paragraph or two in this section of my dissertation, but it didn't take long for me to realize that my gratitude can't be contained in a couple paragraphs; it needs a bit more space to breath. That is how fortunate I have been here. Some people may cross paths with a few others who forever change their perspective on the world in a meaningful and deeply appreciated way, but I have been fortunate enough over the past seven years of my Ph.D. to have had countless encounters with people who have helped me grow in unanticipated and deeply appreciated ways. This dissertation wouldn't exist without these influences, and this section of gratitude and reflections may be the most important section of my entire dissertation.

The person whom I am most grateful to for their mentoring over these past seven years is Dr. Laurence Padman. Laurie, your support and generosity—both in funding and encouraging my Ph.D.—has been unparalleled. It is because of you that I found a way to pursue my passion in polar oceanography, was able to observe the oceans around Antarctica in a way that brought my Masters thesis to life and that inspired my interest in ocean/ice-

shelf/atmosphere interactions (which I hope to carry forward), and was able to participate in workshops (WAIS, FRISP, and IGS) in which, for the first time, I finally felt a sense of belonging within a scientific community. You held out a hand, lifted me up, guided me through and offered incredible tolerance and patience as I fumbled through some aspects of development that were difficult for my own self to experience. I had no clue what I was doing when I wrote my first paper on Larsen-C basal melting, and there were times when I handed you righteously crap writing. Even so, you somehow found a will to see me through to the end and, in so doing, help me learn that...well...you were right about...oh so many things! I really admire your ability to advise so many aspects of a research problem and to bring to the table of advising a tremendous depth of knowledge that spans length scales, time scales, research methods, and both liquid and solid phases of water. I also admire your ability to remain engaged and committed through all circumstances, even the difficult ones. Thank you for not giving up on me all these many years. Your encouragement and respectful guidance will always be remembered and appreciated.

Dr. Helen Amanda Fricker, I will always appreciate your “can-do” attitude that carried with it both enthusiasm and support for my research. I really respect your ability to lift people up and to offer a full range of guidance, from affirmative to challenging. You have been an incredible role model to me in the way you advocate for women and offer an example for how to sit at a table that is largely dominated by men. I appreciate you as a role model and a mentor, as well as for all the effort that you put in with Laurie to help me work through my growing pains as a scientist and scientific writer. I am also so grateful to you for the opportunities you have extended to me to share my work at AGU

and to connect with others both in the field and beyond. Thank you for all the positive and constructive feedback that you have given to me so freely.

I am also incredibly grateful to Drs. Eric Skyllingstad, Roger Samelson, and Peter Ruggiero. Thank you, Eric, for your willingness to assume the role of my major-professor in the eleventh hour and for helping me understand that I needed to let go of what I wanted to research (in the short term) in order to sustain my ability to move forward with my degree. I appreciate all your encouragement and support. I will remember you for always bringing to the table more ideas than I could assimilate and for your enthusiasm for me to branch out and explore other areas of possibility, both in research and computing. Your door always felt open to me, and I am grateful for your willingness and ability to help guide me. Roger, you too always offered me an open door to spending time discussing details of calculations or suggestions for how to do things better. Even when you challenged my work, you seemed to do so with a sense of encouragement rather than criticism. I admire your ability to convey a sense of being on the same team together, even as you were disagreeing with or challenging my method. I always felt like you were on my side, helping me along. Lastly, to my graduate school representative, Peter, I am so grateful to you for encouraging me through difficult times and letting me know that you were available for support, should I have needed it. Thank you!

Susan Howard, Mike Dinniman, and Scott Springer were always incredibly generous with their time and support of my learning how to work with the Regional Ocean Modeling System. Susan Howard, you started me off in my learning and I am so thankful to you for all your time. You always offered your support fully, quickly, thoroughly and with a

great sense of humor. Mike Dinniman, I always felt like you were there for me, whenever I needed, and I so appreciate your overseeing my efforts and teaching me Fortran as I worked to modify of thermodynamics. The ROMS modeling community is lucky to have you be a part of it. Scott Springer, I appreciate your helping me with creating the Weddell Sea grid, my learning how to use the ESR cluster, and always being such a strong advocate/supporter of our reading group discussions. Thank you three in particular for helping me develop my abilities numerical modeling. Ben Galton-Fenzi, I also appreciate your sharing code and ideas related to the treatment of pressure.

My understanding of thermodynamics would not be nearly as accurate or as deeply rooted were it not for the email exchanges with Miles McPhee and Adrian Jenkins. Miles and Adrian, I am so grateful for your enthusiasm for teaching as you imparted to me this feeling that I could ask you two anything, and you would always respond with such generosity of spirit for helping me learn by guiding me through my intellectual fumbblings. Thank you for being so receptive and responsive to my inquiries. The time you took to offer feedback is deeply appreciated.

There were so many others to whom I am grateful as well. Dudley Chelton was incredibly gracious for providing computers, office space, his time and other resources to help support my ability to research Antarctic winds. My awesome officemates Eric Beals, Alex Jonko, Peter Gaube, and Larry O'Neill offered the best comradery and humorous exchanges that I could ask for from officemates. Thank you all! Larry O'Neill, in particular, I am very grateful all your help with the QuikSCAT wind analysis, which I carry forward with me even if it wasn't utilized in this dissertation. As for computing, Eric Beals, Tom

Leach, Chuck Sears and Bruce Marler were always responsive to my requests for help in overcoming computer roadblocks within OSU. Similarly, I appreciate the staff and scientists at ESR who helped with computer issues, paperwork or moral support. John Begenisich and Dave Carey at Earth & Space Research bailed me out countless times with my computer woes and always with good humor and incredible tolerance. Employment paperwork and logistics were made so much easier by the help of Camisa Carlson, Lance LaRowe, and Tiffany Pham. Thank you for all your efforts! I also received much appreciated support from Lori Hartline and Robert Allan in CEOAS Student programs office. I am grateful for your abilities to help guide me through and to advocate for financial support on my behalf. I am also really grateful for the NSF program “Mentoring Physical Oceanography Women to Increase Retention.” It has been so supportive to have regular opportunities for sharing support or wisdom with other women in the field. Thank you all!!!

I have also had an amazing network of family and friends. My Mom moved to Corvallis when my son was young to help me with childcare. She also drove with me through a snow storm to San Francisco so that she could care for him while I presented my research at the American Geophysical Union, and she flew with me and my son to Old Dominion so that I could work with Mike Dinniman without being away from my son for a longer period than I was willing to be at his age. Thank you for going above and beyond, Mom! Dad...you too. You both provided the financial support to help me finish and endless encouragement throughout. Your unconditional love is most appreciated. I'm also grateful to Loren Mueller for his financial support over the past few months that allowed our son and I to stay in our home while I finished my Ph.D. Thanks as well to my friends Annaliese, Joy, Tara, Brodie,

Kate, Katy, Sam, Meredith, Megan, Avie, Kim, Sandi and my awesome sister Kasia for the community and emotional support you offered over these years. I'm not sure what I would have done without you all to laugh with and keep things real!!!

Lastly, I would not be here today if it weren't for my funding sponsors. The first few years of my Ph.D. were funded by the NASA Earth and Space Science Fellowship (07-Earth07F-0095), and I've had other sources of funding by NASA over the years under grant funding to Laurie Padman. I am also grateful for Oregon State University and their generous offering of various scholarships and fellowships that helped keep me afloat throughout my studies.

The true reach of my gratitude extends beyond the words to various professors and colleagues, near and far. My path has crossed more talented scientists and supportive friends/family than I can describe. Thank you all whom I didn't mention by name but who have helped me along the way. I have been fortunate to achieve many successes and accomplishments that were made possible, in part, because of all those who helped me achieve them.

I could end my acknowledgements here and feel complete about having recognized those whom have helped me with my academic success; but doing so would impart the fallacy that my most valuable learning during my Ph.D. was academic. The truth is that the most valuable learning during my doctoral experience wasn't academic; my most valuable learning was about life itself. In particular, I learned about supporting life rather than simply doing life.

It was a lesson that was hard earned as it took my body failing me in order for me

to realize that I had habituated a practice of science that was not sustainable for my own life. Over the course of my life, I have cultivated a strong habit of willfully overpowering the needs of my body in order to overcome difficult circumstances, because I liked the reward of achievement that came with this choice. Some examples of this habit in my life included moving to Spain at fourteen to attend a Spanish-speaking public school, even though I couldn't understand the language; attending the Sea Education Association after my Freshman year of college, even though it was intended for those in their Junior/Senior year; learning to kayak on the Grand Canyon and navigated through a class 7 rapid by shouting "stroke!" as I punched through waves that were higher than my boat was long; and pursuing in Physical Oceanography in spite of my poor physics background. I was capable at taking on great challenges and overcoming them, and I liked the recognition that came with my achievements. I became nearly fluent in Spanish at fourteen and achieved mostly As and Bs on my report card, I stayed up nights on end to study at SEA because I was so enamored of the material that I thought sleep was less important, and I immersed myself in graduate school studies to the point that it only took me only one and a half years to earn my first pair of glasses. I had not yet been taught that this way of living and thinking was harmful. In fact, to the contrary, our culture and the people in my life seemed to encourage this over-doing; so it didn't occur to me that I was pre-conditioning my own future failure. When I encountered this failure, the resulting crash into fatigue was non-negotiable, unprecedented in my prior experience of living, inconvenient, unwelcome and incredibly difficult to experience.

I share this story here because I see the learning that came from this crash as being

perhaps the most important lesson of my life and a lesson that is relevant to our society at large. It wasn't one "thing", one person, or one circumstance that caused me to crash; it wasn't my fault or some one else's fault. The conditions for my crash were established by a joint effort.

Looking back on my own participation, I started to notice how often I prioritized achievement at the sacrifice of my wellbeing. I often chose "doing" over sleeping, sugar and caffeine over resting, and putting food in my mouth "on the fly" rather than sitting down at breakfast and lunch to eat the meals that are most able to fuel my day. I practiced a life that valued productivity at the expense of my longer-term wellbeing. The impact of these choices over the years compounded the problem. The less sleep I got...the more anxious I became; the more anxious I became...the less slept I got. Without knowing it, I became a functional mess of a human being. In hindsight, I can see that my thinking was clouded and scattered. I needed anti-anxiety medication to sleep and had a hard time relaxing or slowing down because practicing this skill didn't align with my belief that doing more was necessary for advancement. The more I took an honest look at my choices the more I realized that my body had given up on me only long after I had given up on it.

Unfortunately, there are certain things in life that we can't just cut and run from (like our own bodies). Sometimes, we have to bear the responsibility of our past choices (or the past choices of those who came before us) and do the work to dig ourselves out of whatever ditch we either co-created or were put in. I found myself in a ditch of fatigue facing the reality that I couldn't continue managing my responsibilities in the way that I had been. Something had to change.

Back in the days when I practiced martial arts, I used to love watching how Jackie Chan's characters practiced what Sensei Melanie Murphy taught me for self-defense: Protect what's in danger, use what's available, put it where it counts. Jackie Chan's characters championed the resourcefulness of making use of what was available to them; they never said to their opponents: "Gosh...I could really use some nunchucks right now.... Could you please wait right here while I go get some, cause I'd really like to kick your ass right now, but I just don't have the right tools on hand." No. Jackie's characters made use of their environment to pull a can of whoop ass out from whatever their environment had to offer them at the time.

In my post-crash scenario, I needed to channel my inner Jackie Chan, and I needed to pull out a can of whoop ass on my habit of neglecting life in favor of achievement. There were a few needs that had to be addressed as I considered forming new habits: I needed to be more fully engaged as mother, to cope with my fatigue, to heal my body, to tend to my relationship with my husband and to tend to myself, inclusive of my scientific self.

Once again, I brought to the table of self-reflection my scientific inquiry and curiosity: Could it be possible that my personal crash was less about my circumstances and more about how I managed my circumstances? I formed a hypothesis around creating success with new beliefs that productivity does not require sacrifice of self or family, and I decided to test this hypothesis on myself.

I had already discovered acupuncture and Qigong before my crash and had already experienced how powerful Taoist medicine was for me in overcoming my anxiety, so I opted to self-medicate with Taoist practices. I relaxed with quiet solitude and Qigong instead of

loud places and alcohol. I prioritized full, balanced, sit-down meals for breakfast and lunch and considered not only what I was eating but also how I was eating. I let go of coffee, gluten, sugar and alcohol (though these companions love me so much that they still visit at times). I embraced motherhood to the best of my ability and prioritized my relationships with my son and my husband. I also sought out people who could help me learn better productivity skills so that I could manage my life without neglect of my life.

Through this process, my brain started to think more clearly, my thoughts became less scattered, my anxiety reduced, my ability to manage life with ease increased, and I became happier. Focusing on my self-care helped me do better work (better science) and be more present as a mother and partner.

Thankfully, I had some amazing guides to help me along the way. I will forever be grateful for the guidance from Dr. Tara Rodden Robinson, Dr. Hugh Kearns (whose workshop was funded by OSU), Brodie Welch (L.Ac.), Master Liu He, and the Ling Gui School of International Healing Qigong. It is because of them that I learned the skills necessary to integrate my body into my practice of living and doing research. Tara taught me how to be in control of my work instead of allowing my work to be in control of me. Hugh Kearns offered invaluable tools for writing papers and thinking better instead of simply doing more. Brodie Welch not only introduced me to Qigong seven year ago but also offered powerful healing through acupuncture treatments. She inspired me to consider that thinking well is a whole body function. Her teachings also introduced me to Master Liu He and the Ling Gui School of International Healing Qigong, where I learned how to utilize Taoist medicine in my daily practice of living toward harmonizing my past, present

and future within my health practice. I learned that life is simply a series of preparations. Our daily activity prepares us for sleep, our sleep prepares us for our daily activity, our food prepares our blood to deliver nourishment within our body to organisms that either support our wellbeing and ability to function (in the short-term, long-term or both) or to organisms that hinder our wellbeing. In short, I learned that my internal ecosystem requires my care and attention in order to allow it to function in a way that can sustain my life.

My body is an ecosystem affected by my choices. The earth is an ecosystem affected by our choices. Could it be that how we treat one is reflected in how we manifest change in the other? If not directly, then perhaps by establishing beliefs of what to prioritize and how? We are observing the earth as objectively as possible and, yet, we cannot remove ourselves from the system we are observing. In fact, we are forcing the system as we observe it change. It's a fantastic and exciting time to be a scientist because the world is literally changing in front of our eyes; yet...somehow...we seem to be overlooking the connection between our future livability on the earth and our ability to protect our own future selves by caring for our lives in the present. We seem to be missing the connection that every time we neglect our own wellbeing, we contribute to the cultural mindset that prioritizes short-term gain over longer-term stability. There is no way we can address policy change for our global system without first addressing our cultural mindset around how we care for our own (or our offspring's) life and how we often neglect life in favor of productivity, scientific or other. If we want to make any headway with mitigating anthropogenic climate change, then we need to do best to ignore it for a little while until we are able to address our own psychology around prioritizing short-term gain. The simple truth is that if we lack

the skill of the practice of valuing life as individuals then we will certainly lack the skill of valuing life on a societal level, and we won't be able to manage any meaningful change toward mitigating anthropogenic climate change until we gain this skill.

This past January, *Science* magazine requested a 250 word contributions to answer the following question: If you had 5 extra hours per week to devote to advocacy for science, how would you use that time? My response wasn't selected for publication, so I can offer it freely here, as follows.

Clear scientific evidence shows that greenhouse gases affect climate, yet we struggle as a culture to respond to this information and reduce our greenhouse gas emissions. Many scientists that I know are frustrated by the "business as usual" mentality that favors productivity over sustainability; however, many of them continue support this mentality in their actions and words. There is too much work, too much competition, too great a need to produce papers, proposals and results to slow down and care for our own sustainability over our scientific productivity. I learned this as I was being humbled by my own limitations after my son was born. The simple act of choosing to stay in science while upholding my boundaries around caring for my own and my sons wellbeing earned me fierce criticism, both internal and external. Thankfully, I was able to find those who could teach me the skills I have needed to do life well (inclusive of science) and was dismissed by those who couldn't. Our bodies are complex ecosystems that needs our care, just as our children's are, and our culture will only be able to value sustainability together with productivity when we do. Perpetuating the mentality of needing five extra hours a week is harmful. I advocate for a system that supports us in caring for what we have, with the time we have. It's time we make our science meaningful with the way we do science.

This habit of prioritizing productivity over wellbeing isn't just my own habit; it has become our cultural habit, both within academia and beyond. We have a choice to make in science about whether we simply want to talk about this idea of caring for life on this planet or whether we want to act in a way that cares for life on this planet, inclusive of our own. Life is life, whether we are talking about life on this planet or life in our bodies.

It's okay if we don't want to make any changes to our academic system to help

support the lives of those within it (inclusive of offspring). “Business as usual” is a perfectly legitimate choice. Science has carried forward just fine under the current system and will continue to carry on just fine under the current system. Or...will it?

There are already signs that the way we do science isn't meeting the needs of our society. Currently, the timescales over which people want information is much smaller than the timescale over which scientific questions can be answered well. There appears to be a gap in understanding between what scientists know and what the general public understands because many people are choosing to get their information from social media rather than scientists. I would argue that the academic system is not only failing the people in science but it's failing the purpose of science as well, as we are currently not sufficiently meeting the communication needs of our society.

So...how do we bridge this gap? How do we integrate scientific understanding with our societal needs for information or for countering mis-information? Do we ask scientists to add onto their plate of tasks the additional task of outreach? The job of being a scientist is already demanding to the point that most academics I know either have a spouse who has been willing to manage the home or have been willing to allow for fatigue and compromise their own longer-term health and wellbeing. This system may be functional but it is not optimal; it's established on the premise that science is served best by each academic assuming various roles, even if he or she excels in one role but not as well in another role. The model is like a monoculture where each academic is his or her own entity and all these entities have a similar or the same purpose. Even though science continues to show that biodiversity is important to life on this planet, we remain committed

to this monoculture system. Perhaps it's time to embrace the lessons of biodiversity within the walls of academia.

The truth is that the questions we are facing are too big for any individual or group to solve on their own. We need to collaborate. Upholding a competitive, monoculture model is counter productive. It's time to evolve the system towards one that allows for biodiversity of skill, that relies on collaborations and that is flexible to our biological changes as we propagate life. This change will not only be good for science, it will be good for scientists. As part of this change, we can demonstrate that we actually do want women in science, inclusive of their biology and not simply their gender, by establishing clear guidelines for how funding accommodates maternity leave in all stages of career advancement so that the health and wellbeing of women, children and families are supported together with career advancement. In a biodiverse system, we might also have a strong support network and funding to help re-assimilate women back into academia, if they choose to take extended leave, so that we can break down the barriers imposed by having off-ramps in academia but no on-ramps. If there is a glass ceiling for women then it's supported both by funding and by those who use their words and actions to support the belief that we need to choose between family and career. Having more clear funding guidelines for how we, as a culture, support future life on this planet by supporting the embodiment of future life in our children is both an important and an overdue step in the direction of creating policies that support present and future life.

We need not wait, however, to start our own shift in mentality.

The most powerful leadership in the coming century is not going to be from any

single person, government or organization. *We the people* seem to keep looking for a president, policy or science to help rescue us from our problems; but, ultimately, we are the source of our problems, and they can't save us from ourselves, no matter how powerful they might be. The most powerful leadership in the coming center is not going to be externally guided. It will be the leadership of our own empowered choices in action and words that will help us individually and collectively toward overcoming our challenges. I have realized that I have my work cut out for me in offering this kind of leadership within science, and my experiences informs me that I am not alone.

To Laurie Padman, for leading me through, and

Ehren William Mueller,

for helping to show me the way.

TABLE OF CONTENTS

	<u>Page</u>
1 General Introduction	1
2 Thermodynamics	8
2.1 Background	9
2.1.1 Freezing Point	11
2.1.2 Heat and salt fluxes	12
2.1.3 Cautionary notes for modeling applications	20
2.2 Methodology	22
2.3 Parameterization comparison	23
2.4 Recommendations	25
3 Topographic grids and model setup of the Larsen-C Ice Shelf, Antarctica, using satellite remote sensing	34
3.1 Introduction	34
3.2 Derivation of ice elevation, thickness and draft grids	35
3.2.1 Ice Surface Elevation	35
3.2.2 Ice thickness and draft	38
3.3 Sub ice shelf bathymetry	39
3.4 Errors associated with model grid structure	42
3.4.1 σ -level considerations	43
3.4.2 Reynolds and Peclet error considerations	44
3.5 Activated C-preprocessing Options in our ROMS model runs	48
4 Impact of tide-topography interactions on basal melting of Larsen-C Ice Shelf, Antarctica	52
4.1 Introduction	54
4.2 Background	57
4.2.1 Tides	59
4.2.2 Larsen C Ice Shelf	61
4.3 Model Configuration	62
4.3.1 Thermodynamic forcing	63
4.3.2 Model grid and domain	66
4.3.3 Model forcing	70
4.3.4 Errors	74
4.4 Results	75
4.4.1 Tidal current distribution	75
4.4.2 Base case	77
4.4.3 Tide forcing and <i>wct</i> sensitivity	79
4.4.4 Sensitivity of w_b to ocean temperature	82
4.4.5 Basal melt relative to ice draft	82

TABLE OF CONTENTS (Continued)

	<u>Page</u>
4.4.6 Comparison of LCIS-averaged basal melt rates	83
4.4.7 Cross front exchange and ventilation	84
4.4.8 Evaluating the accuracy of our w_b predictions	86
4.4.9 Broader implications	87
4.5 Conclusions	91
5 Nonlocal effects of an evolving ice shelf topography on basal melting of the Filchner-Ronne Ice Shelf, Antarctica	109
5.1 Introduction	111
5.2 Methods	113
5.3 Results	117
5.3.1 Tidal forcing	117
5.3.2 General characteristics of basal melt	119
5.3.3 Regional melt characteristics	121
5.3.4 Regional heat flux and flow	122
5.3.5 Mass balance along flow lines	127
5.4 Discussion	131
5.4.1 Ice-shelf-averaged basal melt	132
5.4.2 Regional basal melt, with implications for ice sheet mass balance	132
5.5 Conclusions	136
6 General Conclusions	162

LIST OF FIGURES

<u>Figure</u>	<u>Page</u>
2.1 Freezing point temperature as a function of ice draft depth using the calculations of <i>Millero (1978)</i> and <i>Foldvik and Kvinge (1974)</i>	26
2.2 Meltrates calculated over a range of mixed layer velocities and temperature with $z_{ice} = -800$ m.	26
2.3 Meltrates calculated over a range of ice drafts and temperatures with $u_* = 0.02$ m s ⁻¹	27
2.4 Meltrate estimate as a function of thermal forcing ΔT for an ice draft of 500 m and friction velocity corresponding to $ \mathbf{u} = 0.28$ m s ⁻¹ ($u = v = 0.2$ m s ⁻¹).	28
2.5 Meltrate estimate as a function of ice draft $ z_{ice} $ given $T_o = -1.9^\circ\text{C}$ and friction velocity corresponding to $ \mathbf{u} = 0.28$ m s ⁻¹ ($u = v = 0.2$ m s ⁻¹).	29
3.1 Location map for Larsen C Ice Shelf showing data sources used to define model geometry and hydrography. The Bawden Ice Rise, indicated by yellow, was not included in our model geometry.	50
4.1 Location map for Larsen C Ice Shelf showing data sources used to define model geometry and hydrography. The Bawden Ice Rise, indicated by yellow, was not included in our model geometry.	95
4.2 Model geometry used in this study.	96
4.3 Characteristics of the tidal currents beneath LCIS.	97
4.4 Model run equilibrations as shown by melt rate averages for LCIS.	98
4.5 Comparison graphics of melt rate, surface current speed, water column thickness, and residual barotropic current.	99
4.6 Comparison between the 350 m and base cases wct , tidal current speed, and basal melt.	100
4.7 Melt rate (w_b) averaged over 30 days at ~ 1 year of model run time for cases (a) base, (b) 350 m (c) $K_1 + O_1$, (d) $M_2 + S_2$, (e) $\min u_{*o}$, (f) constant γ_t (see Table 4.3).	101
4.8 Melt rate comparison graphics for base case and cold case.	102
4.9 LCIS-averaged (a) and LCIS-area-integrated (b) w_b over h_{draft} bins of -1000 to -50 m in bin intervals of 50 m.	103
4.10 LCIS-averaged values for w_b from the same time interval shown in Figure 4.7.	104
4.11 Dye concentration 180 days after being “released” at model run time of 10 years with 100% concentration beneath LCIS and 0% concentration elsewhere.	105
5.1 Model domain (lower left) and insert showing important geographic references for FRIS (upper right).	143
5.2 An overview of the grid geometry adjustments between the standard and modified grids.	144

LIST OF FIGURES (Continued)

Figure	Page
5.3 Barotropic current beneath FRIS, as calculated by Equation 5.1, for (a) the standard-grid, tides-only run, time averaged over 35 days; and (b) the modified-grid.	144
5.4 Difference in barotropic currents, $\Delta U_{tide} = U_{tide}^s - U_{tide}^m$, where U_{tide}^s is the standard case current shown in Figure 5.3a and U_{tide}^m is the modified case current shown in Figure 5.3b.	145
5.5 Meltrates for the standard cold, standard warm and modified warm cases. (a) Meltrates averaged over the last year of the standard cold case, with $T_{init} = -1.9^\circ\text{C}$	145
5.6 Comparison between tidal current and melt rates for the standard case. . .	146
5.7 Comparison between tidal current and melt rates for the modified case. . .	146
5.8 Difference between year averaged melt rates of modified warm case (Figure 5.5(c)) and standard warm case(Figure 5.5(b)).	147
5.9 FRIS-averaged melt rates over model runtime, with values averaged over 30-day intervals.	148
5.10 Regionally averaged values of melt rates over time with (a) showing the locations of the regionally averaged values of melt rate for: (b) Foundation inlet, (c) Möller inlet, (d) S. Channel, (e) Institute inlet, and (f) Rutford embayment.	149
5.11 Steady state regionally averaged values, as shown in Figure 5.10, averaged over the last year.	150
5.12 Map of heat flux magnitudes across transect locations shown as solid black lines.	151
5.13 Heat flux across transects shown in Figure 5.12.	152
5.14 Heat flux normalized by transect area for transects shown in Figure 5.12. . .	152
5.15 Difference in area-normalized heat fluxes between the two cases with $T_{init} = -1.4^\circ\text{C}$ and the $T_{init} = -1.9^\circ\text{C}$ standard case, as shown in Figure 5.15. . .	153
5.16 Deviations of average temperatures from standard -1.9°C case for transects shown in Figure 5.12.	154
5.17 Average perpendicular velocities for transects shown in Figure 5.12.	155
5.18 Deviations of average perpendicular velocity (Figure 5.17) from standard -1.9°C case for transects shown in Figure 5.12.	156
5.19 Barotropic velocities (m s^{-1}) averaged over the last 12-months of model run time.	157
5.20 Map of basal ice mass loss or gain (Gt a^{-1}) with white contours showing transition from loss (green to red) and gain (blue).	157
5.21 Integrated mass loss or gain along the flow lines shown in Figure 5.20. . . .	158
5.22 Difference in integrated mass loss or gain along the flow lines shown in Figure 5.20.	159
5.23 FRIS-averaged basal melt rate comparison between this study [TS	160
5.24 Comparison of estimated basal melt to observations from the western RIS. .	161

LIST OF TABLES

<u>Table</u>	<u>Page</u>	
2.1	Parameter symbols and values referenced by various studies to describe the thermal and saline exchange coefficient.	30
2.2	Constant values used in computation of melt rates described in Section 2.3	31
2.3	An overview of the parameterization symbols that are commonly used in the literature of ice shelf and ocean exchange together with the description used in the corresponding publication.	32
4.1	Parameter definitions used in the numerical model and abbreviations adopted in this paper.	106
4.2	Amplitude (m) and phase (degrees) values for the M ₂ tidal constituent at three locations on LCIS.	106
4.3	An overview of tide forcing scenarios for the different runs shown in this paper.	107
4.4	Estimates of <i>wct</i> in meters from seismic data and an aircraft gravity survey compared to the base case bathymetry and the CATS2008a bathymetry. . .	107
5.1	Symbols definitions used throughout this chapter.	140
5.2	An overview of the five model runs presented in this paper and the name that is used to reference them throughout this paper.	141
5.3	Regional characteristics of heat flux balance for the standard case with $T_{init} = -1.9^{\circ}\text{C}$, showing: the convergence or divergence of heat [tW] across the transects shown in Figure 5.12, the net surface heat flux in the region, averaged over one year [tW], and the combined effect of these heat exchanges.	141
5.4	Same as Table 5.3 but for the standard case with $T_{init} = -1.4^{\circ}\text{C}$	141
5.5	Same as Tables 5.3 and 5.4 but for the modified case with $T_{init} = -1.4^{\circ}\text{C}$. .	141
5.6	Overview of changes (%) in transect dimensions and predicted values between the standard -1.4°C and the modified -1.4°C case.	141
5.7	Publication sources and abbreviations used in Figure 5.23.	142

Chapter 1

General Introduction

Ice sheet mass transport into the oceans can change rapidly over months to years (*De Angelis and Skvarca, 2003; Rignot et al., 2004; Scambos et al., 2004b; Rignot et al., 2008*), but these dynamics are still poorly understood. They are important because the rate of sea level change is affected by the rate at which Antarctic meteoric ice (land-formed ice) transfers its mass from grounded to floating ice. Factors that influence the rate at which Antarctic ice streams and glaciers move mass across the grounding line include ice rheology and mass balance, which is affected by melting or freezing at the ice-ocean interface. When the floating end-members of ice streams and glaciers combine to form ice shelves over the oceans, the mass gain or loss to/from these ice shelves modulates the rate of mass transfer across the grounding line: Removing mass from an ice shelf increases the stress along the grounding line and increases the rate of mass loss from the continent; to the contrary, adding mass from an ice shelf decreases the stress along the grounding line and decreases the rate of mass loss from the continent. This ability of ice shelf melting and freezing to affect the

boundary layer shear stress and, hence, flow of meteoric ice across the grounding line, is commonly referred to as the “buttressing” effect. Currently, ice shelf basal is thought to account for $1,325 \pm 235 \text{ Gt a}^{-1}$ to $1,454 \pm 174 \text{ Gt a}^{-1}$ of mass loss from the continent, compared to $1089 \pm 139 \text{ Gt a}^{-1}$ to $1,321 \pm 144 \text{ Gt a}^{-1}$ mass loss from calving (*Rignot et al.* (2013), *Depoorter et al.* (2013), respectively), demonstrating the significance of basal melt to Antarctic mass loss.

Ice shelf basal melting can occur anywhere the ice is in contact with water but the impact on glacial dynamics and melt water product differs depending on the depth and degree of basal melting. Basal melting at the grounding line is enhanced by the suppression of the freezing point due to increased pressure. Melting at the grounding line increases the net driving force offshore (*Joughin et al.*, 2010) and has the most direct influence on glacier dynamics (*Rignot and Jacobs*, 2002). It also increases the along-flow slope by thinning the seaward ice (*Little et al.*, 2012), leading to a positive feedback with melting in this region. In general, melting at the grounding line is influenced by a combination of factors, including: tidal currents (*Holland*, 2008), sub ice shelf topography (*Little et al.*, 2009), subglacial freshwater outflow (*Motyka et al.*, 2003; *Rignot et al.*, 2010; *Jenkins*, 2011), and ocean temperature. The meltwater produced from this region is the coldest and often leads to the creation of frazil ice particles in response to reduced pressure as the meltwater plume ascends in the ice shelf cavity. Melting in more shallow regions of ice shelves, away from the grounding line, also influences ice sheet dynamics but requires greater thermodynamic forcing due to the reduction in pressure. The source of this thermodynamic forcing can be supplied by either warmer ocean temperatures or surface currents that can be amplified by

a variety of processes, including tides.

Warm water ice shelves, such as Pine Island Glacier, are in regions where relatively warm (around 1°C) Circumpolar Deep Water (CDW) circulates within the cavity and enhances basal melt in flow pathways. The larger thermal forcing conditions of warm water ice shelves generate a stronger melt water plume than in cold water ice shelves. Cold water ice shelves, on the other hand, have an inflowing temperature from High Salinity Shelf Water around the surface freezing point of -1.9°C . The meltwater plume speed beneath cold water ice shelves is likely less than that beneath warm water ice shelves, introducing conditions where tidal currents have a greater impact on the spatial distribution of basal melting. Because of these differences in thermodynamic forcing, warm and cold water ice shelves are likely to respond differently to changes in atmospheric circulation, sea ice concentration, ice shelf topography, and ocean temperatures. Numerical solutions aimed at predicting ice shelf evolution (e.g. *Pollard and DeConto (2009)*) are, therefore, likely to have large errors until we are able to improve our predictive abilities of open-ocean atmospheric circulation, sea ice formation, ice shelf ventilation and tidal currents. The focus of this dissertation is the uncertainties in modeling basal melting of cold water ice shelves in the Weddell Sea.

Ice shelves in the northwest of the Weddell Sea, along the Antarctic Peninsula, have experienced warming atmospheric temperatures as the -9°C isotherm has shifted southward. This isotherm represents the lower end of the -9 to -5°C range of mean temperatures, which is considered to be a tipping point for ice shelf stability. Ice shelves in regions of mean temperatures between -9 to -5°C are subject to thinning and collapse (*Vaughan and Doake, 1996; Morris and Vaughan, 2003; Cook and Vaughan, 2010*); no ice

shelves exist in regions with annual mean temperatures above -5°C (*Morris and Vaughan, 2003*).

This observed southward shift in atmospheric warming since the mid-1960s has been attributed to a strengthening of the polar vortex (*Orr et al., 2008*). The polar vortex is enhanced by natural and anthropogenic forcings. The latter include a decrease in Antarctic stratospheric ozone and an increase in tropospheric greenhouse gases (*Thompson and Solomon, 2002; Thompson et al., 2011; Marshall et al., 2004*). A strong polar vortex is seen as a positive index of the Southern Annular Mode (SAM). The future strength of the polar vortex and, hence, SAM is uncertain because the combined effect of natural forcings, increased greenhouse gases and a recovery of Antarctic stratospheric ozone is unknown (*Thompson et al., 2011*). What is known is that a stronger polar vortex increases the strength of westerly winds across the Antarctic Peninsula, bringing warmer air temperatures over the Larsen ice shelves (located along the eastern side of the peninsula) driving the annual mean isotherm southward. This increased atmospheric warming (*Orr et al., 2008*) has coincided with an increase in ocean temperatures (*Robertson et al., 2002*), although it's unclear whether the two are directly linked. Overall, Antarctic Peninsula ice shelves have responded to these environmental changes by collapsing, reducing the size of floating meteoric ice by $28,000\text{ km}^2$ since 1950 (*Cook and Vaughan, 2010*).

The Larsen-C ice shelf (LCIS), at around $46,500\text{ km}^2$ (*Rignot et al., 2013*), is the largest remaining ice shelf on the Antarctic Peninsula and serves as a real-time environment to explore the underpinnings of how atmospheric and oceanographic changes influence ice shelf stability. It is unclear whether the primary contributor to the observed decrease in

LCIS surface height is caused by warmer atmospheric temperatures (*Holland et al.*, 2011; *Nicholls et al.*, 2012), or the ocean (*Shepherd et al.*, 2003, 2004), or both; however, either way, melting and freezing at the ice-oceans interface remains an important factor in the structure of this ice shelf and, likely, its stability (*Glasser et al.*, 2009; *Jansen et al.*, 2010). LCIS is a cold water ice shelf and HSSW is the primary source water to LCIS cavity circulation in spite of the observations of Modified Warm Deep Water (MWDW) on the continental slope (*Nicholls et al.*, 2012). The inflowing temperatures around the surface freezing point of -1.9°C preconditions the spatial distribution of basal melting beneath LCIS to be more sensitive to tidal currents. Prior this study, however, most modeling studies of the LCIS and ocean interactions neglected tides (e.g. *Holland* (2008)). The purpose of this study was to explore the effect of tidal currents on both the degree and spatial distribution of basal melting beneath LCIS.

South of the LCIS, at the most southern extent of the Weddell Sea, is the Filchner-Ronne Ice shelf (FRIS). At 438,000 km², this ice shelf is the second largest ice shelf of Antarctica (*Rignot et al.*, 2013). The sheer size of FRIS makes it efficient at converting ocean heat, via basal melting, into a super-cooled meltwater product that is then modified by sea ice formation over the continental shelf to produce Weddell Sea Deep Water, the Weddell Sea source of Antarctic Bottom Water. Similar to LCIS, the FRIS cavity is ventilated by HSSW. However, a recent modeling study by *Hellmer et al.* (2012) demonstrates that a reduction in sea ice, caused by future scenarios of warmer atmospheric temperatures, may alter the coastal current to advect less modified, hence warmer, CDW into the FRIS cavity. The authors did not explore the consequence to basal melting from this increase in ocean

temperature. The final purpose of this dissertation is to explore the impact of this warmer water within FRIS on ice shelf basal melting, ice shelf topography, and tidal forcing within the cavity.

Thermodynamic parameterizations in ice shelf and ocean numerical modeling

Rachael D. Mueller

Chapter 2

Thermodynamics

Forecasting the ocean's influence on ice sheet mass balance is important for understanding future sea level rise, but our ability to do so is limited by both observational challenges and computational constraints. One observational challenge is that the sub ice shelf environment is difficult to sample. In some areas it is simply inaccessible. This observational limitation diminishes our ability to validate numerical studies, a shortcoming that is perhaps most acute around Antarctica, where only two successful expeditions have measured the ice-ocean heat flux beneath ice shelves. *Jenkins et al.* (2010) documented measurements from a hot water bore hole through the Ronne Ice Shelf that, together with radar observations, were used to validate and tune the thermal and saline exchange coefficients to the summer conditions at this site in 2001. More recently, *Stanton et al.* (2013) calculated melt rates beneath Pine Island Glacier using observed salt flux measurements retrieved through a bore hole. These measurements help provide point-source information to validate parameterizations, which is both useful and necessary; however, we have yet to

validate the applicability of point-source data to the range of environmental conditions, both in sub ice shelf topography and ocean stratification or mixing. Understanding the limitations and assumptions of the commonly used parameterizations is imperative for accurately conveying the strengths and limitations of any given numerical analysis or prediction.

The purpose of this chapter is three-fold: (1) To give a simple overview of commonly used thermodynamic parameterizations, (2) to show how different choices in coefficient values can affect ice shelf melt rate predictions, and (3) to suggest a common language of symbols to help facilitate comparisons between studies within our community. This article is organized so as to give an overview of parameterizations in Background (Section 2.1). Contained in Section 2.1 are sub-sections on the freezing point of seawater (Section 2.1.1) and fluxes across the ice-ocean boundary (Section 2.1.2). Section 2.2 gives a brief overview of the methodology used for comparison. Sections 2.1.1, 2.1.2 and 2.2 form the basis of information that will be useful in interpreting the comparisons shown in Parameterization Comparison, Section 2.3. An additional section, Section 2.1.3, is also included in Background to offer information that may be useful for those intending to apply these parameterizations to the ice shelf environment. Prior to describing the comparisons, a brief Methodology (Section 2.2) is explained. Lastly, recommendations for nomenclature and parameterizations are given in Section 2.4.

2.1 Background

Heat exchange at the ice-ocean interface can be solved by a one-, two-, or three-equation approach with (1) the temperature at the ice shelf base, assumed to be at the

freezing point (2) the heat flux across the ice-ocean boundary, and (3) the corresponding salt flux across this boundary. The one-equation approach assumes an instantaneous adjustment of the mixed layer temperature to the freezing point temperature and circumvents the need to calculate the exchange of heat over time by means of a heat flux across the boundary. A more realistic assumption is that temperature changes gradually in response to melting and according to physical principles governing heat flux. In this two-equation approach, the temperature difference between the mixed layer temperature and at the ice shelf base establishes a thermal forcing for heat exchange while the basal ice salinity is assumed to be equivalent to the mixed layer salinity (and, hence, mixed layer salinity is unaffected by melt). An additional level of complexity is introduced by allowing the salinity of the ice shelf base to be more fresh than the mixed layer salinity such that melting introduces a freshening of the surface water. A third equation for salt flux is then introduced to solve for salinity at the ice shelf base in order to estimate melt rates.

All together, the equations for the surface freezing point (T_f), the heat flux through the surface layer (Q_o^T) and the salt flux through the surface layer (Q_o^S) are defined as:

$$T_f = f(P, S_b), \text{ or } f(P, S_o), \quad (2.1)$$

$$Q_o^T = f(T_f, T_o, \alpha_h, u_*), \quad (2.2)$$

$$Q_o^S = f(S_b, S_o, \alpha_s, u_*), \quad (2.3)$$

where P is the pressure at the ice interface, S_b is the salinity at the ice-ocean interface, S_o is the salinity within the surface mixed layer, T_f is the freezing point temperature, T_o is

the temperature of the ocean in the surface mixed layer, α_h, α_s are the thermal and saline exchange coefficients and u_* is the friction velocity. A detailed discussion of the thermal and saline exchange coefficients is given in Section 2.1.2. The nomenclature used in heat flux parameterizations is diverse in the literature. Tables 2.1 and 2.3 attempt to clarify similarities and differences in the various approaches by listing terms and usage. Section 2.1.2 further explains these differences.

2.1.1 Freezing Point

The freezing point temperature (T_f) is affected both by pressure and the salinity of the ice shelf base. A common linear representation is of the form

$$T_f = \lambda_1 S + \lambda_2 + \lambda_3 Z, \quad (2.4)$$

where S represents salinity either at the ice shelf base or in the mixed layer, depending on the parameterization choice (as discussed later), and Z represents either ice draft (z_{ice}) or pressure (P).

Two commonly cited papers for coefficient values are *Foldvik and Kvinge* (1974) and *Millero* (1978) (see, for example, *Dinniman et al.* (2007) and *Jenkins et al.* (2010)). *Foldvik and Kvinge* (1974) represented the freezing point temperature according to the interface salinity and the the depth of the ice (z_{ice}) with coefficient values of: $\lambda_1 = -5.7 \times 10^{-2} \text{C}$, $\lambda_2 = 9.39 \times 10^{-2} \text{C}$, and $\lambda_3 = -7.641 \times 10^{-4} \text{C m}^{-1}$. *Millero* (1978) represented the freezing point temperature according to pressure (P) at the ice-ocean interface with coefficient values of $\lambda_1 = -5.73 \times 10^{-2} \text{C}$, $\lambda_2 = 8.32 \times 10^{-2} \text{C}$, and $\lambda_3 = -7.53 \times 10^{-8} \text{C Pa}^{-1}$. Figure 2.1 show

that the *Millero* (1978) equation yields slightly colder values of T_f (and, hence, stronger thermal forcing). The effect of this difference in melt rate is discussed in Parameterization Comparison (Section 2.3).

2.1.2 Heat and salt fluxes

Classical turbulence theory differentiates three regions of mixing within the surface layer: the molecular sublayer, a transition log-layer, and a fully turbulent region. Assuming (a) steady state, (b) horizontal homogeneity and (c) negligible heat conductivity through the ice, the turbulent heat and salinity fluxes across these regions can be described by the turbulent exchange across the boundary and the gradient of heat and salt. The following two sections give examples of how the turbulent exchange is parameterized by reviewing the literature on laboratory- and ocean-based experiments. A third section describes modifications that are based on a numerical study and not incorporated in the results discussed here, though important to consider in model applications.

Laboratory-based parameterizations

Owen and Thomson (1963) applied standard engineering dimensional analysis to represent the turbulent exchange by a Stanton number (St), where St is a non-dimensional number representing heat transfer in turbulent flow and is typically calculated according to

$$\text{St} = \frac{\text{Nu}}{\text{RePr}} = \frac{\left(\frac{c_h L}{\kappa}\right)}{\left(\frac{uL}{\nu} \frac{c_p \mu}{\kappa}\right)}, \quad (2.5)$$

with L representing a characteristic length scale [m], c_h the heat transfer coefficient [$\text{W m}^{-2} \text{K}^{-1}$], κ is the thermal conductivity [$\text{W m}^{-1} \text{K}^{-1}$], u a velocity scale [m s^{-1}], ν is kinematic viscosity [$\text{m}^2 \text{s}^{-1}$], c_p is the specific heat [$\text{J K}^{-1} \text{kg}^{-1}$], and μ is the dynamic viscosity [$\text{kg m}^{-1} \text{s}^{-1}$]. Similar to other laboratory experiments (e.g. *Kader and Yaglom (1972)*), they assume that fluxes of heat occur through forced convection such that a temperature wall law and a temperature defect law can be applied to derive a formula for heat transfer across the molecular sublayer region. Given these assumptions, the heat flux (Q_T) across a rough surface can be parameterized by:

$$Q_T = \rho c_p (u \text{St}) (T_b - T_o) \quad (2.6)$$

where ρ is the density of the fluid, c the specific heat, u is a representative velocity (often but not necessarily u_* , depending on the usage in calculating St), T_b the temperature of the fluid at the interface, T_o the temperature of the fluid at the edge of the mixed layer, and St is defined as:

$$\text{St} = \frac{1}{\beta} \left(\frac{u_* h}{\nu} \right)^{-p} \left(\frac{\nu}{\alpha} \right)^{-r} = \frac{1}{\beta} (\text{Re})^{-p} (\text{Pr})^{-r} \quad (2.7)$$

where α is a constant for a particular roughness, $\text{Re}_* = u_* h / \nu$ is the roughness Reynolds number, with h being the characteristic thickness of the sublayer, and m, n are constants. For a purely molecular process, $m = 1/2$ and $n = 2/3$; however, *Owen and Thomson (1963)* determined that $\alpha = 0.52$, $m = 0.45$ and $n = 0.8$ best fits data from experiments in a wind tunnel and roughened pipe. A few years later, *Kader and Yaglom* published work on a

smooth surface and later on a parallel ridged surface in their 1972 and 1977 papers (*Kader and Yaglom, 1972, 1977*). They describe U_o and T_o to be the velocity and temperature at a distance from the boundary that is representative of the boundary layer flow thickness (h) and derived a different form of a non-dimensional parameter to describe heat flux across a boundary:

$$\text{St} = \frac{1}{2.12 \log\left(\frac{hu_*}{\nu}\right) + \beta(\text{roughness}) + 2.35} \quad (2.8)$$

where $\beta(\text{roughness})$ is the parameter that varies depending on surface characteristics. This form was iterated on in *Jenkins (1991)* and then again in *Jenkins and Bombosch (1995)*. *Holland and Jenkins (1999)* followed the form giving in *Jenkins and Bombosch (1995)*, who presented $\beta(\text{roughness}) = 12.5\text{Pr}^{2/3} - 11.35$.

Ocean-based parameterizations

McPhee (1983) pioneered the effort of moving beyond these laboratory estimates and developing heat flux parameterizations based on observations under a melting ice pack, in the Bering Sea. A few years later, this observational effort was expanded by comparing laboratory-based parameterizations of heat flux to those observed in the marginal ice zone within the Greenland Sea. *McPhee (1987)* developed a parameterization that addresses the observation that meltwater stabilizes the water column and reduces turbulent mixing by confining the momentum transfer to more shallow layers while reducing effective drag (see pp. 77-78 in *McPhee et al. (2008)*). By comparing various models of heat flux across the sublayer to direct observations, *McPhee et al. (1987)* found that incorporating buoyancy affects into melt rate predictions prevents over-estimating basal melt. This parameterization

incorporates an eddy viscosity that is dependent on the mixed layer stability, producing an expression for the Stanton number that has a molecular component reflective of the *Owen and Thomson* (1963) thermal exchange coefficient (Equation 2.7) and a turbulent component that is influenced by stratification:

$$\text{St} = \frac{1}{\Phi_{turb} + \Phi_{\nu}}, \quad (2.9)$$

where

$$\Phi_{\nu} = 1.57(\text{Re}_*)^{1/2}([\text{Pr}, \text{Sc}]^{2/3}), \quad (2.10)$$

$$\Phi_{turb} = \frac{1}{k} \ln \frac{u_* \xi_N \eta_*^2}{f z_0} + \frac{1}{2 \xi_N \eta_*} - \frac{1}{k}. \quad (2.11)$$

The stability parameter η_* is of the form introduced by *McPhee* (1981),

$$\eta_* = \left(1 + \frac{\xi_N u_*}{f L R_c} \right)^{-1/2}, \quad (2.12)$$

and the friction velocity is calculated according to

$$u_*^2 = C_d U^2 \quad (2.13)$$

where C_d is a dimensionless drag coefficient and U is the mixed layer velocity. The variable f [s^{-1}] represents the Coriolis parameter while the buoyancy dependence is introduced by the Obukhov length scale, L [m]. The non-dimensional constants include the Reynolds number ($\text{Re}_* = u_* z_0 / \nu$), Prandtl or Schmidt number ($[\text{Pr}, \text{Sc}] = \nu / \alpha_{t,s}$), von Karman's constant (k), the critical Richardson number ($R_c = 0.2$, below which the flow becomes

dynamically unstable and turbulent), and a dimensionless constant $\xi_N = 0.052$. In this form, the turbulent exchange is represented by the influence of friction velocity, roughness length, molecular diffusivities, and stratification-dependant stability.

Schmidt et al. (2004) simplified the above Equation 2.11 by assuming neutral conditions and setting the stability parameter $\eta_* = 1$, $f = 1 \times 10^{-4}$, $h_\nu = 0.001$, and $\nu = 1.95 \times 10^{-6}$. This simplification by *Schmidt et al.* (2004) is the thermodynamic parameterization incorporated into ROMS 3.3 such that Equation 2.11 is represented by:

$$\Phi_{turb} = 2.5 \ln \left(\frac{5300u_*^2}{|f|} \right) + 7.12 \quad (2.14)$$

In practice, the buoyancy effect is relatively small except in cases of extreme melt (*McPhee et al.*, 1987; *McPhee*, 1992), so this simplification should be appropriate for most applications.

Other sources of uncertainty in addition to the influence of stratification on turbulent mixing include the effect of drag and double diffusion under different conditions. An observational experiment in 1984 called MIZEX attempted to address this uncertainty (*McPhee*, 1992). Prior to this experiment, the thinking was that the spatially variable surface roughness of sea ice introduced variations in turbulence and, hence, heat exchange. A surprising result from *McPhee* (1992), however, was that the thickness of the transition layer z_0 (as in the *Kader and Yaglom* (1972) parameterization) remained the same despite a five fold difference in the surface roughness, demonstrating that the sensitivity of thermal forcing to surface roughness isn't as strong as once thought. Figure 6.5 of *McPhee et al.* (2008) shows the relationship between observed Re_* and α_h dependence over these five ex-

periments. Contradictory to laboratory results, α_h remains nearly constant, with a value of ~ 0.0057 , in spite of the changes in Re_* . This weak relationship of α_h on Re_* leads to the conclusion that the roughness scale z_0 doesn't affect scalar fluxes beyond its role in establishing the overall turbulent stress (McPhee, pers. com., 6/8/2009). If Re_* is not important to the scale of α_h then the functional form of Φ_ν for heat (salt) exchange can be represented by the Prandtl (Schmidt) number alone, i.e. $\Phi_\nu \propto \text{Pr}(\propto \text{Sc})$, and the influence of molecular diffusivities has a more prominent effect than previously suspected.

The conclusion that molecular diffusivities may be more important than surface roughness motivates the distinction that the molecular diffusivities of heat and salt fluxes respond differently to the ice-ocean boundary than molecular momentum flux. This difference is because the momentum boundary remains hydraulically rough down to $\text{Re}_* \sim < 10$ such that the momentum boundary layer is unaffected by the molecular, viscous sub-layer. The thermal and saline boundaries, on the other hand, appear to be strongly affected by molecular, double diffusive properties (McPhee *et al.*, 1987). Sirevaag (2009) compares heat flux calculations using a bulk formulation of St versus one that depends on double diffusion and found that the bulk parameterization over-estimates melt in cases of strong thermal forcing. This result suggests that the influence of double diffusion increases with the thermal forcing (McPhee, pers. com., 6/11/2009). Our best guess to date is that one of the largest sources of error in applying these parameterizations involves the role of double diffusion and the variations of this parameter amongst different environments.

One way to represent double diffusion in the heat and salt flux calculations is to introduce a double diffusion ratio, R , that scales the salt flux by some factor of the thermal

exchange coefficient, α_h . Equation 2.6, together with the salt flux equation, can be written as follows:

$$\langle w'T' \rangle_o = \alpha_h u_* (T_b - T_o) \quad (2.15)$$

$$\langle w'S' \rangle_o = \alpha_s u_* (S_b - S_o) \quad (2.16)$$

These kinematic heat and salt flux equations are equivalent to $\langle w'T' \rangle_o = Q_T/(c_p \rho)$ and $\langle w'S' \rangle_o = Q_S/\rho$. Here, α_h is a thermal exchange coefficient. The corresponding saline exchange coefficient α_s is related to α_h by a double diffusion factor of R , such that $\alpha_s = \alpha_h/R$.

This representation of heat flux has become the standard owing to its simplicity and the observed lack of dependence of between Reynolds number and heat flux (*McPhee*, 1992). However, despite sharing a standard approach, many authors diverge in both nomenclature and values. Tables 2.1 gives an overview of various symbols used, the values given in the referenced articles, and how the value relates to others in the literature.

The most common practice to date is to represent the thermal exchange coefficient as a non-dimensional value symbolized by α_h (e.g., *McPhee* (2008)) and Γ_T (*Jenkins et al.*, 2010). Two related parameters often used to describe heat exchange include the dimensional thermal exchange velocity (γ_T , *Holland and Jenkins* (1999)) and the non-dimensional Stanton number (St). The thermal exchange velocity, γ_T (which one can consider to represent $u_* \alpha_h$, with units m s^{-1}) is typically set to a constant value (Table 2.1). The Stanton number (St, Equation 2.5) is a dimensionless number that was developed to characterize

heat transfer in a forced convective flow by relating heat transfer to the fluid’s thermal capacity. As a non-dimensional number that characterizes the strength of heat transfer, St can be (and has been) somewhat synonymous with the thermal exchange coefficients α_h and Γ_T in the parameterizations of ice-ocean exchange. The heat transfer coefficient that is typically referred to in thermodynamics, however, is a dimensional value with dimensions of $\text{Wm}^{-2}\text{K}^{-1}$ (see c_h in Equation 2.5) and is thus different from the non-dimensional heat transfer coefficient discussed in ice-ocean exchange parameterizations (e.g. α_h and Γ_T). The terminology of heat transfer coefficient is useful for describing the non-dimensional parameter used in ice-ocean exchange because there is no salinity equivalent for the non-dimensional St , so relating this parameter as the “thermal exchange coefficient” allows for an equivalent terminology of “saline exchange coefficient” in the salt flux equation. As such, the use of St has thus been to primarily distinguish the underlying assumptions of the parameterization. For example, *McPhee et al.* (2008) introduced the bulk Stanton number (St_*) to differentiate the case that assumed a two equation approach rather than a three equation approach (as described in Section 2.1). In this context, the St_* notation was used for the case where the heat exchange coefficient was calculated using the mixed layer salinity in the T_f equation (Equation 2.4) and the α_h notation was used when the salinity at the ice base was used to calculate T_f . The salinity at the ice-ocean interface is less than the salinity of the mixed layer, so St_* is necessarily less than α_h (Table 2.1). Note that *Mueller et al.* (2012) mistakenly used values of St_* in place of α_h and thus underestimated basal melt. This mistake is discussed in more detail in Section 2.3.

In summary, the largest variation among parameterizations of ice-ocean exchange

is due to the representation of the thermal and saline exchange coefficients. For all intents and purposes, St is synonymous with α_h , but it can be useful to use different nomenclature in order to highlight different assumptions amongst parameterizations.

Model-based modifications

All of the equations mentioned thus far assume that the ice is a material surface where heat and salt diffuses across the boundary with no meltwater advection. (*Jenkins et al.*, 2001) identified an error in the form of a drift in temperature and salinity when applying this assumption of a material surface to numerical modeling applications where seawater undergoes a succession of melt-freeze cycles. They correct for this numerical drift by introducing an advection term to the thermal exchange velocity such that $\gamma_{eff} = \gamma_{T,S} + \partial h / \partial t$ where $\partial h / \partial t$ [m/s] is the rate of basal melt or freeze (*Jenkins et al.*, 2001).

2.1.3 Cautionary notes for modeling applications

It is often assumed that is necessary in applying any of these parameterizations to the ice shelf environment is that the ice-ocean exchange beneath sea ice is thermodynamically equivalent to ice-ocean exchange beneath ice shelves, but differences in the two scenarios are non-trivial. First, ice shelves are composed of meteoric ice that begins with zero salinity and only gains salt in special circumstances in which ocean water forms marine ice layers. Sea-ice forms in the ocean and has a non-zero salinity, creating differences in salt flux and buoyancy flux between the two cases. Second, ice shelves are the upper boundary of an underwater cavern that generally slopes upward from the grounding line to the ice shelf front, while sea ice floats in an orientation that is more or less perpendicular

to the gravitational force, with comparatively small areas of sloped surfaced introduced by pressure ridges and keels; the result of the sloping ice shelf base is a buoyancy-driven thermohaline circulation that advects ocean water towards the ice shelf base as the meltwater plume ascends the sloping ice shelf base. Third, the sub ice shelf environment is more isolated from wind forced turbulent mixing than the environment below sea ice. Lastly, the thickness of ice shelves are of order 1000 m and are subject to crevasses and—in some cases—frazil deposition of ice, while sea ice is of order 1 m and is affected by pressure ridges and hummocks, creating differences in hydrodynamic roughness (McPhee, pers. comm., 6/11/09).

These environmental differences translate into dynamical differences. Below ice shelves, large-scale buoyant plumes are created by meltwater. These plumes respond to pressure changes as they ascend hundreds of meters within the water column and can re-freeze as ice platelets or by accreting onto the ice shelf base. The dynamics of the sub ice shelf plume is much more isolated from wind forcing as well. In contrast, the meltwater from sea ice already sits at most a few meters from the surface and is more affected by the background wind-driven circulation than by pressure changes.

Another consideration in applying these parameterizations in numerical models is the potential discrepancy between vertical grid resolution and the length scale assumptions of the parameterizations. The Ice Ocean Boundary Layer (IOBL) is likely to vary in thickness from place to place due to differences in stratification and mixing. Generally speaking, however, the IOBL extends $O(50)$ m below the ice and is defined as the region where water column properties are affected by the ice boundary (McPhee, pers. comm., 6/11/09). Areas

of weaker stratification have the potential for deeper boundary layers. For example, *Holland et al.* (2007) demonstrates that an IOBL meltwater plume beneath the Filchner-Ronne Ice Shelf is $O(100)$ m and ranges from 0 to ~ 200 m. It is likely that the IOBL varies both by regional characteristics and by the local influences of stratification and mixing.

Following *McPhee* (2008), his section 5.5, the IOBL can be broken down into three sub-layers: a surface layer, a mixing layer and a pycnocline. The surface layer scale is of $O(5-15)$ m and is the region where turbulent eddies sense the boundary (*McPhee*, pers. comm., 6/11/09). The surface layer is also the layer in which parameterizations have been developed to estimate the heat, salt, and momentum fluxes between the ice and the ambient ocean. As such, values for temperature, salinity and velocity are inherently assumed to be taken from the surface layer of the IOBL, yet this constraint is rarely mentioned in meso-scale modeling studies. A possible consequence of neglecting this constraint is introducing error the melt rate prediction. *Shaw et al.* (2008) show that basal melt will likely be overestimated if the modeled boundary depth is taken outside of the region where a constant sheer stress is likely to occur because the model is violating the law-of-the-wall assumption from which many parameterizations are derived.

2.2 Methodology

The four methods compared correspond to the parameterizations explained in: (a) *Mueller et al.* (2012), (b) *Mueller et al.* (2012) corrected to use *Jenkins et al.* (2010) thermal exchange coefficients, (c) *McPhee et al.* (1987), and (d) *Jenkins et al.* (2010). The corrected form of *Mueller et al.* (2012) is equivalent to using the *Jenkins et al.* (2010) parameterization

with a freezing point calculated based on *Foldvik and Kvinge (1974)* as opposed to *Millero (1978)* (see Section 2.1.1 for further explanation of this difference).

Matlab scripts were used to estimate melt rate over the same range of velocities, ice draft values and temperature. In all cases, the friction velocity was calculated according to Equation 2.13 over a range of mixed layer current speeds (U) ranging from 0 to 0.7 m s⁻¹, ice draft values range from 0 to 1500 m and mixed layer ocean temperature, T_o ranges from -2.5 to -1.5. Table 2.2 shows the values of constants used in Equations 2.11, 2.15, 2.16 and 2.4.

2.3 Parameterization comparison

The two most comparable parameterizations for melt rates as $f(T_o, U)$ and $f(T_o, z_i)$ are those of the corrected *Mueller et al. (2012)* and *Jenkins et al. (2010)* (Figures 2.2(b,c) and 2.3(b,c)). These parameterizations only differ in choice of freezing point algorithm, so their similarity is not surprising. Melt rates for the original *Mueller et al. (2012)* parameterization are shown in Figures 2.2(a) and 2.3(a) over a range of U and z_{ice} , respectively. This parameterization underpredicts melt when compared to Figures 2.2(b-d) and 2.3(b-d). This underprediction results from incorrectly applying the bulk St_* value to the case where an interfacial salinity (rather than the mixed layer salinity) was used in the calculation of T_f . Given that $T_f(S_b) > T_f(S_o)$, the assumption of $T_f(S_o)$ leads to a smaller α_h than $T_f(S_b)$ such that melt is underpredicted when $\alpha_h(S_o)$ is incorrectly used instead of $\alpha_h(S_b)$. Melt rates for the *McPhee et al. (1987)* parameterization, simplified as described in *Schmidt et al. (2004)*, are shown in Figures 2.2(c) and 2.3(c). This parameterization produces the

largest melt rates of those compared here.

Figure 2.4 compares melt rates for all four cases across a range of thermal forcing values, ΔT . Melt rates were averaged over all velocities and ice drafts, given the same thermal forcing. This figure demonstrates that the simplified *McPhee et al.* (1987) parameterization (Equation 2.14) yields melt rates that are $\sim 20\%$ larger than both the *Jenkins et al.* (2010) approach and the modified *Mueller et al.* (2012) approach. The difference in T_f used by *Jenkins et al.* (2010) and the modified *Mueller et al.* (2012) (see section 2.1.1 for details) has no appreciable affect on basal melt, as seen in Figures 2.4 and 2.5 in which the line corresponding to the *Jenkins et al.* (2010) parameterization overlays the values from of the corrected *Mueller et al.* (2012). In contrast (and as expected), the choice in α_h does have a large impact on melt predictions; changing values of α_h alone leads to a $\sim 60\%$ maximum reduction in basal melt predictions when comparing the *Mueller et al.* (2012) results to the modified *Mueller et al.* (2012) results.

The difference between parameterizations over a span of ΔT values (Figure 2.4) is similar to the differences over a span of ice draft values, z_{ice} values (Figure 2.5). In Figure 2.5, values are averaged over the ranges of temperature and velocity for any z_{ice} . Differences between parameterizations converge at ~ 200 m, which is the averaged freezing point depth corresponding to the range of temperatures from -2.5°C to -1.5°C and the range in S_b of 24.8 to 39.7. The relative differences seen for melt rates > 0 (melting) are mirrored for melt rates < 0 (freezing) such that, for example, the original *Mueller et al.* (2012) parameterization underpredicts basal freezing and melting across the full spectrum of ice drafts.

2.4 Recommendations

This chapter has shown simple comparisons of melt rates between thermodynamics parameterizations that are commonly used in the literature of ice shelf and ocean interactions. The intention of this paper is to provide an overview of the effect of this choice on model predictions of basal melting and to highlight important considerations when applying these parameterizations in numerical models. Based on these considerations, it is advised that model applications incorporate:

1. Double-diffusive thermal and haline exchange parameterization based on Equations 2.15 and 2.16;
2. $\alpha_h = 1.1 \times 10^{-2}$, $R = 35.5$ for sub ice shelf cavity applications (as in *Jenkins et al.* (2010));
3. $\alpha_h = 1.31 \times 10^{-2}$, $R = 33$ for sea-ice applications (as in *Sirevaag* (2009)).

The double-diffusive parameterization described by Equations 2.15 and 2.16 is recommended because it's computationally efficient, it will allow for ease of assimilating new and/or regional values of the thermal and haline exchange coefficients from borehole observations, and it is legitimized by the lack of dependence between the thermal exchange coefficient and Re (as discussed in Section 2.1.2).

The notation used in this paper and recommended for ease of comparisons includes: α_h and α_s for non-dimensional thermal and haline exchange coefficient, γ_T and γ_S for dimensional thermal and haline exchange velocity, and R for double diffusive factor.

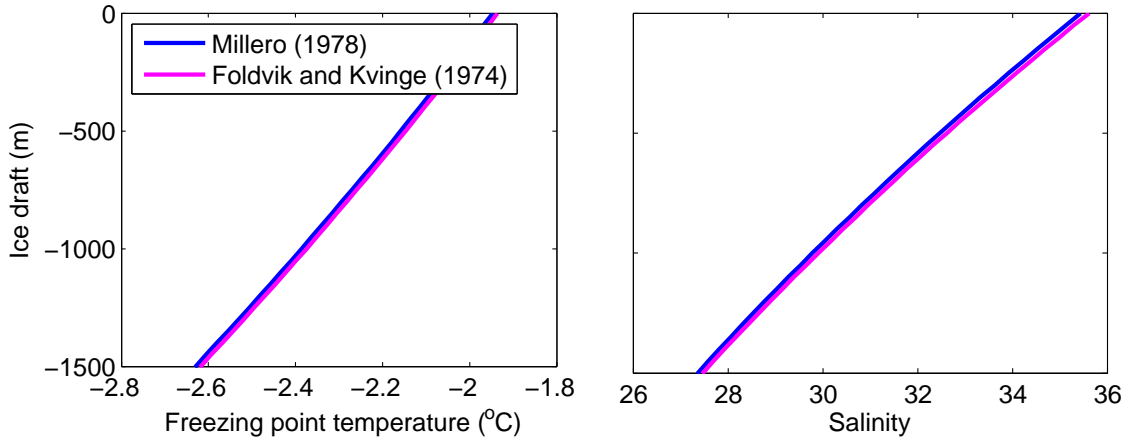


Figure 2.1: Freezing point temperature as a function of ice draft depth using the calculations of *Millero (1978)* and *Foldvik and Kvinge (1974)*. The values shown are calculated using $S_o = 34.65$, $T_o = -1.9$ °C, $u_* = 4.1 \times 10^{-3}$ m s $^{-1}$, $\alpha_h = 1.1 \times 10^{-2}$, $\alpha_s = 3.1 \times 10^{-4}$, $c_p = 3985$ J °C $^{-1}$ kg $^{-1}$, and $C_d = 9.7 \times 10^{-3}$.

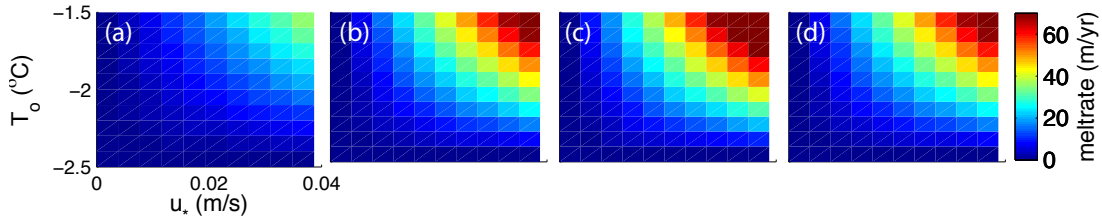


Figure 2.2: Meltrates calculated over a range of mixed layer velocities and temperature with $z_{ice} = -800$ m. For each of these four cases, the melt rates are calculated according: (a) thermodynamic parameterization and coefficients as described in (*Mueller et al., 2012*); (b) thermodynamic parameterization described in *Mueller et al. (2012)* but with thermal exchange coefficients of *Jenkins et al. (2010)*; (c) thermodynamic parameterization and coefficients described by *Schmidt et al. (2004)*; (d) thermodynamic parameterization and thermal exchange coefficients described by *Jenkins et al. (2010)*.

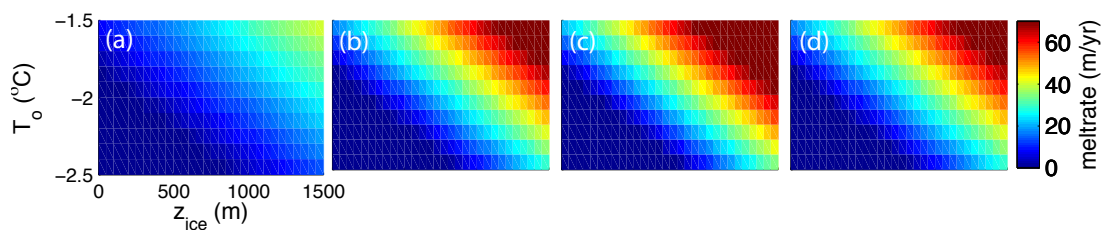


Figure 2.3: Meltrates calculated over a range of ice drafts and temperatures with $u_* = 0.02 \text{ m s}^{-1}$. Subplots (a-d) same as in Figure 2.2, showing estimates based on: (a) thermodynamic parameterization and coefficients as described in *Mueller et al. (2012)*; (b) thermodynamic parameterization described in *Mueller et al. (2012)* but with thermal exchange coefficients of *Jenkins et al. (2010)*; (c) thermodynamic parameterization and coefficients described by *Schmidt et al. (2004)*; (d) thermodynamic parameterization and thermal exchange coefficients described by *Jenkins et al. (2010)*.

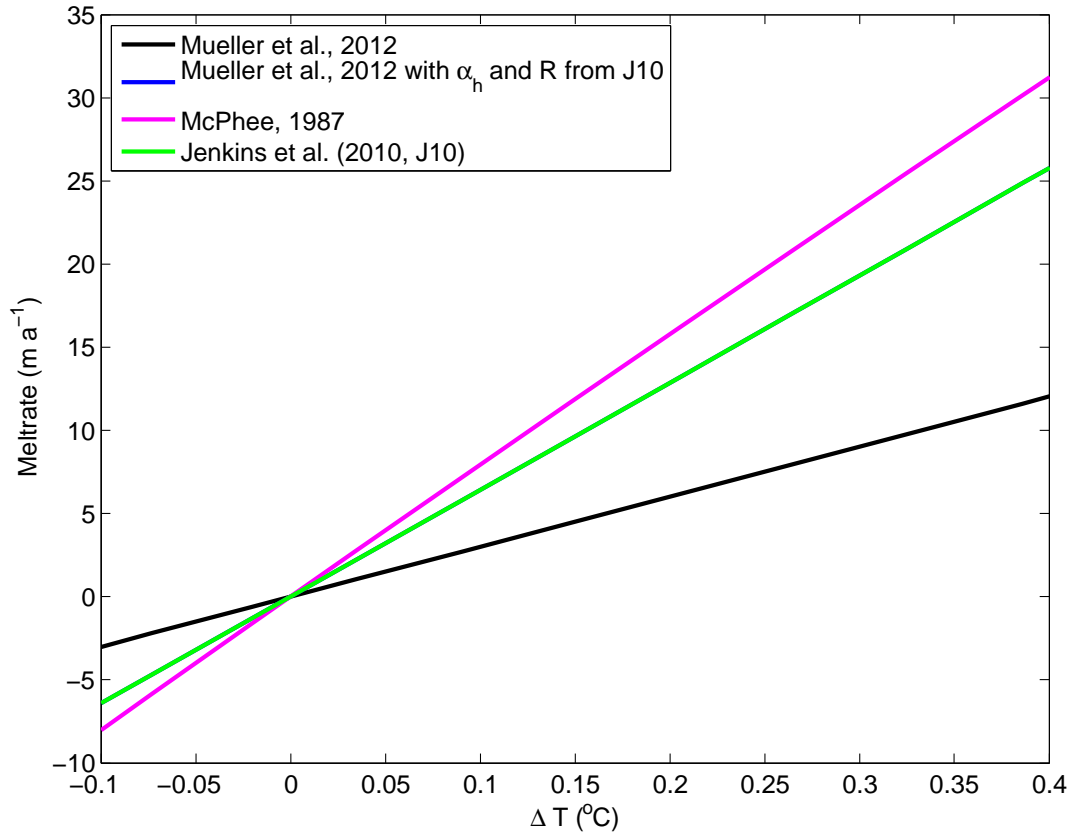


Figure 2.4: Meltrate estimate as a function of thermal forcing ΔT for an ice draft of 500 m and friction velocity corresponding to $|\mathbf{u}| = 0.28 \text{ m s}^{-1}$ ($u = v = 0.2 \text{ m s}^{-1}$). The different thermodynamic parameterizations are described in Section 2.1.2 and correspond to citations listed in the legend. The *Mueller et al.* (2012) with α_h and R from J10 is hidden by the green J10 line as the only difference between these two cases is the freezing point calculation shown in Figure 2.1 and described in Section 2.1.1.

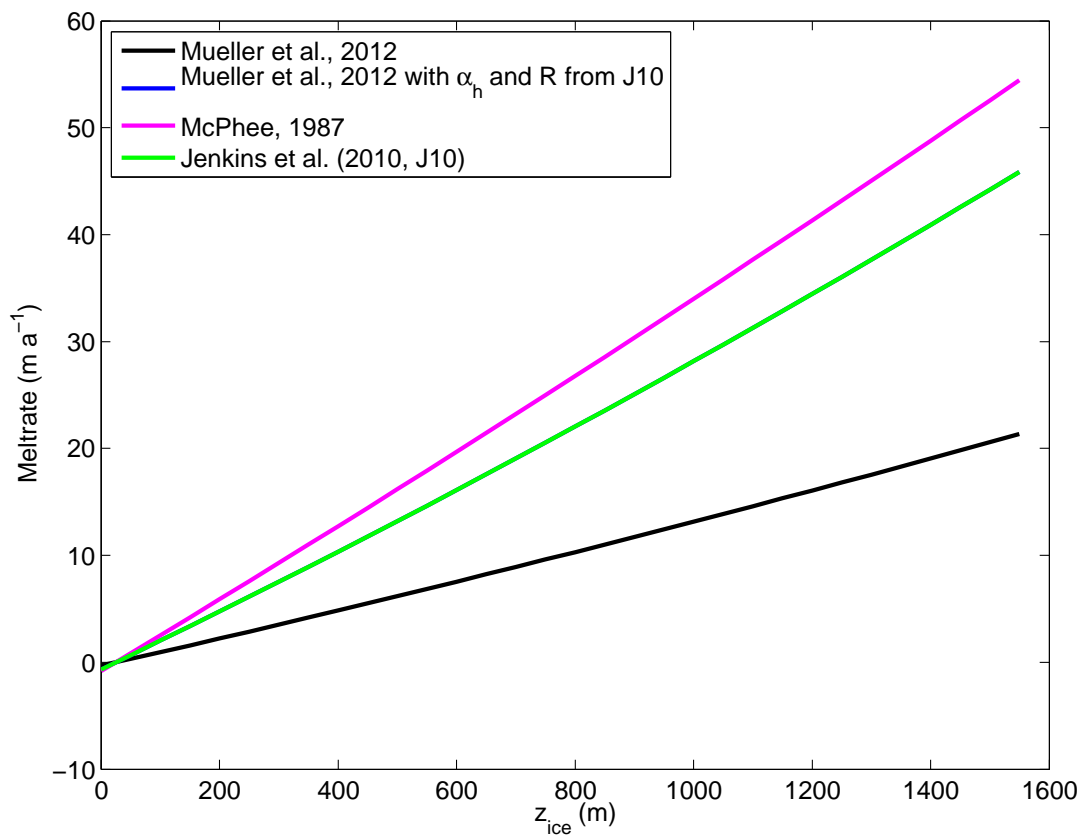


Figure 2.5: Meltrate estimate as a function of ice draft $|z_{ice}|$ given $T_o = -1.9^\circ\text{C}$ and friction velocity corresponding to $|\mathbf{u}| = 0.28 \text{ m s}^{-1}$ ($u = v = 0.2 \text{ m s}^{-1}$). The different thermodynamic parameterizations are as in Figure 2.4.

Table 2.1: Parameter symbols and values referenced by various studies to describe the thermal and saline exchange coefficient. “ $\langle \rangle$ ” indicates an averaged value over available stations. If no method is indicated then the publication is a numerical modeling study that applied the given value for the heat flux parameterization and served a purpose other than validating the heat flux parameterization. See Table 2.3 for a more specifics on the expression of thermodynamic exchange used in various studies.

Symbol	Value	Publication	method
γ_T	1×10^{-4} [m/s]	<i>Hellmer and Olbers</i> (1989)	
γ_S	5.05×10^{-7} [m/s]	<i>Grosfeld et al.</i> (1997)	
γ_T	4.2×10^{-5} [m/s]	<i>McPhee et al.</i> (2003)	Svalbard, N. Atlantic (SHEBA)
c_H	$5.7 \times 10^{-3} \pm 4.0 \times 10^{-4}$	<i>McPhee et al.</i> (1999)	Weddell Sea, Antarctica, (ANZFLUX)
$\langle St_* \rangle$	5.6×10^{-3}	<i>McPhee et al.</i> (1987), <i>McPhee</i> (1992), <i>McPhee</i> (1999)	
$\langle St_* \rangle$	$5 \times 10^{-3} - 6 \times 10^{-3}$	<i>Notz et al.</i> (2003)	Arctic (AIDJEX, SHEBA)
α_h	9.5×10^{-3}	<i>McPhee et al.</i> (2008)	Svalbard, N. Atlantic
R	30	<i>McPhee</i> (2008), ref. <i>Notz et al.</i> (2003)	Weddell Sea, Antarctica (ISPOL)
α_h	9.3×10^{-3}	<i>Sirevaag</i> (2009)	Arctic
R	35	<i>Jenkins et al.</i> (2010)	Ronne Ice Shelf, Antarctica
–	Not sufficient data	<i>Mueller et al.</i> (2012)	note: this value assumes T_f is calculated from S_o rather than S_b and was applied incorrectly here. The correct value for $T_f = f(S_b, z_{ice})$ is 1.1×10^{-2} (<i>Jenkins et al.</i> , 2010)
α_h	1.31×10^{-2}		
α_s	4.0×10^{-4}		
R	33		
Γ_T	1.1×10^{-2}		
Γ_S	3.1×10^{-4}		
R	35.5		
α_h	5×10^{-3}		
R	33	<i>Stanton et al.</i> (2013)	Pine Island Glacier Ice Shelf, Antarctica
$\langle St_* \rangle$	4.8×10^{-3}	McPhee, pers. comm., 11/16/13	

Table 2.2: Constant values used in computation of melt rates described in Section 2.3

Symbol	Value	Units	Description
ϕ	73	$^{\circ}\text{S}$	latitude
S_b	34.65		Mixed layer salinity
c_{po}	3985	$\text{J } ^{\circ}\text{C}^{-1} \text{ kg}^{-1}$	Specific heat of seawater
C_d	3×10^{-3}		Drag coefficient
L	3.34×10^{-5}	J kg^{-1}	Latent heat of freezing salt water
α_h^{J10}	1.1×10^{-2}		Thermal exchange coefficient used in <i>Jenkins et al. (2010)</i>
α_h^{M12}	5×10^{-3}		Thermal exchange coefficient used in <i>Mueller et al. (2012)</i>
R^{J10}	35.48		Double diffusive ratio used in <i>Jenkins et al. (2010)</i>
R^{M12}	33		Double diffusive ratio used in <i>Mueller et al. (2012)</i>

Table 2.3: An overview of the parameterization symbols that are commonly used in the literature of ice shelf and ocean exchange together with the description used in the corresponding publication. Units are annotated for dimensional parameters and analogous symbols referenced. See Table 2.1 for an overview of values used in these different studies.

Symbol	Description	Publication	Comments or units
B	Stanton number	<i>Owen and Thomson</i> (1963) [OT63]	
c_H	Stanton number	<i>Yaglom and Kader</i> (1974) [KY74]	
$\frac{1}{\Phi_{turb} + \Phi_{T,S}^{visc}}$	Stanton number (per <i>McPhee et al.</i> (2008))	<i>McPhee</i> (1987) [M87]	equated to B in OT63
γ_T, γ_S	thermal, saline exchange velocity	<i>Hellmer and Olbers</i> (1989)	[m/s]
γ	coefficient of turbulent heat flux	<i>Grosfeld et al.</i> (1997)	[m/s]
$\gamma_T = \frac{u_*}{2.12 \ln((u_* h / \nu) + 12.5 \text{Pr}^{2/3} - 9)}$	thermal exchange velocity	<i>Holland and Jenkins</i> (1999)	KY74 [m/s]
$\gamma_T = \frac{u_*}{\Phi_{turb} + \Phi_{T,S}^{visc}}$	thermal, saline exchange coefficient	"	M87 [m/s]
α_h, α_s	bulk Stanton number	<i>McPhee et al.</i> (2008)	$T_f = f(S_b)$
St_*	thermal, saline exchange coefficient	"	$T_f = f(S_o)$
α_h, α_s	thermal, saline exchange coefficient	<i>Notz et al.</i> (2003)	$T_f = f(S_b)$
Γ_T, Γ_S	thermal, saline exchange coefficient	<i>Jenkins et al.</i> (2010)	same as α_h, α_s
$R = \frac{\alpha_h}{\alpha_s}$	double diffusion ratio	e.g., <i>Notz et al.</i> (2003)	

Topographic grids and model setup of the Larsen-C Ice Shelf, Antarctica, using satellite
remote sensing

Rachael D. Mueller, Laurence Padman, Michael S. Dinniman, Svetlana Y. Erofeeva,
Helen A. Fricker, Matt A. King

Journal of Geophysical Research

2000 Florida Avenue N.W.

Washington, DC 20009-1277 USA

Vol. 117, C05005, 2012

Chapter 3

3.1 Introduction

Environmental and geographic constraints make it difficult to map sub-ice-shelf cavities with a high degree of spatial resolution and accuracy. At the time of this study, only two point sources were available to ground truth the seabed depth and water column thickness under Larsen C Ice Shelf (LCIS) (*Jarvis and King, 1993; Jansen et al., 2010*). The lack of spatial coverage from direct observations makes remote sensing techniques necessary for estimating both ice draft and bathymetry between the in-situ observation sites.

The purpose of this chapter is to give a background for the setup used in *Mueller et al. (2012)* (Chapter 4). Specifically, we describe the methodology used to incorporate remotely sensed observations as well as to explore other sources of uncertainty and error that arise from model parameterization choices. This supplementary online material was published together with *Mueller et al. (2012)*. We include in the following sections: a description of how we created the grids of ice elevation, thickness, and draft (Section 3.2); an overview of how we estimated seabed depth under (Section 3.3); a discussion about minimizing errors due to model grid structure (Section 3.4); and a table of C-preprocessing

options applied in our Regional Ocean Modeling System runs (Section 3.5).

3.2 Derivation of ice elevation, thickness and draft grids

3.2.1 Ice Surface Elevation

During the period late 1994 to early 1995, the geodetic mapping mission of the European Space Agency ERS-1 radar altimeter satellite operated in an 168-day repeat orbit, with along-track spacing of 335 m and across track spacing of ~ 2 km over LCIS. Elevations are provided relative to the WGS-84 ellipsoid with corrections for solid-earth, ocean and load tides already applied. However, these elevations must be corrected to a mean sea level (MSL) reference frame so that they can be converted to ice thickness through the hydrostatic assumption and assumed density profiles.

Corrected height (h_{MSL}) is obtained by:

$$h_{MSL} = h_{obs} - GE_{mt} - h_{tide} - h_{OTL} - MDT + E \quad (3.1)$$

In equation (3.1), GE_{mt} is the geoid-ellipsoid separation in the mean-tide system, h_{tide} is the tidal sea surface elevation relative to the deformable seabed, h_{OTL} is the seabed deformation due to ocean tide loading, MDT is the mean dynamic topography (discussed below) and E incorporates both unmodeled sources of surface elevation changes and radar altimeter error terms. The “mean-tide” system is one which includes the permanent luni-solar tidal deformation of the solid Earth.

The largest correction to the observed elevation is GE_{mt} . We used the EGM2008 –

WGS 84 geoid model [*Pavlis et al.* (2008), <http://cddis.nasa.gov/926/egm96/doc/S11.html> and pers. comm. N. Pavlis 5/1/2009], obtained from the U.S. National Geospatial-Intelligence Agency web site http://earth-info.nga.mil/GandG/wgs84/gravitymod/egm2008/egm08_wgs84.html. This geoid model assumes a tide free reference system. We first created a regional grid of EGM2008 in the tide free system, GE_{tf} , using the program “interp_1min.f” from the same web site. Following advice from Dr. Pavlis, we then converted GE_{tf} to a mean tide GE_{mt} reference using the following function:

$$GE_{mt} = GE_{tf} + \frac{1}{100}((1 + 0.3)[9.9 - 29.6 * \sin^2(\phi)]), \quad (3.2)$$

where ϕ is latitude. The correction term leads to a change in the geoid-ellipsoid separation of -0.23 to -0.18 m for the LCIS region.

We estimate h_{tide} (typical magnitude ~ 1 m) with the circum-Antarctic tide model CATS2008a, which is a high-resolution updated version of the data assimilation barotropic ocean tide model described by *Padman et al.* (2002). We use a load tide model based on the global tide solution TPXO7.1 (*Egbert et al.*, 1994; *Egbert and Erofeeva*, 2002) to estimate h_{OTL} (magnitude ~ 0.05 m).

After including the preceding corrections, we obtained a mean sea level elevation of -1.4 m for the open ocean seaward of the LCIS front. We attribute this elevation to MDT and error terms, the combined effect for which we correct using $MDT + E = -1.4$ m. Typical values of MDT for the Antarctic seas are -2 to -1 m, according to EGM2008 (*Pavlis et al.*, 2008). More recent estimates of MDT are -1.25 m (<http://www.aviso.oceanobs.com/duacs/>) and -1.7 m (± 0.02 - 0.03 cm, using model output from

<http://ecco2.jpl.nasa.gov/products/>) for this region. E incorporates time-dependent dynamic topography (magnitude ~ 0.1 m), the inverse barometer effect (IBE; magnitude ~ 0.1 m) (*Chelton and Enfield, 1986; Padman et al., 2003*), and sea ice contamination. Neither time-dependent dynamic topography nor the IBE can be reliably modeled for this period of observation. We also note that the thermohaline circulation associated with basal melting under LCIS leads to a small gradient of MDT from the ice shelf front to its grounding line, with a total magnitude of < 0.1 m. Since these errors are small relative to MDT uncertainty, we uniformly apply a -1.4 m correction across the entire region to account for $MDT + E$ and to approximately zero the elevation values of the open ocean.

After quality control of the data, the resulting set of corrected elevations (h_{MSL}) was gridded onto a polar-stereographic 1 km x 1 km grid, using an octant search method to smooth the anisotropic data sets resulting from high along-track sampling but relatively coarse track-to-track spacing. The octant search looks in each 45° octant around the gridding point to develop a single weighted value for each octant, assigned to a octant-dependent mean distance from the solution node. The final value assigned to each node is a distance-weighted value based on the eight octant values. This method reduces the appearance of the ERS-1 ground tracks that persist in *Bamber and Bindshadler (1997)* and that persisted in our data after applying a more commonly used kriging method. These small perturbations are nearly imperceptible but show up in model results, presumably because of the sensitivity in meltwater advection to sub-ice-shelf topographic slopes.

3.2.2 Ice thickness and draft

In order to convert h_{MSL} to ice thickness H and ice draft (h_{draft}), we assume that the ice shelf is everywhere in local hydrostatic equilibrium so that the total mass of ice is equal to the weight of the displaced water (i.e., Archimedes Principle). The conversion requires knowledge of the density of the glacial ice, the surface snow, and the transition layer between the ice and the snow (or firn layer) where the snow that has experienced some densification but has not yet compacted into solid ice. The thickness of the firn layer around Antarctica can range from zero to >100 m (*van den Broeke et al.*, 2008) and is affected by pressure, temperature and, in regions like the LCIS, meltwater percolation. The reduced density of firn relative to the density of solid ice ρ_i is often represented as a firn density correction thickness Δh (*van den Broeke et al.*, 2008). For LCIS, Δh is likely between 0 and 15 m (*van den Broeke*, pers. comm., 2009). Uncertainties in firn depths and densities can introduce errors of tens to hundreds of meters. For example, the area-averaged h_{draft} (Section 3.2.1) derived from h_{MSL} (Section 3.2.2) is ~ 400 m for LCIS when using $\Delta h = 0$ m, but is ~ 250 m when using $\Delta h = 15$ m. The meltwater percolation contribution makes the LCIS firn density correction more difficult to estimate than for other ice shelves experiencing colder summer conditions.

Various options are available for the correction for firn density. *Holland et al.* (2009) identified a latitudinal difference between an airborne radar survey of LCIS basal elevations and the BEDMAP estimate of ice thicknesses (*Lythe et al.*, 2001), which the authors interpreted as latitudinal differences in firn compaction. The grid of ice draft h_{draft} developed by *Griggs and Bamber* (2009) used $\Delta h = 10$ m for most of the ice shelf with a

sharp gradient to zero in the north (see their Figure 1a), qualitatively similar to latitudinal gradient identified by *Holland et al.* (2009).

Our firn density correction is based on an ice density profile from the south-central LCIS (location shown in Figure 3.1 and described by *Jansen et al.* (2010)). In the vertical, we fit the observed density profile with a constant ice density of $\sim 920 \text{ kg m}^{-3}$ below a critical depth h_{crit} and a half-cosine shape to a surface density of $\sim 500 \text{ kg m}^{-3}$. Ocean density is taken to be 1027.7 kg m^{-3} , with an estimated maximum error of 0.2 kg m^{-3} , corresponding roughly to uncertainty in depth-averaged (over the draft of the ice shelf) salinity uncertainty of 0.2 psu. We varied h_{crit} linearly from 0 m at 65° S to 120 m at 70° S , fixed as constant (of 0 m or 120 m) north and south of these limits, respectively. The vertical density field can then be inverted to give ice thickness relative to h_{MSL} .

For thick ice, our representation of h_{draft} as a function of surface elevation is close to the *Holland et al.* (2009) model. However, the *Holland et al.* (2009) correction model leads to negative values of h_{draft} when applied to regions of thin ice that are found in the southern portion of LCIS and in the Larsen-D Ice Shelf. Our latitudinal correction allows for positive ice draft for these regions, which probably represent the multi-year growth of land-fast sea ice through snow accumulation.

3.3 Sub ice shelf bathymetry

Our models require a map of seabed topography relative to the ocean surface, extending from the coast and ice shelf grounding lines to the boundaries of the open-water domain. For the open water, there are few in situ depth measurements in the western

Weddell Sea south of the Larsen-B embayment (see Figure 1 in *Luckman et al. (2010)*). We therefore use an open-water bathymetry data set developed for the Circum-Antarctic Tidal Simulation model, version 2008a (CATS2008a, a modified form of *Padman et al. (2002)*), based on a combination of the GEBCO-2008 gridded bathymetry (*Hall, 2006*) and the TOPO12.1 gridded bathymetry (http://topex.ucsd.edu/marine_topo/mar_topo.html), an update to the grid derived from trackline data and inferred satellite marine gravity as described by *Smith and Sandwell (1997)*. The CATS2008a map is biased towards the smoother GEBCO-2008 product on the open-water continental shelf area east of LCIS. While we are aware of new ship track data and the presence of a shallow bank to the south of LCIS (*Luckman et al., 2010*), the CATS2008a bathymetry does not take these recent observations into account.

For regions under LCIS, we know of only two spot bathymetry measurements from seismic profiles (*Jansen et al., 2010*); see Figure 3.1 for locations. We do, however, know approximate minimum seabed depth near the ice shelf grounding line (GL), assuming that we know the location of the GL and the ice draft (h_{draft}) there. The GL location is quite well constrained by synthetic aperture radar (SAR) interferometry (InSAR) (*Rignot et al., 2011*) and interpretation of break-in-slope surface features on MODIS images (*Scambos et al., 2007*). Ice draft comes from the map developed as described in Section 3.2.2.

We seek a continuous representation of bathymetry under LCIS, connecting the variations in h_{draft} at the GL with bank and trough features in our model open-water bathymetry just east of the LCIS front. We used velocity fields derived from synthetic aperture radar interferometry (InSAR) and speckle tracking to develop approximate flow-

lines for ice flow from the GL to the ice front (flowlines shown in Figure 3.1). Velocity fields were provided to us by I. Joughin and were based on methods described by *Joughin* (2002) applied to data collected by the Japanese Space Agency’s “ALOS” SAR from 2006 to 2008. Errors computed from the local image statistics are small ($\sim 2 \text{ m a}^{-1}$), but larger errors may result from baseline errors, uncompensated tidal errors, and ionospheric effects (*Gray et al.*, 2000). While it is difficult to evaluate these errors, they should generally be $< 10 \text{ m a}^{-1}$.

For each flowline, we interpolated bathymetry H from the estimated depth at the GL (H_{GL}) to water depth H just seaward of the LCIS ice front (H_{IF}), the latter interpolated from GEBCO-2008. We did this by stepping along the flowline at one-year intervals and interpolating between these points (of order 300 m) to give along-flowline bathymetry values H_i . We used a weighting scheme as follows: $H_i = (w_1 H_{GL} + w_2 H_{IF}) / (w_1 + w_2)$, where weight $w_2 = c_w \frac{d}{dm}$ with c constant, dm the distance between the grounding line and the ice front for that flowline, d the distance from the grounding line along the flowline, and $w_1 = (dm - d) / dm$. By varying c , we can change the profile of H_i from linear to much steeper near the grounding line. A value of $c=4$ was chosen to provide satisfactory smoothness in bathymetry across the ice front without creating regions of negative wct in the sub ice shelf cavity. The resulting field of along-flowline H_i was then gridded onto a polar stereographic 1x1 km grid, consistent with the elevation and h_{draft} grids.

This approach to gridding sub ice shelf bathymetry relies on the assumption that troughs along the ice front are relict features from Last Glacial Maximum (LGM) extensions of ice streams draining catchment basins located close to their present locations. The

modern streamlines evaluated from SAR follow surface features on LCIS quite well, suggesting little change in ice flow direction during the ~ 800 years it takes for ice to flow from the GL to the modern ice front. While this is encouraging for the methodology, there is no guarantee that the actual bathymetry under LCIS looks like our map. Nevertheless, the approach provides plausible sub-ice-shelf features that suggest specific processes which might be relevant to sub-ice-shelf ocean circulation and ice/ocean interaction. Furthermore, a recently developed bathymetric grid based on airborne gravity surveys (*Cochran and Bell, 2012*) is qualitatively similar to our grid.

3.4 Errors associated with model grid structure

The use of a σ -level vertical grid coordinate and the staggered lateral (Arakawa-C) grid in ROMS leads to quite complicated requirements for model stability and general performance. The problem is exacerbated by the presence of a second sloping boundary, the base of the ice shelf. We describe our approach to addressing the well known pressure gradient errors and Reynolds and Peclet errors that are inherent to this modeling framework. Section 3.4.1 addresses the factors influencing the choice of vertical grid spacing and grid smoothing to avoid numerical flows associated with baroclinic pressure gradient errors induced by sloping σ -surfaces. Section 3.4.2 describes the methodology for choosing advection schemes and parameterizations for vertical and lateral viscosities and diffusivities to minimize growth of numerical errors at the grid scale.

3.4.1 σ -level considerations

Models based on terrain-following σ -levels require special consideration for grids that include regions of large topographic variability. Unrealistic flows may be generated as errors in horizontal, baroclinic pressure gradients caused by transforming densities on σ -levels to horizontal gradients. These spurious flows occur when the bottom slope is large (*Beckmann and Haidvogel, 1993; Haidvogel and Beckmann, 1999*) and where the change in σ -level depth between adjacent horizontal grid nodes is large compared with the distance between adjacent σ -levels (*Haney, 1991*). Building a model grid that satisfies these criteria for σ -level thickness becomes more complicated by the addition of ice shelves and the introduction of large pressure gradients along the ice shelf front. *Galton-Fenzi (2009)* shows, however, that these errors are small for the default ROMS model density-Jacobian scheme (*Shchepetkin and McWilliams, 2003*).

Building a model grid that satisfies the criteria for reducing σ -level related errors can require an increase in σ -level thickness. If the surface σ -level is used to represent the ocean mixed layer, as in this dissertation, then care must be taken to ensure that the surface σ -level thickness adheres to the thermodynamic assumptions implicit in the ice-ocean thermodynamic parameterizations. The thermodynamic exchange used in Chapter 4 is derived from a “law of the wall” assumption that utilizes ocean mixed layer properties from a depth that is within the transition log layer, between the molecular sub layer and the fully turbulent region below (*von Kármán, 1930*). The application of these parameterizations to regional modeling beneath ice shelves is still an area of active research (*McPhee et al., 2008*). Nonetheless, we make use of the available parameterizations and attempt to maintain the

integrity of their assumptions by choosing a number of σ -levels that would allow the ocean’s mixed layer variables to be within the ice-ocean boundary layer but outside of the molecular sub layer.

Observations of the ice-ocean boundary below ice shelves typically show a mixed layer of ~ 25 -50 m (*MacAyeal*, 1984; *Nicholls et al.*, 1997, 2001, 2004). This range is comparable to values from observations beneath sea ice (*McPhee and Smith*, 1976). We chose 21 levels to ensure a reasonable thickness for the surface σ -level. For our standard model runs, our minimum σ -level thickness in this region is 4 m with a maximum of 30 m; 80% of the surface level thicknesses below LCIS are in the range 5 to 20 m. For the 350 m *wct* case (see main text, Section 4.3 and Table 3), the *wct* under the ice shelf was set to a minimum value of 350 m; in this case, the range of surface level thicknesses beneath LCIS is from 11 to 22 m, with 99% of the values falling between 5 and 20 m.

To test the magnitude of these errors for our grid, we use a 14-day unforced model simulation with linear stratification representing a uniform temperature of -1.7°C and a salinity range of 34.1 to 34.25. The corresponding density gradient is representative of the final density stratification from our standard case results. Results show LCIS shelf-averaged current speeds of order $1 \times 10^{-4} \text{ m s}^{-1}$, with a maximum value along the ice shelf front of $1.7 \times 10^{-3} \text{ m s}^{-1}$. Since this circulation is much weaker than tidal currents, we assume that these errors are negligible.

3.4.2 Reynolds and Peclet error considerations

The hypothesis explored in Chapter 4 is that tides significantly change basal melt rates (w_b). Numerical modeling of this process relies on diffusion to represent unresolved

scales of mixing to predict how the dissipation of tidal kinetic energy provides a mixing source that replenishes the supply of the warm inflow water to the ice shelf base. In advection-diffusion models, in particular, a background diffusion is necessary for model stability and for the prevention of numerical flows caused by grid cell Reynolds (Re) and Peclet (Pe) errors (*Weaver and Sarachik, 1990, 1991; Sugimoto et al., 1991; Marchesiello et al., 2009*), usually characterized as a checkerboard pattern in numerical results that reflects a two grid cell computational noise mode. The magnitude of diffusion necessary for numerical stability will depend on the grid resolution and current speeds. Theoretically, preventing spurious flows in our application, with a grid resolution of $\Delta x=2$ km and current speeds ~ 0.01 m s⁻¹, would require $Pe_h = |U|\Delta x/K_h < 2$ and $Re_h = |U|\Delta x/A_h < 2$, where K_h and A_h represent horizontal eddy diffusivity and viscosity, respectively. Satisfying the Re_h grid cell error criterion for this case would require $A_h, K_h > 10$ m² s⁻¹. The values for the vertical case would be $A_z, K_z > 5 \times 10^{-5}$ m² s⁻¹ (assuming $\Delta z \sim 10$ m and $|w| \sim 1 \times 10^{-5}$ m s⁻¹).

Background diffusion can be implemented either explicitly through mixing parameterizations or implicitly through the choice of advection scheme. In general, third-order advection schemes are numerically diffusive while second- and fourth-order schemes are numerically dissipative. The ROMS default advection scheme is third-order upstream advection. Although the higher order advection schemes are thought to circumvent the Reynold's and Peclet grid cell errors, we found that these errors may persist in the higher order advection schemes. To the best of our knowledge, *Marchesiello et al. (2009)* is the only study to address this issue for the ROMS model. *Marchesiello et al. (2009)* shows cases in which

spurious mixing occurs when using third-order tracer advection, and they suggest that all diffusive-advection schemes would behave similarly for σ -coordinate models. They show that this sensitivity occurs at all grid resolutions and define different scales of diapycnal diffusion based on mesh size, bottom depth/slope, flow speed, and lateral mixing.

In this study, we utilize the ROMS 3.2 default third-order upstream scheme for horizontal advection of 3D momentum, fourth-order centered scheme for horizontal advection of tracers, and the fourth-order centered scheme for vertical advection of momentum and tracers. We tested the sensitivity of w_b (with tide forcing included) to different values of background vertical diffusion of momentum and tracers. We varied background vertical diffusion from $O(1 \times 10^{-5}) \text{ m}^2 \text{ s}^{-1}$ to $O(1 \times 10^{-3}) \text{ m}^2 \text{ s}^{-1}$ and found a relative error in w_b up to $\sim 65\%$ for model run time of 100 days. Varying horizontal viscosity from 60 to 500 $\text{m}^2 \text{ s}^{-1}$ resulted in a relative error up to 7% for the same time interval. In all cases, the choice of background diffusion and viscosity did not affect spatial pattern of w_b imposed by tidal forcing. The most significant differences between the cases of varied vertical diffusion was increased w_b in the mid-shelf region, although the magnitude of this melt still remained much lower (85% less) than the melt in the region of amplified tidal forcing. In general, increasing vertical diffusion resulted in increased w_b across the ice shelf with relatively little change to the spatial distribution of w_b and ocean circulation.

Our tests of the effects of different mixing schemes and values demonstrate that lower values of background diffusion and viscosity are sufficient to prevent spurious Re and Pe error flows. As such, for all runs described in this Chapter 4, we chose the minimum background vertical viscosity and diffusivity for numerical stability, with minimum mixing

coefficients of $A_z, K_z = 1 \times 10^{-5} \text{ m}^2 \text{ s}^{-1}$. The coefficients for the Laplacian horizontal mixing are $A_h = 5 \text{ m}^2 \text{ s}^{-1}$, and $K_h = 1 \text{ m}^2 \text{ s}^{-1}$. Note: these are minimum values only; the Mellor-Yamada 2.5 turbulence closure scheme (*Mellor and Yamada, 1974, 1982*) applied in our model runs will increase A_z and K_z as dynamic stability changes (represented by changes in the Richardson number). In general, the horizontal diffusion coefficients may be less than the values estimated above because of the geostrophic coupling between velocity and density (*Weaver and Sarachik, 1990*). Horizontal mixing is along σ -surfaces for momentum and geopotential surfaces for tracers. A complete list of the model's C-preprocessing options (referred to as "cppdefs") is provided in the following section.

3.5 Activated C-preprocessing Options in our ROMS model

runs

Activation of these C-preprocessing options is required to reproduce the results presented in Chapter 4. The complete explanation of each option is provided at <https://www.myroms.org/wiki/index.php/cppdefs.h>.

Name	Description
MCPHEE	Larsen-C realistic cavity with tide forcing
ADD_FSOBC	Adding tidal elevation to processed OBC data.
ADD_M2OBC	Adding tidal currents to processed OBC data.
ANA_BSFLUX	Analytical kinematic bottom salinity flux.
ANA_BTFLUX	Analytical kinematic bottom temperature flux.
ANA_INITIAL	Analytical initial conditions.
ANA_PASSIVE	Analytical initial conditions for inert tracers.
ANA_SMFLUX	Analytical kinematic surface momentum flux.
ANA_SSFLUX	Analytical kinematic surface salinity flux.
ANA_STFLUX	Analytical kinematic surface temperature flux.
ASSUMED_SHAPE	Using assumed-shape arrays.
AVERAGES	Writing out time-averaged fields.
AVERAGES_AKS	Writing out time-averaged vertical S-diffusion.
AVERAGES_AKT	Writing out time-averaged vertical T-diffusion.
AVERAGES_FLUXES	Writing out time-averaged surface fluxes.
CURVGRID	Orthogonal curvilinear grid.
DJ_GRADPS	Parabolic Splines density Jacobian (Shchepetkin, 2002).
DOUBLE_PRECISION	Double precision arithmetic.
EAST_FSCHAPMAN	Eastern edge, free-surface, Chapman condition.
EAST_M2FLATHER	Eastern edge, 2D momentum, Flather condition.
EAST_M3GRADIENT	Eastern edge, 3D momentum, gradient condition.
EAST_TGRADIENT	Eastern edge, tracers, gradient condition.
FLOATS	Simulated Lagrangian drifters.
ICESHELF	Include Ice Shelf Cavities.
MASKING	Land/Sea masking.
MIX_GEO_TS	Mixing of tracers along geopotential surfaces.
MIX_S_UV	Mixing of momentum along constant S-surfaces.
MPI	MPI distributed-memory configuration.
MY25_MIXING	Mellor/Yamada Level-2.5 mixing closure.
NONLINEAR	Nonlinear Model.
NONLIN_EOS	Nonlinear Equation of State for seawater.
NORTH_FSCHAPMAN	Northern edge, free-surface, Chapman condition.

NORTH_M2FLATHER	Northern edge, 2D momentum, Flather condition.
NORTH_M3GRADIENT	Northern edge, 3D momentum, gradient condition.
NORTH_TGRADIENT	Northern edge, tracers, gradient condition.
N2S2_HORAVG	Horizontal smoothing of buoyancy and shear.
PERFECT_RESTART	Processing perfect restart variables.
POWER_LAW	Power-law shape time-averaging barotropic filter.
PROFILE	Time profiling activated .
K_C4ADVECTION	Fourth-order centered differences advection of TKE fields.
RAMP_TIDES	Ramping tidal forcing for one day.
IRST_SINGLE	Double precision fields in restart NetCDF file.
SALINITY	Using salinity.
SOLVE3D	Solving 3D Primitive Equations.
SOUTH_FSCHAPMAN	Southern edge, free-surface, Chapman condition.
SOUTH_M2FLATHER	Southern edge, 2D momentum, Flather condition.
SOUTH_M3GRADIENT	Southern edge, 3D momentum, gradient condition.
SOUTH_TGRADIENT	Southern edge, tracers, gradient condition.
SPLINES	Conservative parabolic spline reconstruction.
SPHERICAL	Spherical grid configuration.
SPONGE	Enhanced horizontal mixing in the sponge areas.
SSH_TIDES	Add tidal elevation to SSH climatology.
T_PASSIVE	Advecting and diffusing inert passive tracer.
TS_C4HADVECTION	Fourth-order centered horizontal advection of tracers.
TS_C4VADVECTION	Fourth-order centered vertical advection of tracers.
TS_DIF2	Harmonic mixing of tracers.
UV_ADV	Advection of momentum.
UV_COR	Coriolis term.
UV_U3HADVECTION	Third-order upstream horizontal advection of 3D momentum.
UV_C4VADVECTION	Fourth-order centered vertical advection of momentum.
UV_QDRAG	Quadratic bottom stress.
UV_TIDES	Add tidal currents to 2D momentum climatologies.
UV_VIS2	Harmonic mixing of momentum.
VAR_RHO_2D	Variable density barotropic mode.
WESTERN_WALL	Wall boundary at Western edge.

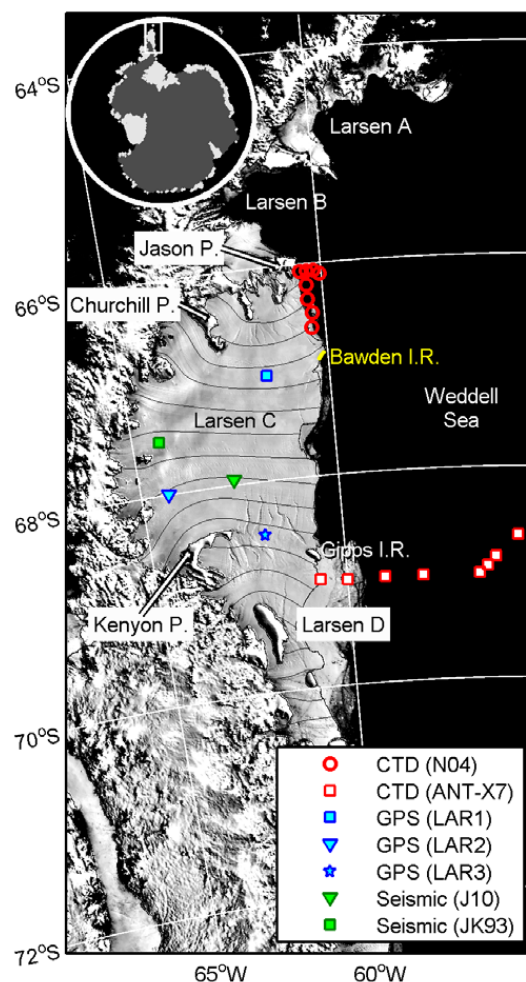


Figure 3.1: Location map for Larsen C Ice Shelf showing data sources used to define model geometry and hydrography. The Bawden Ice Rise, indicated by yellow, was not included in our model geometry. CTD stations include those reported by *Nicholls et al.* (2004) (N04) and *Bathmann et al.* (1994) (ANT-X7). GPS ice elevation data (LAR1, LAR2, LAR3) are described by *King et al.* (2011). Seismic surveys from *Jarvis and King* (1993) (JK93) and *Jansen et al.* (2010) (J10) provided local measurements of ice and firn density profiles in addition to seabed depth and water column thickness. The black flowlines on the ice shelf are based on recent interferometric synthetic aperture radar velocity measurements of ice flow (described in Section 2 of Online Supplementary Material).

Impact of tide-topography interactions on basal melting of Larsen C Ice Shelf, Antarctica

Rachael D. Mueller, Laurence Padman, Michael S. Dinniman, Svetlana Y. Erofeeva,
Helen A. Fricker, Matt A. King

Journal of Geophysical Research

2000 Florida Avenue N.W.

Washington, DC 20009-1277 USA

Vol. 117, C05005, 2012

Chapter 4

Abstract

Basal melting of ice shelves around Antarctica contributes to formation of Antarctic Bottom Water and can affect global sea level by altering the offshore flow of grounded ice streams and glaciers. Tides influence ice shelf basal melt rate (w_b) by contributing to ocean mixing and mean circulation as well as thermohaline exchanges with the ice shelf. We use a three-dimensional ocean model, thermodynamically coupled to a non-evolving ice shelf, to investigate the relationship between topography, tides, and w_b for Larsen C Ice Shelf (LCIS) in the northwestern Weddell Sea, Antarctica. Using our best estimates of ice shelf thickness and seabed topography, we find that the largest modeled LCIS melt rates occur in the northeast, where our model predicts strong diurnal tidal currents ($\sim 0.4 \text{ m s}^{-1}$). This distribution is significantly different from models with no tidal forcing, which predict largest melt rates along the deep grounding lines. We compare several model runs to explore melt rate sensitivity to geometry, initial ocean potential temperature (θ_0), thermodynamic parameterizations of heat and freshwater ice-ocean exchange, and tidal forcing. The resulting range of LCIS-averaged w_b is $\sim 0.11\text{-}0.44 \text{ m a}^{-1}$. The spatial distribution

of w_b is very sensitive to model geometry and thermodynamic parameterization while the overall magnitude of w_b is influenced by θ_0 . These sensitivities in w_b predictions reinforce a need for high-resolution maps of ice draft and sub ice shelf seabed topography together with ocean temperature measurements at the ice shelf front to improve representation of ice shelves in coupled climate system models.

4.1 Introduction

The oceans around Antarctica interact with the continental ice sheet at the floating ice shelves that occupy about 50% of its coastline (*Drewry et al.*, 1982). Melting at an ice shelf base influences global ocean properties by producing cold and low-salinity meltwater plumes that carry freshwater mass away from the continent and precondition the surrounding continental shelf waters for formation of Antarctic Bottom Water (e.g., *Jacobs* (2004)). Basal melting can also weaken an ice shelf, increasing the likelihood of calving events or disintegration (*Vieli et al.*, 2007). The balance between ice gain (by advective input of grounded ice, snow accumulation, and marine ice accretion) and loss (primarily basal melting and calving) determines the total mass balance of an ice shelf. Ice shelf stability can be compromised when the mass balance is negative. Mass loss reduces the stresses impeding the offshore flow of the ice shelves and lead to more rapid seaward ice transport in the inflowing glaciers and ice streams (*Rignot et al.*, 2004; *Scambos et al.*, 2004b). Through these processes, the ocean can affect the overall mass balance of the Antarctic ice sheet and associated global sea level on decadal time scales (*Payne et al.*, 2004).

While we have a general understanding of processes that cause ice shelf basal melting (*Lewis and Perkin*, 1986; *MacAyeal*, 1984; *Hellmer and Ollers*, 1989; *Jacobs et al.*, 1992; *Holland and Jenkins*, 1999), the ability to accurately model the spatial distribution of basal melt rate (w_b) and the associated net ice mass loss is limited by several factors, including: poorly-known ice shelf and seabed geometry, a paucity of hydrographic data defining the nature of the ocean inflow to the sub ice shelf cavity, and neglect of specific processes for the purpose of computational ease and efficiency. Models that attempt to

project land ice contribution to sea level changes over long time scales (e.g., *Pollard and DeConto* (2009)) will be subject to potentially large errors until these data and model deficiencies are resolved.

One forcing that is usually excluded in numerical models of ice shelf basal melting is tides. A relationship between tides and basal melting was postulated by *MacAyeal* (1984), who noted that the ice shelf isolates the sub ice shelf cavity from direct wind forcing and, hence, increasing the importance of tidal currents as a source of oceanic kinetic energy for conversion to mixing. More recent studies have demonstrated that tides can be a significant factor in ocean and ice shelf interactions close to the ice shelf boundaries (*Makinson and Nicholls*, 1999; *Makinson*, 2002; *Joughin and Padman*, 2003; *Holland*, 2008; *Robinson et al.*, 2010). *Makinson et al.* (2011) predicted that tides contribute approximately half of the net mass loss from Filchner-Ronne Ice Shelf (FRIS) in the southern Weddell Sea.

In this paper, we are interested in understanding basal melt sensitivity to errors in initial and boundary conditions for ice shelves where tidal forcing is significant. For this purpose, we report on sensitivity studies of the effects of adding tides to an ocean model that is thermodynamically coupled to Larsen C Ice Shelf (LCIS) in the northwestern Weddell Sea, Antarctica. This ice shelf experiences significant tidal variability (*King et al.*, 2011, in press) and is ventilated by cold, High Salinity Shelf Water (HSSW) (*Nicholls et al.*, 2004); it is similar, therefore, in some respects to the much larger FRIS studied by *Makinson et al.* (2011). The smaller size of LCIS is advantageous for studying the influence of tides in these conditions because it allows for much finer model grid resolution. The more northern location of LCIS also means that it will likely respond to climate change earlier than FRIS.

Recent lowering of the LCIS surface (*Shepherd et al.*, 2003; *Fricker and Padman*, 2012) supports the view that LCIS is undergoing changes that may lead to weakening of the ice shelf.

Atmospheric forcing and open ocean circulation clearly play important roles in ice shelf mass and elevation variability (*Fricker and Padman*, 2012), but in the present study we only force our models with tides. Our approach allows us to focus on understanding the factors contributing to uncertainty in w_b . For LCIS, relevant sources of uncertainties include: water column thickness (wct), temperature of ocean water flowing into the sub ice shelf cavity, and the parameterization of heat and freshwater exchange at the ice-ocean interface. We are particularly interested in the effect of errors in wct . Tidal currents can be very sensitive to wct errors on small spatial scales, leading to significant uncertainty in the contribution of tides to w_b . This study complements the application of a plume model to LCIS (*Holland et al.*, 2009), which provides a valuable comparison for our simulations.

We first explain the fundamentals of ice and ocean interaction in Section 4.2. Readers who are already familiar with ice-ocean interaction may proceed directly to Sections 4.2.1 and 4.2.2, which offer background information specific to tides and LCIS, respectively. Following these sections, we discuss model configuration (Section 4.3) and results from the set of simulations that we use to explore model sensitivity (Section 4.4). The conclusions (Section 4.5) first describe how these results apply to LCIS and then generalize them to all ice shelves. An Online Supplementary Document was provided with *Mueller et al.* (2012) to explain the methodology used to create the model geometry and the details of our numerical setup. We included this information in Chapter 3 of this dissertation, which describes our

estimates of ice draft, bathymetry, and our evaluation of model grid errors.

4.2 Background

A simplified characterization of sub ice shelf cavity circulation is the “ice pump” concept (*Lewis and Perkin, 1986*), in which the increased pressure at the grounding zone suppresses the in situ freezing point (T_f) of seawater, increasing the difference between ocean temperature (T_o) and T_f . This increased thermal difference fuels the melting of the meteoric ice at the grounding zone and introduces a buoyant plume of cold, fresh water that entrains ambient water as it ascends through the water column along the sloping ice shelf base. The loss of pressure as the plume rises may result in ice accretion onto the ice shelf base, thus, “pumping” ice away from the grounding zone and possibly redistributing it to the mid-shelf region. Alternatively, if the plume reaches the depth of neutral buoyancy, it can separate from the ice shelf base and/or be exported from the ice shelf cavity. By the time this plume leaves the ice shelf cavity it is estimated to contain a meltwater concentration of $\sim 0.2\text{--}2\%$, depending on the magnitude of w_b and the corresponding strength of the plume (*Mackensen, 2001; Payne et al., 2007*). Back at the grounding zone, the ascending plume is replaced by relatively unmodified, hence warmer, ocean water to maintain the thermohaline circulation.

This theoretical ice pump is often used to describe ice shelf basal melting; however, it focuses on the influence of pressure on thermal forcing, which emphasizes melt at the deep ice along the grounding zone. In reality, melting can occur at a variety of locations from the grounding zone to the ice shelf front (e.g., *Joughin and Padman (2003)*). Buoyant

meltwater plumes can extend far from their initial sources, and the characteristics of a plume will depend not only on local properties such as ice base topography and turbulent kinetic energy but also the accumulated history of the plume. The complexity of coupling local turbulent and thermodynamic processes with advection prevents an exact characterization of specific plumes.

Melting in the grounding zone is important because it tends to increase the along-flow ice surface slope and the net force driving ice offshore (*Joughin et al.*, 2010; *Little et al.*, 2012) with a direct impact on ice sheet mass balance (*Rignot and Jacobs*, 2002). Meltwater from this region is also the coldest. In addition, the grounding zone is where w_{ct} goes to zero and where fresh subglacial water will first enter the ocean upon draining from under the grounded ice. Plumes from this meltwater will reflect the details of ice base topography (*Little et al.*, 2009), tides (*Holland*, 2008), the temperature of the ambient ocean, and the depression of salinity due to inflow from subglacial freshwater. The latter dependence has been shown to be critical to basal melting near the terminus of tidewater glaciers and ice shelves (*Motyka et al.*, 2003, 2011; *Rignot et al.*, 2010; *Jenkins*, 2011).

Away from the grounding line, melting requires a greater supply of ocean heat to compensate for the smaller pressure suppression of T_f and generally weaker ice-base slopes. In some regions (e.g., the Amundsen Sea), the principal water mass ventilating the sub ice shelf cavities is Circumpolar Deep Water (CDW) whose temperature (often $> 1^\circ\text{C}$) is already much greater than T_f ; therefore, we expect that variations in CDW inflow depth and temperature have a greater influence on w_b than the pressure effect on T_f . For an ice shelf in this region, such as the floating portion of Pine Island Glacier, the associated melt

can exceed 100 m a^{-1} (*Payne et al.*, 2007; *Joughin et al.*, 2010; *Bindschadler et al.*, 2011). Basal melt may also be augmented near the ice shelf front during the summer months when the upper ocean water masses adjacent to the front become warmer and are episodically advected into the ice shelf cavity by wind forcing and tides (e.g., *Horgan et al.* (2011)).

4.2.1 Tides

Tidal height variability beneath Antarctic ice shelves is relatively easy to monitor with in situ measurements (e.g., *King et al.* (2011)) and with satellite radar and laser altimetry (e.g., *Fricker and Padman* (2002); *Padman et al.* (2008)) because the ice shelf is floating and responds immediately to surface elevation changes in the ocean. However, the more thermodynamically relevant tidal currents under ice shelves are much more difficult to measure. Only a few ocean-current time series are available from moorings deployed through holes in George VI Ice Shelf (*Potter and Paren*, 1985), FRIS (*Nicholls et al.*, 1997) and Amery Ice Shelf (*Craven et al.*, 2009). As a result, most of our understanding of tidal currents under and near ice shelves has been obtained from models.

The documented effects of tides on ice shelf basal melting are complex. Tides may intensify the entrainment of warmer water beneath the cooler boundary layer to increase w_b (*MacAyeal*, 1984), but they can also create a well-mixed region that diminishes w_b in the grounding zone, landward of a tidal front (*Holland*, 2008). Through their interactions with topography and non-tidal flows, tides can contribute to the mean circulation into and within an ice shelf cavity (*Makinson and Nicholls*, 1999). Other studies confirm the importance of tides for ice-ocean interactions on FRIS (*Makinson*, 2002) and Ross Ice Shelf (*MacAyeal*, 1985b; *Robinson et al.*, 2010). It is likely that the relatively high basal melt rates found

near the Ross Ice Shelf calving front are influenced by tidal advection of seasonally warmed near-surface water under the ice shelf in summer (*Horgan et al.*, 2011).

Tidal currents in high-latitude oceans tend to be fairly barotropic because of the weak stratification, simplifying models to the depth-averaged shallow water momentum and volume conservation equations based on *wct* (*MacAyeal*, 1984; *Robertson et al.*, 1998). However, three processes complicate prediction of the contribution of tides to the total currents influencing thermodynamic exchanges at the ice base: critical latitude effects (*Makinson et al.*, 2006; *Robertson et al.*, 2001), generation of topographic vorticity waves (TVWs, e.g., *Cartwright* (1969), *Middleton et al.* (1987) and *Padman and Kottmeier* (2000)), and rectified flows (*MacAyeal*, 1985a). For LCIS, which is several degrees away from the critical latitudes for any tidal harmonics, we regard TVWs and rectified flows as the most significant sources of uncertainty in our ability to quantify tidal currents beneath LCIS.

The mechanism that causes TVW amplification is essentially the same as for coastal-trapped waves (e.g., *Gill and Schumann* (1974)); i.e., the forced across-slope displacement stretches or shrinks the water column, resulting in a restoring force from the change in vorticity. The dispersion characteristics of TVWs in an unstratified ocean are sensitive to cross-slope topographic variation at fairly small length scales (e.g., *Middleton et al.* (1987)). For typical Antarctic conditions of a deep continental shelf (~ 500 m) adjacent to an abyssal plain, the maximum frequency of a TVW is close to diurnal and, at these frequencies, the group velocity (i.e., the speed at which energy can propagate along-slope) is close to zero. Thus, a mechanism exists to excite a TVW from the background diurnal tide, with only slow radiation of this energy away from the generation site. We will refer

to these waves as diurnal topographic vorticity waves, or DTVWs. Energetic DTVWs have been identified in data in many high latitude regions including the Arctic (*Hunkins, 1986; Padman et al., 1992*) and the Antarctic (*Middleton et al., 1987; Padman and Kottmeier, 2000*), and have been shown to increase diurnal currents by 5-10 fold off Vancouver Island (*Thomson and Crawford, 1982*). *Padman et al. (2009)* observed and modeled DTVWs at the Ross Sea shelf break, where instantaneous current speeds exceed 1 m s^{-1} . The amplitudes and phases of DTVWs along the continental slope can vary rapidly over distances comparable to the slope width (*Middleton et al., 1987*).

Tidal rectification arises through nonlinearities associated with spatial gradients in friction, mean shear, and tidal coefficients, all of which are increased in the presence of topographic gradients (*Loder, 1980; Robinson, 1981*). Rectified flows in an Eulerian frame (as would be measured at a mooring) can be of order 10% of the magnitude of the oscillatory tidal flows; the Lagrangian (particle following) mean flow can be up to $\sim 15\%$ (see *Padman et al. (1992)*). The large spatial gradients of tidal coefficients in DTVWs implies a contribution to tidal rectification (see *Padman et al. (2009)*, their Figure 10), such that we expect regions with strong DTVWs to also support a tidal contribution to mean circulation.

4.2.2 Larsen C Ice Shelf

LCIS is the largest ice shelf on the Antarctic Peninsula, with an area of $\sim 50,000 \text{ km}^2$ (*Cook and Vaughan, 2010*). During the last several decades, the Antarctic Peninsula has experienced very rapid climate change (*Comiso, 2000; Skvarca et al., 1998, 1999; Vaughan and Doake, 1996*) and significant retreat of ice shelves (*Cook and Vaughan, 2010*). Portions of LCIS have experienced recent surface lowering (*Shepherd et al., 2003; Zwally et al., 2005*;

Fricke and Padman, 2012) that may have been caused by firn compaction (*Holland et al., 2011*), accelerated basal melting (*Shepherd et al., 2003*), or both. Although LCIS is currently considered stable (*Cook and Vaughan, 2010; Jansen et al., 2010*), its stability is attributed to marine ice accretion (*Jansen et al., 2010; Khazendar et al., 2011*), which may diminish if ocean temperatures rise (*Holland et al., 2009*).

The possibility that LCIS might follow its northern neighbors and collapse within the next century (*Scambos et al., 2004a; Shepherd et al., 2003*) has motivated many recent field programs and modeling studies. Despite this activity, however, the *wct* under LCIS or even the bathymetry (D) of the open continental shelf seaward of the LCIS ice front (*Luckman et al., 2010*) is still poorly known. In addition, few hydrographic measurements exist to constrain the properties of the ocean water entering and leaving the sub ice shelf cavity. The locations of relevant hydrographic profiles are shown in Figure 4.1 and these data are described by *Bathmann et al. (1994)* and *Nicholls et al. (2004)*. Tide height ranges are significant, with the standard deviation of tide height being >1 m under LCIS (*Padman et al., 2002*); however, there are no measurements of tidal currents near LCIS, and we rely on barotropic tide models to estimate that tidal current speeds under LCIS may be large relative to the thermohaline-only plume speeds of less than ~ 0.05 m s⁻¹ (*Holland et al., 2009*).

4.3 Model Configuration

We investigate the three dimensional ocean circulation beneath LCIS using the hydrostatic, primitive equation Regional Ocean Modeling System, version 3.2 (ROMS3.2)

(*Shepetchkin and McWilliams, 2009*). ROMS3.2 incorporates a terrain following (σ) coordinate that stretches the vertical coordinate depending on wct , thus providing higher vertical resolution in the dynamically important continental shelf region including the sub ice shelf cavity. Our version of the model has been slightly modified from the repository version to include ice shelf thermodynamic forcing (described below). We summarize the model parameters and setup specifications in Table 4.1.

Efforts are presently underway to develop a frazil ice formation model for ROMS [pers. comm., B. Galton-Fenzi, 2010], but this parameterization was not available for the present study. In our study, water that is colder than the in situ freezing point will result in heat and salt fluxes that are representative of freezing onto the ice shelf base. The effect of frazil ice would be to contribute more ice crystals to freezing and to enhance the buoyancy of the meltwater plume. However, the added buoyancy-driven flow given by frazil formation is likely negligible compared to overall plume speeds [P. Holland, pers. comm., 8/11/2011; *Galton-Fenzi (2009)*]. An idealized cavity study described by *Galton-Fenzi (2009)* demonstrates a $\sim 20\%$ reduction in basal melting with the addition of frazil ice, although it is unclear how results from this idealized cavity would translate to realistic LCIS geometry.

4.3.1 Thermodynamic forcing

Thermodynamics at the interface between the ocean and ice shelf follows the three-equation approach described by Equations (1), (2) and (5) of *Holland and Jenkins (1999)*. The melt rate w_b represents a change in ice draft (h_{draft}) over time; however, h_{draft} is maintained constant throughout each run. We differ from the *Holland and Jenkins (1999)*

approach by using the scalar transfer coefficients described by *McPhee* (2008) and *Sirevaag* (2009). We also simplify Equation (2) in *Holland and Jenkins* (1999) with the assumption that the thermal conductivity within the ice shelf and the associated heat flux through the ice are negligible (i.e., the ice shelf is a perfect insulator, so that $Q_I^T = 0$). With this assumption, the kinematic heat flux (Q_o^T) and salt flux (Q_o^S) through the ocean's surface mixed layer is balanced by the thermodynamics of melting or freezing at the ice shelf base according to:

$$Q_o^T = -\frac{L}{c_{pw}}w_b, \quad (4.1)$$

$$Q_o^S = -S_b w_b, \quad (4.2)$$

where L is the latent heat of fusion, c_{pw} is the heat capacity of water, w_b is the isostatically adjusted vertical velocity at the top of the boundary layer, and S_b is the salinity at the ice-ocean interface. The value w_b is equivalent to the freshwater volume flux and is calculated from the change in ice thickness due to melt ($\frac{\partial H}{\partial t}$) as $w_b = -\frac{\rho_i}{\rho_o} \frac{\partial H}{\partial t}$, where ρ_i and ρ_o are the densities of the ice and ocean, respectively.

Both Q_o^T and Q_o^S at the ice-ocean interface are functions of the friction velocity (u_{*o}), and the salt and temperature differences between the ice-ocean interface (S_b, T_b) and the ocean's mixed layer properties (S_o, T_o):

$$Q_o^T = \alpha_h u_{*o} (T_b - T_o) \quad (4.3)$$

$$Q_o^S = \alpha_s u_{*o} (S_b - S_o) \quad (4.4)$$

Equation (4.3) introduces α_h as a thermal exchange coefficient (*McPhee*, 2008;

Sirevaag, 2009). This thermal exchange coefficient assumes the use of the interfacial salinity (S_b), rather than mixed layer salinity (S_o), to calculate the interfacial temperature (T_b). The saline exchange coefficient α_s is related to α_h by a double diffusion factor, R , such that $\alpha_s = \alpha_h/R$. At the time of this study, the available research with which to inform our choice of the double diffusion factor was from Arctic sea ice studies (e.g., *Sirevaag* (2009) and *McPhee et al.* (2008)). We chose $R = 33$ following *Sirevaag* (2009). *McPhee et al.* (2008) suggests $R = 35\text{--}70$. The actual strength of double diffusion beneath LCIS is unknown; however, observations beneath Ronne Ice Shelf (*Jenkins et al.*, 2010) suggest $R \approx 35$.

A common approach to parameterizing the surface heat and salt fluxes in Equations (4.3) and (4.4) is to represent $\alpha_h u_{*o}$ and $\alpha_s u_{*o}$ with constant thermal and saline exchange velocities, γ_T and γ_S (e.g., *Holland and Jenkins* (1999)). These parameterizations are equivalent to assuming a uniform friction velocity at the ice-ocean interface. In order to assess the consequence of this assumption, we ran one model case with constant γ_T and γ_S (which we refer to as the constant γ_T case, Table 4.3) to compare with the cases that utilize the parameterization given by Equations (4.3) and (4.4).

We calculated u_{*o} in Equations (4.3) and (4.4) from a surface quadratic stress such that $u_{*o}^2 = C_d |\mathbf{u}|^2$ with drag coefficient of $C_d = 2.5 \times 10^{-3}$ and \mathbf{u} taken from the surface σ -level. We assume the surface mixed layer can be represented by the surface σ -level and use these values of temperature and salinity for T_o and S_o . The value of T_b is approximated by the freezing point temperature, which we calculate following *Foldvik and Kvinge* (1974):

$$T_b = 9.39 \times 10^{-2} - 5.7 \times 10^{-2} S_b + 7.641 \times 10^{-4} h_{draft}, \quad (4.5)$$

where $h_{draft} < 0$. Equation (4.5) demonstrates the pressure dependence of w_b that is introduced by h_{draft} . We estimate S_b by combining the heat and salt fluxes given by Equations (4.3) and (4.4) with Equation (4.5) and solving for S_b . For the actual heat and salt fluxes into the top layer of the ocean model, we augment (4.3) and (4.4) to include the meltwater advection term described by *Jenkins et al.* (2001). Values of parameter choices are provided in Table 4.1.

Examples of similar applications in isopycnal coordinate system models can be reviewed in *Holland and Jenkins* (1999), *Little et al.* (2008, 2009), and *Makinson et al.* (2011). A z -coordinate model example is presented by *Losch* (2008). More examples of applications using the ROMS model are given by *Dinniman et al.* (2007), *Dinniman et al.* (2011) and *Galton-Fenzi* (2009). Additional σ -coordinate model applications are provided by *Grosfeld et al.* (1997) and *Beckmann et al.* (1999). A “plume model” approach, which assumes a non-dynamic ocean beneath the ice shelf plume, is used by *Holland and Feltham* (2006), *Payne et al.* (2007), *Holland et al.* (2007), and *Holland et al.* (2009).

4.3.2 Model grid and domain

The domain for simulations presented in this paper incorporates the portion of the Antarctic Peninsula (AP) that is shown in Figure 4.2. Our grid’s node spacing is 2 km in the horizontal with 21 σ -levels, the latter chosen to resolve the sub ice shelf surface mixed layer. Grids for ice draft (h_{draft} , see Section 4.3.2) and bathymetry (D , see Section 4.3.2)

are poorly constrained in many areas of our model domain. Given the importance of wct on tide predictions (Section 4.3.2), we attempted to create a realistic map of h_{draft} with two plausible options for D under LCIS. In creating and working with these maps, however, we recognized that the very large remaining uncertainties in geometry had a significant impact on w_b ; thus, we consign the detailed description of grid development to Supplementary Online Materials and focus here on describing the relevant features of the resulting maps and their inherent uncertainties.

Model Ice Draft (h_{draft})

Our estimated ice draft, based on satellite radar altimetry for epoch 1994/95, varies from ~ 900 m at the grounding line to ~ 100 m at the ice shelf front, with an average value of ~ 275 m (Figure 4.2a). The principal errors in converting ice elevation to h_{draft} arise from uncertainty in the density and thickness of the firn layer. A common approach to accounting for firn properties is to define a firn depth correction (Δh) obtained from measurements or models (see, e.g., *van den Broeke et al. (2008)*). For LCIS, *Holland et al. (2011)* suggested a firn depth correction of 0 and 20 m, assuming dry firn. In the northern LCIS, however, the firn is likely wet, suggesting a firn density correction error of 0 to 8 m, based on Figure 1 of (*Holland et al., 2011*). An 8 m difference in firn density correction would amount to ~ 50 m ice draft uncertainty in the northern LCIS. *Holland et al. (2009)* cited error in ice thickness measurements from airborne radio-echo sounding on the order of 10 m. These data were used by *Holland et al. (2009)* to constrain ice draft estimates from BEDMAP (*Lythe et al., 2001*) with the likely consequence of greatly reducing the error from firn density correction in their study. Our study relies on direct observations of firn

depth and a representation of the latitudinal variations in firn density described in *Holland et al.* (2009) (see Supplementary Online Material for details). Additional to the firn density error is an error from the uncertainty in the density of the marine ice that accumulates in bands in some regions of LCIS (*Holland et al.*, 2009).

Model seabed bathymetry (D)

Our open ocean model bathymetry (Figure 4.2b) is interpolated from the grid for the CATS2008 tide model (see Supplementary Online Documentation). This tide model utilizes data from the 2008 General Bathymetric Chart of the Oceans (GEBCO-2008, *Hall* (2006)) and the *Smith and Sandwell* (1997) global topography (TOPO12.1). The relatively smooth inner continental shelf seaward of LCIS reflects regions where the GEBCO-2008 gridded bathymetry is used while the rougher bathymetry further offshore is derived from TOPO12.1. Derivation of the estimated seabed bathymetry under LCIS is explained in Supplementary Online Documentation.

Our map of D under LCIS is qualitatively similar to a recent grid developed from airborne gravity measurements (*Cochran and Bell*, 2012). Both grids show much shallower bathymetry under the northern half of LCIS. The GEBCO-2008 product imposes a roughly semicircular bank over the continental shelf; however, there is little available in situ depth data east of the LCIS ice front (see *Luckman et al.* (2010), their Figure 1) and no airborne gravity measurements to confirm this feature.

Model water column thickness (wct)

The wct represents the distance from the seabed to the base of the ice shelf; it is equivalent to D offshore of the ice shelf, and to $D + h_{draft}$ beneath the ice shelf (where $D > 0$ and $h_{draft} < 0$). Our base case grid wct (Figure 4.2c), used for most runs reported in this paper, shows low wct in the northern half of LCIS where D is shallow, and a region of large wct in the southern portion of LCIS north of Gipps Ice Rise. Errors in wct arise from errors in h_{draft} (primarily due to uncertainties in the densities and thicknesses of firn and marine ice) and the larger uncertainties in D under and adjacent to LCIS. However, the general agreement between our grid of D and that developed by *Cochran and Bell (2012)* suggests that our grids will contain the principal geometric features influencing LCIS tides and basal melting.

Tidal analyses of recently acquired ice surface elevation time series from GPS receivers on LCIS (*King et al., 2011*) provide an opportunity to assess the general accuracy of our wct map. Following the methodology applied by *Galton-Fenzi et al. (2008)* to the Amery Ice Shelf, we investigate how changing wct under LCIS in a barotropic tide model affects the misfit between modeled and GPS-measured tide heights. The model used for this assessment is a regional subset of the CATS2008 inverse tide model. We ran the model for three wct grids (explained below) in forward mode (i.e., with dynamics but no data assimilation) but with open boundary conditions taken from the CATS2008 inverse tide model. This approach allowed us to assess how changes in wct affect the accuracy of the tide predictions judged relative to unassimilated data (the GPS records from *King et al. (2011)*). The LCIS-averaged wct ($\langle wct \rangle_{LCIS}$) for CATS2008 is ~ 133 m, significantly less

than $\langle wct \rangle_{LCIS} = 211$ m for our base case grid. We refer to the standard CATS2008 grid as “case $1 \times wct$ ”; two other test grids were constructed by multiplying the CATS2008 wct under LCIS by two and three (cases $2 \times wct$ and $3 \times wct$, respectively). The tests therefore span a range of $\langle wct \rangle_{LCIS}$ from 133 to 399 m, encompassing the value of $\langle wct \rangle_{LCIS} = 211$ m for our base case geometry.

We compared the observed tide amplitude variations from each of three GPS stations (locations shown on Figure 4.1) to the three modeled cases described above (Table 4.2), focusing on the largest semidiurnal tidal constituent M_2 . We used M_2 because its dynamical behavior as a Kelvin wave is simpler than the diurnal tides (O_1 and K_1), which contain significant energy as DTVWs (see Section 4.2.1) and are very sensitive to small-scale gradients in wct . The comparisons (Table 4.2) show that the $2 \times wct$ run most closely matches the GPS measured amplitude and phase for M_2 at all three locations, suggesting that the true value of $\langle wct \rangle_{LCIS}$ is around 266 m. The spatial variability of the wct remains unknown.

The ROMS3.2 three-dimensional model presented here produces slightly weaker tides under LCIS than the barotropic runs based on CATS2008 (see Table 4.2). We discuss possible reasons for this in Section 4.3.3.

4.3.3 Model forcing

Thermohaline exchange between the ocean and ice shelf is dependent on the temperature difference between the ice and the adjacent mixed layer, and the mixed layer current speed as a source of turbulence both at the ice base and at the interface with the underlying ocean (Section 4.3.1). Several factors external to the cavity can influence the

water mass properties and circulation within the cavity, including: sea ice formation, winds, general ocean circulation (the large-scale Weddell Gyre), and tides. In this paper, we focus on the influence of tides, as described below. However, we also carried out a single test of sensitivity to initial ocean potential temperature θ_0 , since the *Holland et al. (2009)* plume model of LCIS suggested that quite small changes in θ_0 could profoundly alter the magnitude and spatial distribution of basal melting and refreezing. We choose a “base case” setup and compare our sensitivity tests to these results. Details of the base case grid were described in 4.3.2 and other specifications are discussed in Sections 4.4.2. We also provide an overview of model simulations and forcing characteristics in Table 4.3.

Tides

For all cases except the tide amplification cases and the no-tide cases, we forced the open boundaries to the north, south, and east with the four most energetic tidal constituents extracted from CATS2008. These constituents are M_2 (period 12.42 h), S_2 (12.00 h), K_1 (23.96 h), and O_1 (25.82 h). Together, they account for most of the energy in the full tidal solution. There are some cases in which we closed the boundaries or forced the model with a subset of the diurnal and semidiurnal tides. When using open boundaries, the tidal forcing was applied with Flather boundary conditions for the barotropic velocity (*Flather, 1976*) and Chapman boundary conditions for the free surface height (*Chapman, 1985*). These conditions allow the barotropic velocity and surface elevations that deviate from exterior values to radiate out at the speed of external gravity waves. We applied 3D momentum and tracer diffusion at the boundaries and ramped the tide forcing from zero to 100% over ~ 20 days. We amplified the horizontal diffusivities along the open boundaries by a factor

of ten and decreased this amplification to the background levels within the interior using a cosine taper across a 20 grid cell wide sponge perimeter.

Tide height amplitudes predicted by ROMS3.2 under LCIS are about 20% weaker than in the CATS runs (Table 4.2), consistent with reductions of both heights and currents in the open ocean portion of the domain. We attribute this change to the effect of a different *wct* under LCIS, which is a significant fraction of our total model domain area. Model open boundary conditions in ROMS3.2 compensate for the resulting errors in tidal amplitude and phase by modifying the tidal energy flux across the open boundaries. A new barotropic tide model that takes advantage of improved estimates of sub ice shelf *wct* will reduce this difference.

Hydrography

Observations of the ocean properties in front of LCIS are limited to the locations shown in Figure 4.1. The most complete analysis of the hydrography adjacent to LCIS is given by *Nicholls et al.* (2004), who observed potential temperatures ranging from about -1.4°C to -2.1°C on the continental shelf adjacent to LCIS. Using a Gade line extrapolation (*Gade*, 1979) from the temperature and salinity from the meltwater plume, *Nicholls et al.* (2004) concluded that the primary inflow to the LCIS sub ice shelf cavity is from Modified Weddell Deep Water (MWDW) that flows onto the continental shelf, where it is cooled to the surface freezing point of -1.9°C and salinized to 34.63 during the winter. During the summer, MWDW may be advected toward the ice shelf cavity and cause the continental shelf waters to warm up to -1.4°C , but the authors state that it is unclear whether this warmer source water enters the sub ice shelf cavity.

Holland et al. (2009) used an ocean temperature of -1.9°C to force a plume model experiment and compared these results to a “warm” case with inflow temperature of -1.4°C . Modeled LCIS-integrated mass loss estimates for these two runs were 15 Gt a^{-1} and 70 Gt a^{-1} , respectively. For comparison, the flow of ice across the grounding line for Graham Land (the portion of the AP that is approximately north of the Kenyon Peninsula in Figure 4.1) is estimated from observations of interferometric synthetic aperture radar (InSAR) velocities and ice thicknesses at 20 and 49 Gt a^{-1} for 1996 and 2006, respectively (*Rignot et al.*, 2008). Although LCIS is the largest ice shelf in this region, these ice flux estimates include the impact of accelerated ice stream velocities following the collapse of the Larsen-A and -B ice shelves in 1995 and 2002, respectively; hence, we expect our modeled estimates of LCIS mass loss to be smaller than the *Rignot et al.* (2008) values. For LCIS to be in mass balance, ice sheet outflow to LCIS is balanced by calving or ice front advance, basal melt and accumulation, such that the lower modeled integrated melt rate from *Holland et al.* (2009) (associated with $\theta_0 = -1.9^{\circ}\text{C}$) more closely approximates observed values.

In this experiment, we follow *Holland et al.* (2009) by using an initially homogeneous ocean temperature and salinity. For most of our simulations we chose a θ_0 of -1.7°C and a salinity of 34.65. This salinity value corresponds to the “cold case” plume model run by *Holland et al.* (2009) while temperature was chosen as a mid-range value for the plausible range of -1.9°C to -1.4°C inflow temperatures. For one simulation, we set initial temperature to -1.9°C to represent the best estimate of inflow temperature given in *Nicholls et al.* (2004) and the cold case of *Holland et al.* (2009). For reasons explained in Section 4.4.8, we believe that the colder case (θ_0 of -1.9°C) is more consistent with available LCIS data;

however, the warmer case provides a more robust melting signal for sensitivity studies.

4.3.4 Errors

Here we summarize the primary sources of numerical errors in our simulations. More detail is provided in the Supplementary Online Document for *Mueller et al. (2012)* (Chapter 3 of this dissertation).

The ROMS3.2 σ -level vertical coordinate system and staggered Arakawa-C grid introduce conservative requirements of topographic variability to ensure model stability and general performance. The problem of numerical errors introduced by steep bathymetric slopes is exacerbated by the presence of the ice shelf base, which introduces a second sloping boundary to that of bathymetry. Therefore, a challenge in the present study was to create model grids that satisfied the conditions of model stability while also adequately resolving the sub ice shelf ocean boundary layer. To meet this challenge, we chose a sufficient number of levels (21) so that the maximum upper-layer thickness under ice is about 20 m, smaller than the expected upper ocean boundary layer of about 50 m. In addition, we minimized the possibility of unrealistic spurious flows generated by baroclinic pressure gradient errors by smoothing the seabed bathymetry and ice draft grids to satisfy the Haney criterion (*Haney, 1991*) over most of the grid. The Haney criterion limits the vertical displacement of σ -levels between adjacent grid cells to allow accurate interpolation of baroclinic pressure at specific depths (see Supplementary Online Documentation to *Mueller et al. (2012)*, included here in Chapter 3). We also imposed a minimum value of $wct = 100$ m prior to our final smoothing.

We ran several tests to determine the optimum advection scheme and the minimum background values for viscosity and diffusivity required to prevent grid scale errors

from growing with time. For all runs described in this paper we used the default advection schemes (i.e., 4th order centered for tracers and vertical advection of momentum, and 3rd order upstream for horizontal advection of momentum) with a Mellor-Yamada 2.5 turbulence closure scheme for vertical mixing (*Mellor and Yamada, 1974, 1982*). Minimum vertical eddy viscosity and diffusivity coefficients were $A_{z,min}, K_{z,min} = 5 \times 10^{-5} \text{ m}^2 \text{ s}^{-1}$ and $1 \times 10^{-5} \text{ m}^2 \text{ s}^{-1}$, respectively, and Laplacian horizontal mixing coefficients were $A_h = 5 \text{ m}^2 \text{ s}^{-1}$ and $K_h = 1 \text{ m}^2 \text{ s}^{-1}$. Horizontal mixing is along σ -levels for momentum and geopotential surfaces for tracers. A complete list of the model’s C-preprocessing options (referred to as “cppdefs”) is given in Chapter 3.

4.4 Results

4.4.1 Tidal current distribution

Tidal analyses of a model run with no thermohaline ice-ocean exchange indicate that the O_1 diurnal constituent generates the strongest tidal currents, with the largest values in the NE corner of LCIS (Figure 4.3). Figures 4.3a and 4.3b show the spatial distribution of the magnitude of the barotropic tidal ellipses for the M_2 and O_1 constituents, respectively. The spatial pattern of K_1 currents is similar to O_1 with a mean magnitude that is about 12% less; S_2 currents have a similar spatial structure to M_2 and are, on average, $\sim 30\%$ weaker. The large barotropic currents in the NE region are dominated by the diurnal tides, even though the modeled diurnal tidal elevation amplitudes are smaller in this region than those of the semidiurnal tides (not shown). We attribute this enhancement to the generation of DTVWs (see Section 4.2.1). The largest semidiurnal currents occur near the Churchill and

Kenyon peninsulas (Figure 4.3a) but are much weaker than the diurnal currents in the NE region (Figure 4.3b). Modeled tidal currents along the deep grounding line of the western LCIS are very small; however, we imposed a minimum wct of 100 m (see Section 4.3.4), so that actual tidal current speeds may be larger than in our model where true wct is less than 100 m.

For simulations forced by multiple tidal constituents, we characterize the spatial variability of tidal currents by mapping the time- and depth-averaged tidal current speed U_{tide} , determined from

$$U_{tide} = \left\langle \sqrt{u_b^2 + v_b^2} \right\rangle_t, \quad (4.6)$$

where $u_b(x, y, t)$ and $v_b(x, y, t)$ are orthogonal components of modeled, depth-averaged current and $\langle \rangle_t$ represents temporal averaging. This value represents a typical tidal current speed contributing to mixing near the ice-ocean interface. Figure 4.3c shows U_{tide} for our standard geometry (Figure 4.2) based on the last 30 days of our run with no ice-ocean thermodynamics (“no thermo” case in Table 4.3). The largest values of U_{tide} exceed 0.4 m s^{-1} in the northeast corner of LCIS.

The semidiurnal tides, M_2 and S_2 , introduce a spring-neap cycle of modulation with period ~ 14.7 days; similarly, O_1 and K_1 produce a spring-neap cycle with period ~ 13.7 days. These two cycles beat together to produce a semi-annual cycle with periodicity of ~ 183 days (e.g., Figure 4.4b). Tides will also be modulated by the ~ 18.6 year lunar node tide cycle, but we neglect this variation because our model run time is not sufficiently long. The lunar node modulation introduces an additional $\sim 10\%$ variability of amplitude in the

northeastern LCIS region, as predicted by the CATS2008 barotropic tide model.

4.4.2 Base case

Our base case model (Table 4.3) has an initial uniform potential temperature of $\theta_0 = -1.7^\circ\text{C}$ and $S_o = 34.65$ (see Section 4.3.3). Boundary forcing was obtained from the M_2 , S_2 , K_1 , and O_1 tidal constituents provided by CATS2008 (see Section 4.3.3). This setup was run for 10 model years and the output was averaged over 30-day intervals (~ 2 spring-neap cycles). After completion, the base case was re-started to run for an additional 180 days with 2-day averaged output. For this extension run we also introduced a passive dye tracer beneath LCIS and Lagrangian floats at various depths and locations along the LCIS front.

The spatial pattern of time-averaged w_b for the base case, averaged over the 180-day extension run, is shown in Figure 4.5a. A maximum value of $\sim 2 \text{ m a}^{-1}$ occurs in the NE region, and is co-located with the region of largest time-averaged barotropic tidal speeds. As explained in Section 4.4.1, these large current speeds are mainly due to the diurnal tides (Figure 4.3b,c). The time-averaged surface σ -level velocity represents the thermohaline plume and is shown in Figure 4.5b. The plume speeds are greatest at the grounding line, along a band oriented NE through the mid-shelf region, along the ice front, and around the region of amplified melt.

In the NE region, the combination of small wct , large spatial gradients of wct and associated large gradients in tidal currents provides the conditions required for generation of rectified tidal flows (see Section 4.2.1). We evaluate the modeled Eulerian component of these rectified flows by calculating, from the tide-forced run with no ice-ocean thermody-

namics, the modeled time-averaged (“residual”) barotropic velocity

$$\mathbf{u}_{\text{res}}(x, y) = (\langle u_b(x, y, t) \rangle_t, \langle v_b(x, y, t) \rangle_t), \quad (4.7)$$

where u_b and v_b are defined in Section 4.4.1. Values of \mathbf{u}_{res} are noisy, associated with numerical errors at the grid-scale level in the model. We therefore used a 5x5 2-D boxcar filter to smooth \mathbf{u}_{res} to resolved scales of ocean variability ($\sim 5 \times \delta x$, where $\delta x = 2$ km is the grid node spacing). The vector map of filtered \mathbf{u}_{res} is shown in Figure 4.5c. About 1% of the values of the magnitude of \mathbf{u}_{res} ($|\mathbf{u}_{\text{res}}|$) beneath LCIS are greater than 0.05 m s^{-1} . For grid cells where U_{tide} exceeds 0.05 m s^{-1} , the mean of the ratio $|\mathbf{u}_{\text{res}}(x, y)|/U_{\text{tide}}$ is ~ 0.05 with a standard deviation of ~ 0.06 .

As a comparison, a sensitivity case that neglects tidal forcing (see Section 4.4.3) has a maximum value of the 30-day averaged, surface-level velocity at ~ 1 year of 0.01 m s^{-1} . Hence, $|\mathbf{u}_{\text{res}}|$ can be large relative to the thermohaline-only plume speeds under LCIS, implying that rectified barotropic tidal circulation may exert significant control on the transport of meltwater plumes under LCIS. Rectified tides may play an additional role of ventilating the sub ice shelf cavity (cf. *Makinson and Nicholls (1999)*). We do not, in this paper, attempt to separate the effects of increased mixing and mean advection by rectified tides on the distribution and magnitude of w_b .

Weaker local maxima in w_b are also found along the northern flank of Kenyon Peninsula and near the grounding zone under the western LCIS. Locations of augmented melt in the western margins of the ice shelf cavity correspond to the deepest points of the ice shelf draft. These regions are also the high-melt sites seen in the *Holland et al. (2009)*

plume model. The modeled tidal currents are negligible in this region (Figure 4.3), and we attribute the augmented melt there to the pressure suppression of T_f .

The base case predicts that meltwater will refreeze to the ice shelf base in a few small regions (Figure 4.5a). Most of these regions are towards the back of the LCIS cavity in regions where very cold meltwater from the deep grounding zone is buoyantly forced upward to depths where the plume temperature becomes less than T_f . These locations are in general agreement with the onset of marine ice flowbands identified from signal quality in air-borne radio-echo sounding in *Holland et al. (2009)*; however, we reiterate that our model lacks the ability to create frazil ice within the water column, so that we cannot confirm the marine-ice accumulation rates estimated by *Holland et al. (2009)*.

4.4.3 Tide forcing and wct sensitivity

Our analyses of GPS tidal data (Section 4.3.2) suggest that the average wct for LCIS ($\langle wct \rangle_{LCIS}$) is ~ 266 m, compared to 211 m for our base model geometry (which was created using available data for ice elevation and bathymetry). Two point measurements of wct from seismic soundings (see Table 4.4) indicate local wct of 362 and 412 m. Based on these limited constraints, we created a second model geometry to investigate the potential influence of wct uncertainty by imposing a minimum wct of 350 m beneath LCIS, with a resulting $\langle wct \rangle_{LCIS}$ of 355 m (we refer to this as the “350 m case”). We did this by retaining the original map of h_{draft} and increasing D in order to enforce the minimum wct criteria, then re-smoothing the grid to minimize pressure gradient errors (discussed in Section 4.3.4 and in Chapter 3). As shown in Figure 4.6, this case significantly increases wct in the northern section of the ice shelf and reduces the tidal currents from the base case values

(Figure 4.6b), specifically by reduction in the magnitude of diurnal components. The effect of this reduced tidal forcing is a reduction of the basal melt in the NE region by as much as 2.3 m a^{-1} (Figure 4.6c). We attribute this reduction to the removal of geometric conditions required for the excitation of DTVWs (Sections 4.2.1 and 4.4.1).

In order to further assess the sensitivity of the spatial distribution of LCIS basal melt rate to tidal forcing, we ran seven simulations in addition to the base and 350 m cases described above (see Table 4.3). These are: K_1+O_1 , M_2+S_2 , $\min u_{*o}$, constant γ_T , and three cases with scaled tidal forcing. The K_1+O_1 and M_2+S_2 cases separate the influences of diurnal and semidiurnal tides. The $\min u_{*o}$ case approximates the plume-flow model reported by *Holland et al.* (2009); however, significant differences between the models limit direct comparison. The constant γ_T case represents a common approach to simplified representation of currents due to unresolved processes (such as tides) in models (see Section 4.3.1). The three simulations with scaled open-boundary tide forcing were run to represent a range of tidal currents under LCIS that bracket the estimated uncertainties due to model limitations.

Most runs are 400–600 days simulations, determined by available computational resources; however, the base and 350 m cases are 10 year simulations. The time series of modeled ice shelf averaged w_b rates indicate that most adjustment to forcing occurs in the first few simulated months (Figure 4.4a), although the value for the base case declines a further $\sim 30\%$ from 0.30 to 0.21 m a^{-1} from model year 1 to year 10 (Figure 4.4b).

In Figure 4.7, we compare the maps of w_b from the base case with the 350 m case and the first four cases described above, using 30-day time-averaged values from around

365 days of model run time. The 350 m wct case tests the influence of wct on w_b . This case uses the same forcing of tides as in the base case; however, the resulting tidal currents (not shown) under LCIS are much weaker. This reduction in tidal currents effectively removes the amplified basal melt in the NE region (Figure 4.7 a,b). Away from the NE region, these two cases produce equivalent predictions. The K_1+O_1 case captures most of the variability of $w_b(x, y)$ in the base case (compare Figures 4.7a,c). The M_2+S_2 case (Figure 4.7d) is similar to the 350 m case, with strongest melt along the Churchill and Kenyon peninsulas and the deep grounding lines in the western LCIS; the large melt signature in the NE is absent.

The min u_{*o} case was uniformly initialized with a minimum $u_{*o} = 1 \times 10^{-4} \text{ m s}^{-1}$ that could increase as the thermohaline circulation developed. This case most closely approximates a plume model approach. The spatial pattern of w_b for this run (Figure 4.7e) is very different from the base case. Most basal melt for the min u_{*o} case is concentrated near the grounding zone while all other non-pressure dependent melt is negligible.

The constant γ_T case is equivalent to assuming a total current (tidal plus thermohaline) speed that is uniform everywhere under the ice shelf. We chose values of $\gamma_T = 1 \times 10^{-4} \text{ m s}^{-1}$ and $\gamma_S = 5.05 \times 10^{-7} \text{ m s}^{-1}$ to be consistent with several prior model studies (e.g., *Hellmer and Olbers (1989); Holland and Jenkins (1999); Beckmann et al. (1999); Dinniman et al. (2007)*). This parameterization results in strong melt at the grounding zone with little melt elsewhere (Figure 4.7f). Since our modeled tidal currents are very low over much of LCIS including along the deep grounding line in the western LCIS (Figure 4.3), the constant γ_T case overestimates the current speeds for much of the ice shelf

and produces w_b values that are much higher than in the base case in the grounding zone.

4.4.4 Sensitivity of w_b to ocean temperature

For one run (“cold case”, see Table 4.3), θ_0 is reduced to -1.9°C , the approximate surface freezing point for water at the specified salinity of $S_o = 34.65$. All other factors, including geometry and tide forcing, are the same as for the base case. The spatial structure of the map of w_b for the cold case (Figure 4.8) is similar to that for the base case but with a reduction of 67% in LCIS-averaged melt rate. This result demonstrates that the strong dependence of melt rate on ocean temperature found in the plume-only model by *Holland et al.* (2009) is also true for our tide-forced models.

4.4.5 Basal melt relative to ice draft

The primary differences in spatial heterogeneity of w_b for the major model runs are characterized by averaging w_b into 50-m ranges of h_{draft} (Figure 4.9a) and calculating area-integrated ice volume loss rates binned into the same h_{draft} ranges (Figure 4.9b). The base case results show highest values of bin-averaged w_b ($\sim 1.5 \text{ m a}^{-1}$) under thick ice near the grounding line (Figure 4.9a); however, most net volume loss is predicted under the much more extensive regions of shallower ice near the ice front (Figure 4.9b). Consistent with Figures 4.7a,c, the distribution of net volume loss for the K_1+O_1 case is close to that for the base case.

The constant γ_T case results show much larger values of LCIS-averaged w_b for $h_{draft} < -300 \text{ m}$ (Figure 4.9a). Values near the deep grounding lines are ~ 4 times greater than in the base case. The area-integrated values for the constant γ_T case show a broader

distribution with respect to h_{draft} , and with a maximum contribution from thicker ice than for the base tide-forced case (Figure 4.9b). Despite the differences in melt rate dependence on h_{draft} , the base and constant γ_T cases have similar total ice volume loss rates of $18.6 \text{ km}^3 \text{ a}^{-1}$ and $19.2 \text{ km}^3 \text{ a}^{-1}$, respectively (based on the values shown in Figure 4.9). The similarity of these values is coincidental since we used a value of γ_T taken from the literature rather than one tuned to match the integrated basal melt rate in the base case.

4.4.6 Comparison of LCIS-averaged basal melt rates

The basal melt rate averaged over LCIS for our base case is $\langle w_b \rangle_{LCIS} = 0.25 \text{ m a}^{-1}$ (from results shown in Figure 4.5a). The corresponding total ice volume loss of $14 \text{ km}^3 \text{ a}^{-1}$ is close to the loss of $\sim 16 \text{ km}^3 \text{ a}^{-1}$ for the “cool case” reported by *Holland et al.* (2009) (who assumed an ocean temperature of -1.9°C). We expect our base case estimate to under-predict the actual basal melt that would occur at -1.7°C because our tidal amplitudes appear to be lower than those observed by the three GPS locations described in Section 4.3.2 and Table 4.4. The lowest value in our set of simulations compared in Figure 4.10 was $\sim 0.1 \text{ m a}^{-1}$ for our cold case with $\theta_0 = -1.9^\circ\text{C}$.

We performed three runs with open-ocean tidal forcing scaled by 0.5, 0.75, and 2.0 to describe a likely range of uncertainty in tidal currents due to errors in the wct grid. The case with tidal currents two times greater than the base case gives the largest value of $\langle w_b \rangle_{LCIS}$ (0.44 m a^{-1}). This case roughly approximates the response to a uniform reduction in wct of $\sim 50\%$ or generation of more energetic DTVWs than appear in our models; however, the magnitude of this reduction in averaged wct is not supported by the comparison with tidal analyses of GPS time series (see Section 4.3.2). In general, Figure 4.10 demonstrates

that the ice shelf averaged basal melt rates increase nearly linearly in response to increased tide amplification. These results suggest an uncertainty of $\langle w_b \rangle_{LCIS} = 0.15 \text{ m a}^{-1}$ given a two-fold uncertainty in LCIS-averaged wct . In reality, the actual sensitivity will vary depending on the degree and strength of tide-topography interactions.

The min u_{*o} case, which most closely compares to the *Holland et al.* (2009) plume model, shows LCIS-averaged $\langle w_b \rangle_{LCIS} = 0.14 \text{ m a}^{-1}$ for $\theta_0 = -1.7^\circ\text{C}$, about half that of the base case. The constant γ_T model provides a similar LCIS-averaged w_b and total ice volume loss as the base case, even though the spatial distributions of w_b are very different (Figure 4.9). The value of $\langle w_b \rangle_{LCIS}$ for the 350 m case is most similar to the $M_2 + S_2$ case, $\sim 0.19 \text{ m a}^{-1}$. For the range of sensitivity cases outlined in Table 4.3, $\langle w_b \rangle_{LCIS}$ is $\sim 0.11\text{--}0.44 \text{ m a}^{-1}$.

4.4.7 Cross front exchange and ventilation

We illustrate water mass exchange across the ice shelf front by dye tracers and Lagrangian floats in the 180-day runs initialized from the end of the 10-year base and 350 m cases. Both the 350 m and base cases show outflow in the surface level of the northern LCIS (Figure 4.11a,b) and inflow near the seabed along the southern ice front of LCIS (Figure 4.11c,d). The inflow extends $\sim 100 \text{ km}$ into the cavity after 180 days, reaching the tip of Kenyon Peninsula. The core of the meltwater plume circulates northeastward across the middle of LCIS (Figure 4.5b) towards the region of strong recirculation in the NE LCIS. This flow pattern through the center of the cavity differs from that shown by the plume model of *Holland et al.* (2009). These differences may be attributed to the influence of tide forcing, differences in modeled h_{draft} , and the effect of finite wct on the depth-averaged

mean circulation.

The 350 m case results show more across-front exchange along the central LCIS, at all depths, than the base case (compare Figures 4.11a,b and 4.11c,d). The time series of total dye volume under LCIS shows that, despite these differences in spatial distribution of dye, there is no significant change in the time-averaged net dye volume flux across the LCIS ice front; the cross front exchange for both cases is $\sim 0.2 \times 10^6 \text{m}^3 \text{s}^{-1}$ (0.2 Sv). Based on this flux across the ice front and our estimate of total ocean volume under the ice shelf, a “ventilation” time scale for LCIS is of order 2–3 years.

Although the net cross-front exchange is equivalent between the base and 350 m cases, the surface level dye export is much stronger in the north for the base case than for the 350 m case. We calculated the volume weighted mean dye concentration for the surface level in the region defined by the white box in Figure 4.11a and found that the mean concentration of dye (meltwater) in the base case is 1.7 times the concentration of dye within the same region for the 350 m case. We hypothesize that the stronger vorticity gradient across the ice shelf front in the base case is more effective at steering the meltwater outflow to the north where it is eventually forced by the Jason Peninsula to exit the cavity (see, also, Figure 4.5b).

Our LCIS results can be compared with a study of the flow regime along Ronne Ice Shelf front (*Makinson, 2002*) where currents along the ice front, even below the depth of the ice base near the front, are strongly steered along the front until summer stratification overcomes the vorticity constraint on deep, across-front exchange. The exchange across the ice shelf front is important to understand because it will affect how ocean circulation and

climate change will affect sub ice shelf cavity basal melt. Our results show that uncertainties in bathymetry influence across-front vorticity constraints and, hence, across-front exchange; however, we are unable to explain more fully the across-front exchange for LCIS because other factors that are not represented in this study (e.g., wind forcing and stratification) would also influence across-front exchange as well as seasonal and longer term variability in sub ice shelf ventilation.

4.4.8 Evaluating the accuracy of our w_b predictions

There are only a few direct observations of LCIS w_b and these are short term, point measurements (N. Gourmelen, pers. comm., 2010). This paucity of direct measurements of w_b , the simplified model forcing (tides only), and the uncertainties in model geometry and hydrography means that we cannot unambiguously determine which of our models best represents the real distribution of LCIS basal melt rate. However, we note that the high basal melt rate in the NE corner of 2 m a^{-1} in the base case (Figure 4.5a) is much larger than surface mass balance of $< 0.5 \text{ m a}^{-1}$ (water equivalent) in this region (*van de Berg et al.*, 2006). Therefore, if this amount of basal melting was occurring, the ice shelf would be thinning rapidly downstream along flowlines, contrary to the observed ice draft map (Figure 4.2a). In the cold case, maximum melt rate in the NE corner is $\sim 0.6 \text{ m a}^{-1}$ (Figure 4.8b), close to surface mass balance and, therefore, more consistent with ice shelf topography. Furthermore, the extent of regions where marine-ice accretion is known to occur (*Holland et al.*, 2009) are better represented by the cold case with $\theta_0 = -1.9^\circ\text{C}$ than the base case with $\theta_0 = -1.7^\circ\text{C}$ (Figure 4.8). We propose, therefore, that the cold case is closer to the optimum model for LCIS basal melt than the base case. This result is

consistent with the conclusion by *Nicholls et al.* (2004) that LCIS meltwater is produced at the ice-ocean interface with ambient ocean temperatures close to the surface freezing point of $\sim -1.9^\circ\text{C}$. The cold case predicts negligible overall melting, $\langle w_b \rangle_{LCIS} \approx 0.1 \text{ m a}^{-1}$ (Figure 4.10), supporting the view that measured LCIS elevation loss over the last two decades (*Zwally et al.*, 2005; *Fricke and Padman*, 2012) is due primarily to surface firn compaction including melting (*Holland et al.*, 2011) rather than changes in basal melt rates (*Shepherd et al.*, 2003). However, we emphasize that the addition of realistic forcing and stratification in the open ocean adjacent to LCIS may significantly change the pattern of melt rate and net mass loss through melting, even if the true inflow temperature is close to -1.9°C .

4.4.9 Broader implications

The thickness distribution of an ice shelf is the outcome of a complex mass balance involving the contribution of ice from the grounded ice sheet, lateral divergence of ice mass, surface accumulation (snowfall), basal melting, and iceberg calving. These processes interact with each other through the ice shelf force balance so that changes in the distribution of basal melting will affect inflow, divergence, and calving. Basal melt rate can, in theory, be solved as the residual of the other mass balance terms using ice velocities derived from InSAR and column-integrated ice mass (M) inferred from altimeter-derived surface elevation and density models (e.g., *Joughin and Padman* (2003)). In practice, however, it is difficult to create accurate maps of M , especially for ice shelves such as LCIS where column-averaged ice density can change over short distances in response to variations in density and layer thickness of firn (*Holland et al.*, 2009, 2011) and marine ice (*Craven*

et al., 2009). Uncertainty in M affects ice mass divergence estimates, and further errors arise through a poor understanding of surface accumulation rates. Our suite of simulations provides guidance to the additional data that are needed to assess the future stability of LCIS and other ice shelves.

Without tides, melt is concentrated along the deep grounding lines of tributary glaciers (Figure 4.7e), similar to the pattern reported by *Holland et al.* (2009). When tides are included, the extra melt is concentrated in the NE region (Figure 4.7a); strong diurnal currents in this region of low wct lead to vigorous mixing of ocean heat to the ice base. This increased advection and mixing due to tides, if combined with warming ocean temperatures, could lead to an accelerated thinning in this region with increased likelihood of mass loss through calving (*Alley et al.*, 2008). However, uncertainty in the map of wct leads to a wide range of plausible distributions of w_b (compare Figures 4.7a and 4.7b). When the uncertainty in temperature of the inflowing ocean is also considered, the range of plausible mean basal melt rates (Figure 4.10) and spatial distributions (Figure 4.7) is very large.

The sensitivity of tidal current speeds to the distribution of wct indicates that tides can act as a feedback to basal melt rates. The sign of the feedback is not obvious a priori, which complicates the incorporation of basal melt into ice sheet models that attempt to provide long time integrations of ice mass changes (*Pollard and DeConto*, 2009; *Joughin et al.*, 2010). We suggest that the change in tidal currents with respect to wct variability should be a focus of future research on LCIS and other ice shelves where tidal currents could be sensitive to fairly small changes in wct .

The three ice shelves for which the importance of tides is now verified through

modeling (FRIS (*Makinson et al.*, 2011); Amery Ice Shelf (*Galton-Fenzi*, 2009); and LCIS, this study) share the characteristics that tidal currents are large compared with innate plume velocities, and the temperature of the inflowing water is close to T_f . We refer to these as “cold water” ice shelves. Preliminary modeling of the Ross Ice Shelf indicate that tides also affect the distribution of basal melting there (S. Springer, pers. comm., 2011). The dominance of melt near Ross Ice Shelf front (*Horgan et al.*, 2011) suggests that tides will be particularly effective at increasing near-front basal melting in summer when warm near-surface water can be advected periodically under the ice shelf.

For ice shelves with inflow temperatures a few degrees above T_f (“warm water” ice shelves), such as those fringing the Amundsen Sea, the tidal contribution to w_b may be small because the velocity of the innate thermohaline flows (and, therefore, u_{*o}) is already large (e.g., *Payne et al.* (2007)). However, several tidal processes might invalidate this assumption. First, as we found for LCIS, tidal rectification can affect the mean advection pathways for ventilation of specific regions of an ice shelf. Second, generation of baroclinic tides by barotropic flow across rough and/or steep topography (at the seabed and at the ice base) may create energetic mixing, both at the ice-ocean boundary and at the interface between a freshwater plume and the underlying ocean. Third, tidal influences near the grounding line are hard to predict because of the generally poor representation of geometry there. Fourth, it is plausible that tidal interactions with large amplitude, small-scale features in ice base topography (e.g., the quasi-annual “ripples” on Pine Island Ice Shelf (*Bindschadler et al.*, 2011) and the narrow, along-flowline channels on the base of Amery Ice Shelf (*Fricker et al.*, 2009) and Petermann Ice Shelf in NW Greenland (*Rignot and Steffen*, 2008)) may lead to

much greater tidal effects than would be predicted from the larger, model-resolved scales of topographic variability. Given these uncertainties, modeling of w_b for any specific ice shelf should include tests with and without tidal forcing rather than excluding tides solely on the basis of weak currents in barotropic tide models.

The sensitivity of w_b to the strength of DTVWs implies that high-resolution grids of wct will be required to reduce uncertainties in w_b . Errors in h_{draft} due to uncertainty in the ice density profile may be sufficient to affect modeled tidal currents. This error (up to ~ 50 m) is comparable to the inferred wct in the NE region of LCIS, which means that errors in h_{draft} could result in a large fractional change in wct . The paucity of seabed depth data for most ice shelves implies that even larger errors in wct may arise from errors in D . This is true even for ice shelves whose cavities have been coarsely surveyed by in situ grids of seismic reflectivity (e.g., FRIS (*Johnson and Smith, 1997*) and Ross Ice Shelf (*Greischar and Bentley, 1980*)), since typical seismic station spacing (50–100 km) is much greater than the topographic length scales associated with DTVWs.

A conservative requirement for grid spacing is the ability to resolve the internal Rossby radius of deformation, which is ~ 5 km at polar latitudes; this requirement implies a model grid node spacing of ~ 1 – 2 km. While the ice shelf surface can be mapped at this resolution by aircraft altimeters, the prospects for high-resolution mapping of D are, presently, poor.

4.5 Conclusions

We applied the Regional Ocean Modeling System (version 3.2) with thermodynamic coupling between a non-evolving ice shelf and the ocean to quantify the sensitivity of LCIS basal melt rate (w_b) to tidal forcing, water column thickness distribution (wct), initial ocean potential temperature (θ_0) and parameterizations of ice-ocean thermodynamic exchange. From our study, we reach the following LCIS-specific conclusions.

1. For the range of simulations reported here, ice shelf averaged basal melt rate $\langle w_b \rangle_{LCIS}$ is $\sim 0.11\text{--}0.44 \text{ m a}^{-1}$, corresponding to $7\text{--}27 \text{ km}^3 \text{ a}^{-1}$ ($6\text{--}24 \text{ Gt a}^{-1}$) total ice loss. For most of our simulations, net mass loss primarily occurs where ice draft is between 100 and 350 m. The locations of regions of high melt rates vary from one simulation to another.
2. In a model run without tidal forcing, regions of relatively rapid melt are found near the deep grounding lines of glaciers feeding LCIS. Melt rates elsewhere are negligible. When tides are added, w_b increases in the NE corner of LCIS, and along the edges of the Churchill and Kenyon peninsulas.
3. For $\theta_0 = -1.7^\circ\text{C}$, adding tidal forcing approximately doubles $\langle w_b \rangle_{LCIS}$ relative to a model forced only by thermohaline exchanges between the ocean and ice base. The tide-induced increase in $\langle w_b \rangle_{LCIS}$ is due primarily to significant enhancement of w_b in the NE region of LCIS; in this region, diurnal topographic vorticity waves (DTVWs) excited by tidal interactions with gradients in wct create strong tidal currents (up to $\sim 0.4 \text{ m s}^{-1}$) with the consequence of increased basal melting melt. However, accurate

prediction of tidal currents in this region is difficult. Our model domain omits Bawden Ice Rise, whose presence suggests that there may be significant regions where wct is less than our imposed minimum value of 100 m, and the real flux of tidal energy as DTVWs along the ice front and into the cavity will be different than in our model. The errors in sub ice shelf geometry (including the omission of Bawden Ice Rise and model limitations on resolving DTVWs) imply a factor of ~ 2 uncertainty in $\langle w_b \rangle_{LCIS}$.

4. With the base case geometry, tides generate a rectified barotropic circulation whose magnitude (up to $\sim 0.05 \text{ m s}^{-1}$ in regions of strong tidal currents) can exceed typical thermohaline flows. The rectified tidal flow may, therefore, contribute to the ventilation of the sub ice shelf cavity and the fate of freshwater as it circulates under LCIS.
5. The sensitivity of w_b and tide-induced mean circulation to the energetics of DTVWs implies that high-resolution grids of ice draft and seabed bathymetry will be required to minimize uncertainties in w_b . Studies of DTVWs along the continental slope (*Middleton et al.*, 1987; *Padman et al.*, 1992) demonstrate that cross-slope length scales of these waves are similar to the cross-slope scale of topographic variability. These scales can be very small close to the ice front, with large fractional changes in wct over a distance of order 1 km. Under the bulk of the ice shelf, large channels with scales of order 1–10 km are found; however, their contribution to DTVWs is uncertain. A conservative estimate of required grid resolution is the ability to resolve the baroclinic Rossby radius of deformation, ~ 5 km in high latitude seas, implying a model grid spacing of $\delta x \sim 1$ km.

6. With forcing only from tides and ice-ocean thermohaline exchange, the volume flux across the ice front is ~ 0.2 Sv, corresponding to a mean ventilation time of 2–3 years for the LCIS cavity.
7. For the cold case with $\theta_0 = -1.9^\circ\text{C}$, $\langle w_b \rangle_{LCIS}$ is reduced by a factor of ~ 3 relative to our base case with $\theta_0 = -1.7^\circ\text{C}$.
8. A commonly used model with constant γ_T , corresponding to a total current speed that is constant under the entire ice shelf, predicts high melt rates in the grounding zone but relatively low melt rates elsewhere. The sensitivity of this parameterization to pressure guarantees maximum melt rates at the grounding line for conditions of uniform temperature; as such, this parameterization may produce distributions of ice shelf basal melt that are inconsistent with the real spatial pattern, yielding mass and force balances that are biased accordingly.
9. From comparisons with available data, we tentatively conclude that our cold case ($\theta_0 = -1.9^\circ\text{C}$) is our best representation of LCIS basal melting under current oceanographic conditions. This case provides: estimates of w_b in the NE corner that are consistent with observed changes in ice shelf geometry, predictions of marine ice accumulation regions that are more consistent with the marine ice accumulation zones shown in *Holland et al. (2009)*, and agreement with the inflow temperature inferred by *Nicholls et al. (2004)*. However, since our model lacks realistic ocean stratification, atmospheric forcing and sea ice effects, the true pattern and magnitude of w_b may be different from our cold case simulation.

We conclude that the accuracy of w_b predictions is undermined by potential errors in sub ice shelf geometry and ocean hydrography such that there is an urgent need for new data sets to adequately constrain models of ice shelf and ocean interactions. The most promising approaches to large-scale mapping of ice shelf geometry come from airborne altimetry and gravity surveys over ice shelves (e.g., *Cochran and Bell (2012)*). However, improved data sets for conversion of ice surface height to ice draft are also required, either through remote sensing methods (see *Holland et al. (2011)*) or in situ density measurements (e.g., *Jansen et al. (2010)*). Hydrographic data are needed for all seasons in order to determine the temperature of inflow and its seasonal variability. Given the strong spatial variability of cross-front exchange suggested by our dye experiments (Figure 4.11), data must be collected at several locations along the entire length of an ice front. For FRIS and LCIS, this remains a significant challenge because of the thick, year-round sea ice cover typical of the southern and northwestern Weddell Sea. Until these improved data sets become available, numerical studies of ice shelf basal melt should cite basal melt rates in the context of potential errors from modeling uncertainties in geometry, hydrography and atmospheric forcing.

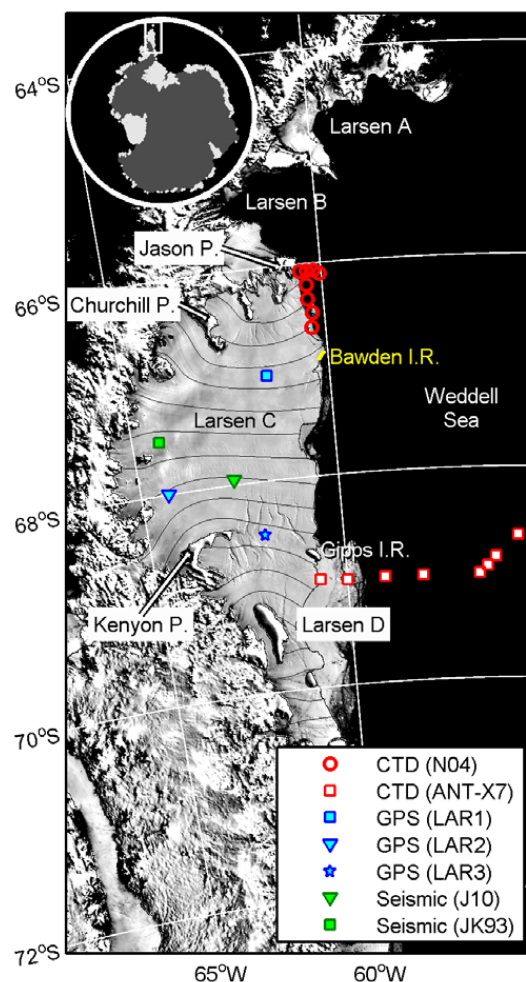


Figure 4.1: Location map for Larsen C Ice Shelf showing data sources used to define model geometry and hydrography. The Bawden Ice Rise, indicated by yellow, was not included in our model geometry. CTD stations include those reported by *Nicholls et al.* (2004) (N04) and *Bathmann et al.* (1994) (ANT-X7). GPS ice elevation data (LAR1, LAR2, LAR3) are described by *King et al.* (2011). Seismic surveys from *Jarvis and King* (1993) (JK93) and *Jansen et al.* (2010) (J10) provided local measurements of ice and firn density profiles in addition to seabed depth and water column thickness. The black flowlines on the ice shelf are based on recent interferometric synthetic aperture radar velocity measurements of ice flow (described in Section 3.2).

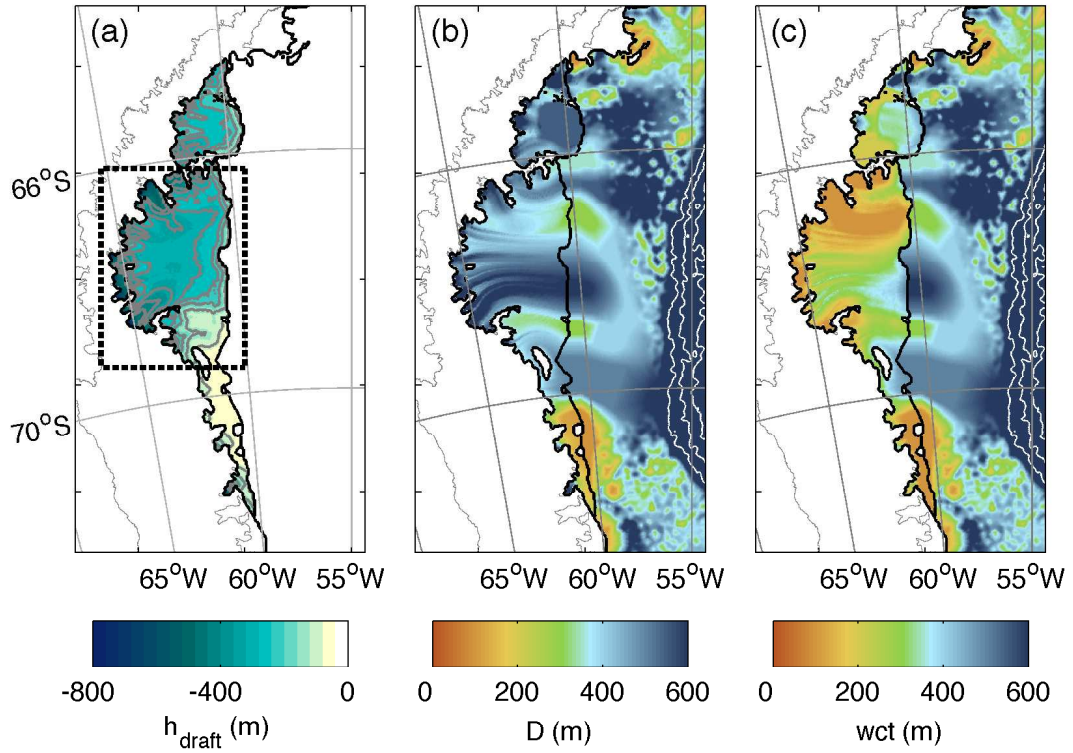


Figure 4.2: Model geometry used in this study. (a) Ice draft (h_{draft}) used for all simulations presented in this paper. The black lines represent the land mask and the ice shelf fronts used in our model. The thick gray lines are 50-m contour intervals of h_{draft} . The ice shelf within the dashed rectangle indicates the area that we refer to as LCIS and is the domain used to estimate LCIS-averaged values; this rectangle also shows the graphics boundary used in Figures 4.3, 4.5, 4.6, 4.7, and 4.8. (b) Bathymetry (D) used in all model runs except for the 350 m case. Isobaths $D=1000$, 1500, and 2000 m are shown with white contours. (c) water column thickness (wct) used for all simulations presented in this paper, with the exception of the 350 m case. Isobaths are the same as in (b). The thin grey outline mapping of the peninsula in (a)-(c) is not used in our model simulations but is shown here to provide regional context.

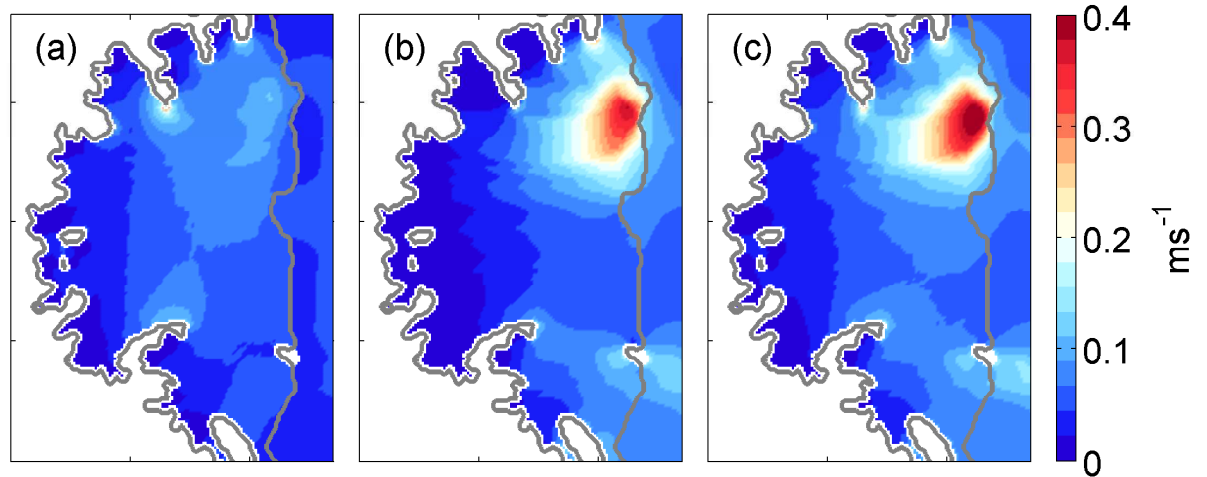


Figure 4.3: Characteristics of the tidal currents beneath LCIS. Major axis of the barotropic tidal ellipse (U_{maj}) for the largest semidiurnal and diurnal tide components (a) M_2 and (b) O_1 respectively. (c) The map of time averaged barotropic tidal current speed ($\langle |\mathbf{u}_b| \rangle_t$). All values are estimated from the last 30 days of a 40-day run with 2-hour averaged output and no thermodynamic ice-ocean exchange.

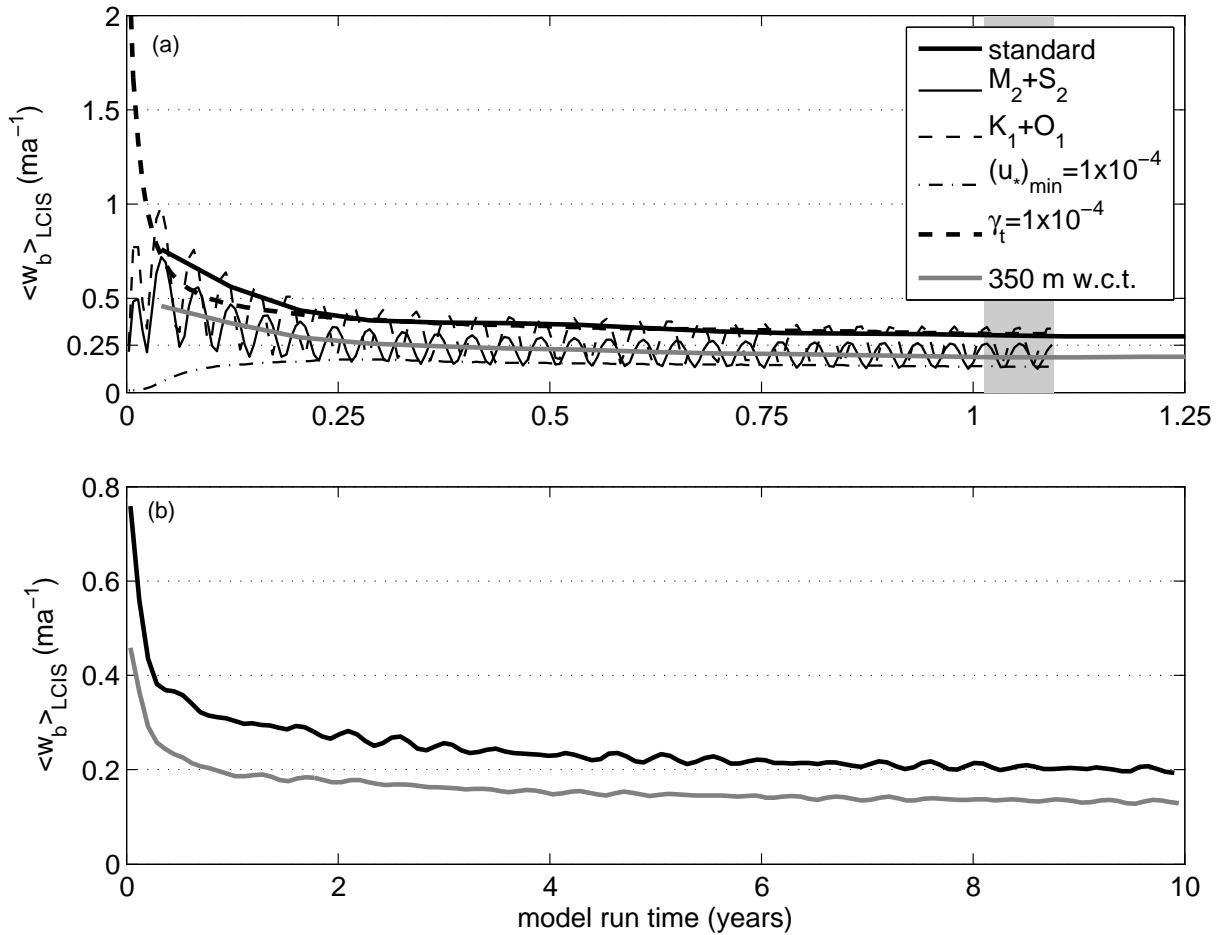


Figure 4.4: Model run equilibrations as shown by melt rate averages for LCIS. (a) The K_1+O_1 and M_2+S_2 runs output 2-day averages while all others output 30-day averages. The shaded gray region shows the time period over which results were averaged to yield melt rate maps shown in Figure 4.7. (b) Time history of LCIS 30-day averaged melt rate for the base case (black line) and 350 m *w.c.t.* test case (gray line), showing convergence to approximate steady state after 10 years.

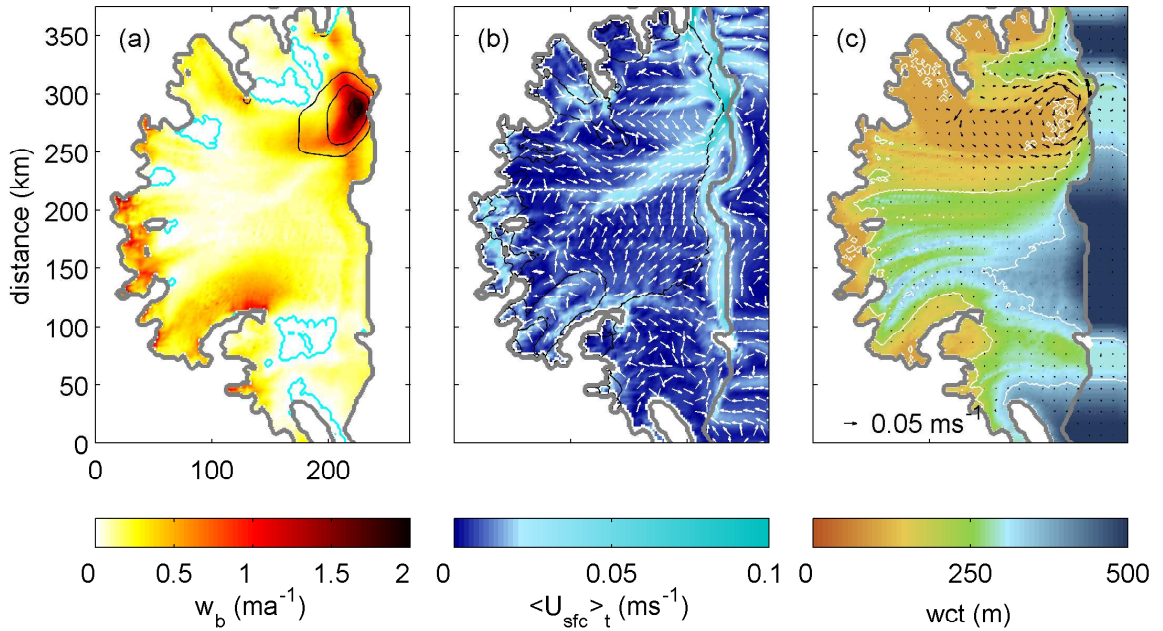


Figure 4.5: Comparison graphics of melt rate, surface current speed, water column thickness, and residual barotropic current. (a) Melt rate (w_b) for the base case averaged over the 180-day restart following the 10-year base run. Black contours show magnitude of the 30-day time averaged barotropic current speed (U_{tide} , Equation 4.6), with contour intervals at $U_{tide}=0.2, 0.3, 0.4 \text{ m s}^{-1}$. Cyan contours indicate regions where $w_b < 0 \text{ m a}^{-1}$ in the base case, i.e. locations of marine ice accretion. (b) Thermohaline and residual circulation for the base case, represented by the magnitude of the 180-day time averaged surface current vectors (color scale) with white unit vectors indicating direction. The black contours show ice draft at intervals of 600, 400, 300, and 200 m. (c) Water column thickness (wct) with white contours at 100, 200, and 350 m. The overlaying vectors show the residual barotropic circulation (\mathbf{u}_{res} , Equation 4.7), from the 30-day averages of the “no thermo” case, as in (a). These vectors are shown for the 5×5 2-D boxcar filtered values described in Section 4.4.2.

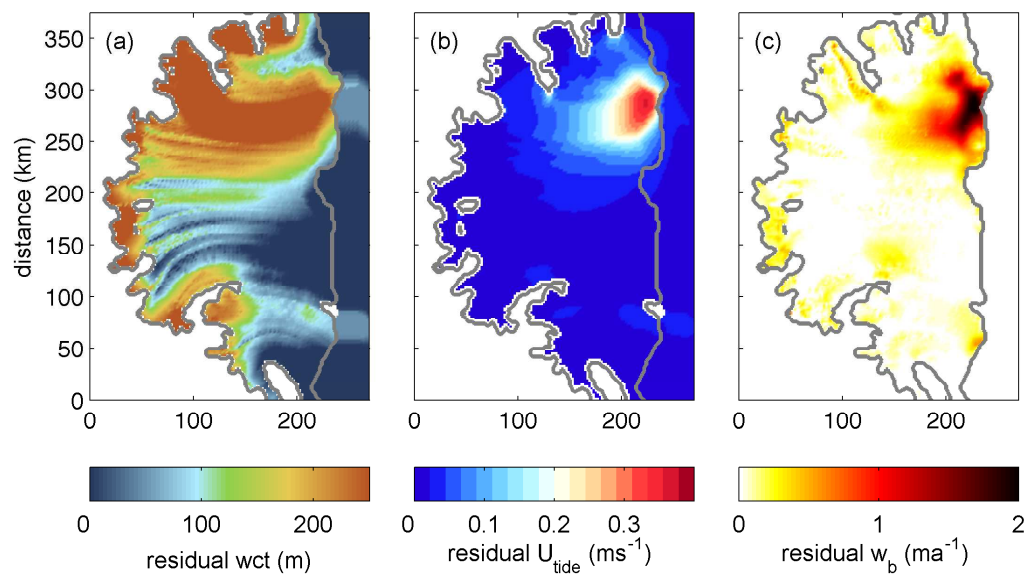


Figure 4.6: Comparison between the 350 m and base cases w_{ct} , tidal current speed, and basal melt. (a) Difference between w_{ct} for the 350 m and base cases ($w_{ct}(350 \text{ m}) - w_{ct}(\text{base})$). (b) Difference between time-averaged tidal current speed for the 350 m and base cases (positive values imply that base case currents are stronger than in the 350 m case). (c) Difference in w_b between the base and 350 m cases (i.e., $w_b(\text{base}) - w_b(350 \text{ m})$). Positive values indicate more melt in base case than in 350 m case.

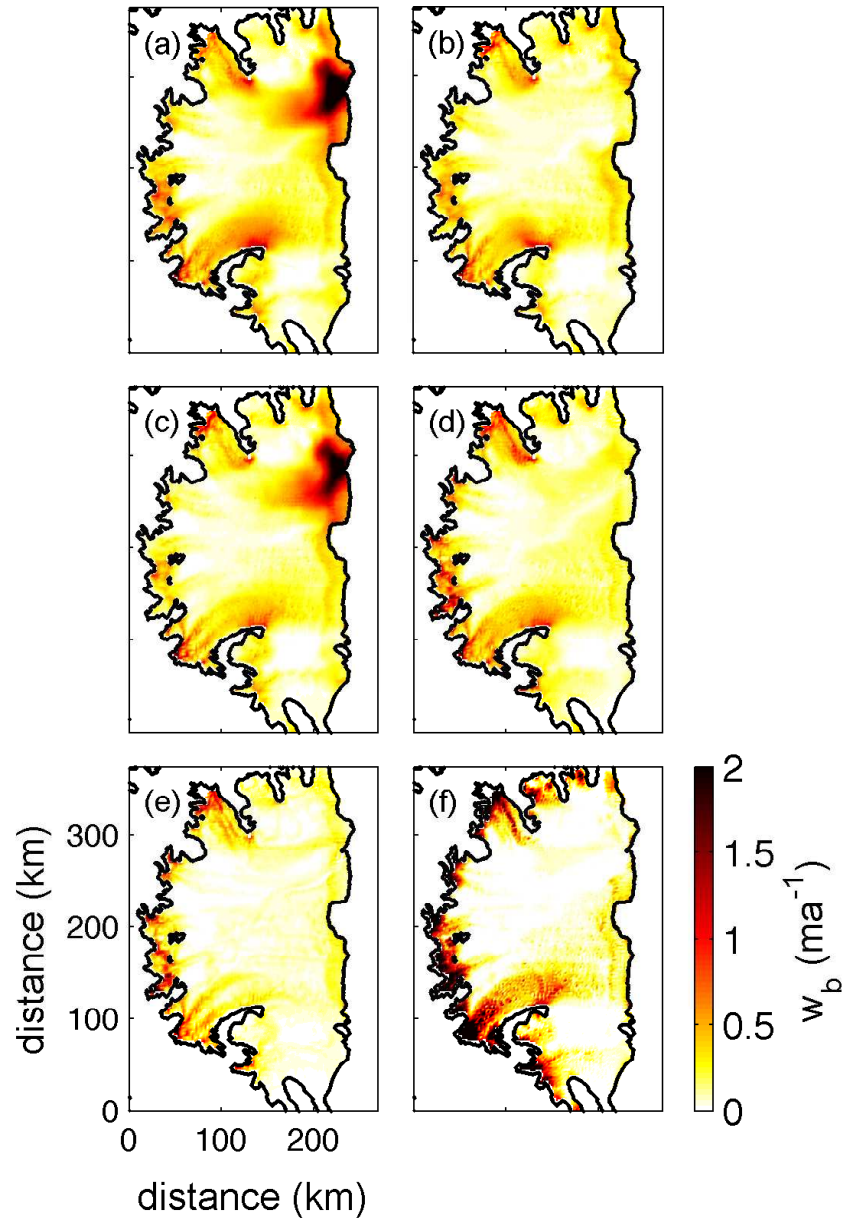


Figure 4.7: Melt rate (w_b) averaged over 30 days at ~ 1 year of model run time for cases (a) base, (b) 350 m (c) $K_1 + O_1$, (d) $M_2 + S_2$, (e) $\min u_{*o}$, (f) constant γ_t (see Table 4.3). The black contours show the ice shelf boundaries applied in our model domain. The maximum melt rate in the NE quadrant for the base case shown in (a) is $\sim 3 \text{ m a}^{-1}$.

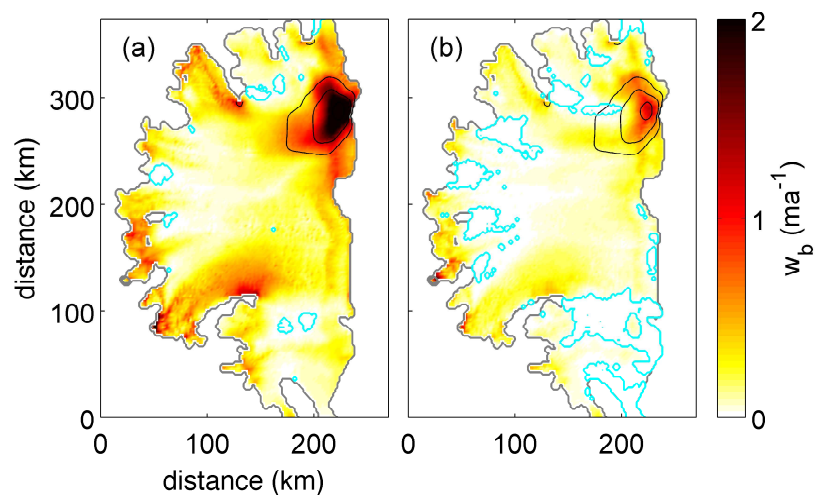


Figure 4.8: Melt rate comparison graphics for base case and cold case. (a) Similar to Figure 4.5a: Melt rate (w_b) for the base case averaged over 30-days at ~ 400 days of model run time. Black contours show magnitude of the 30-day time averaged barotropic current speed (from the “no thermo” case in Table 4.3), with contour intervals at $\langle |\mathbf{u}_b| \rangle_t = 0.2, 0.3, 0.4$ m s^{-1} . Cyan contours indicate regions where $w_b < 0$ m a^{-1} in the base case, i.e. locations of marine ice accretion. (b) w_b for the -1.9°C case averaged as in panel (a).

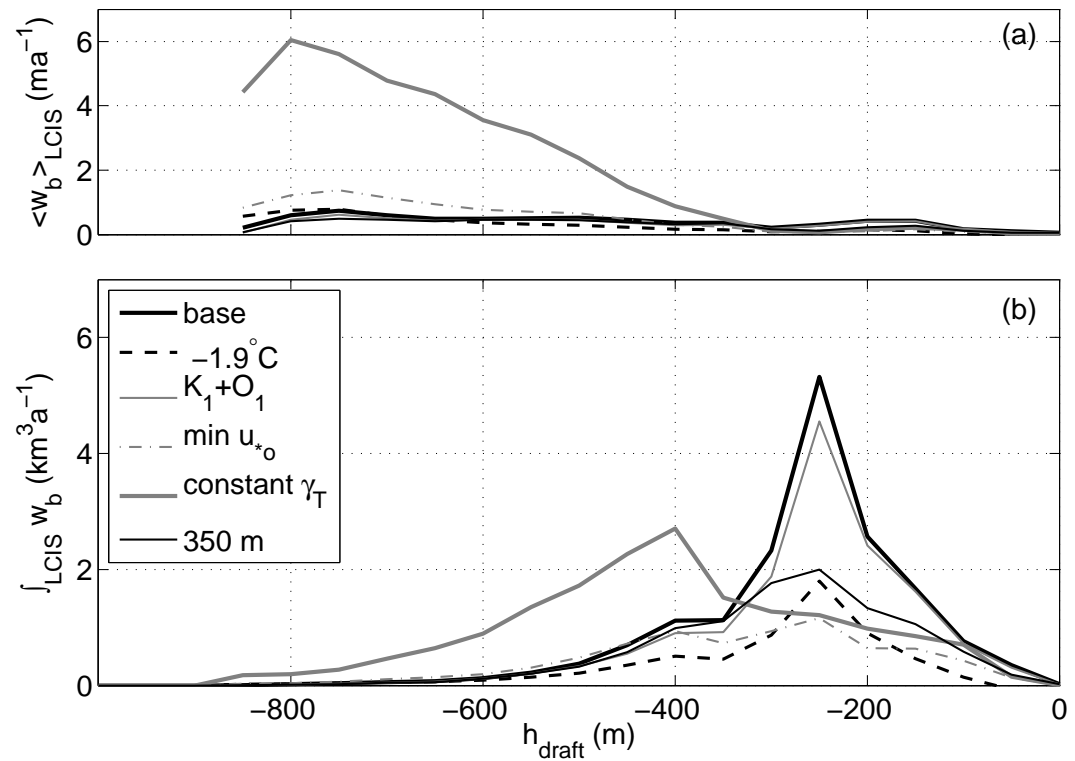


Figure 4.9: LCIS-averaged (a) and LCIS-area-integrated (b) w_b over h_{draft} bins of -1000 to -50 m in bin intervals of 50 m. The area used for averaging is shown by the dashed box in Figure 4.2a.

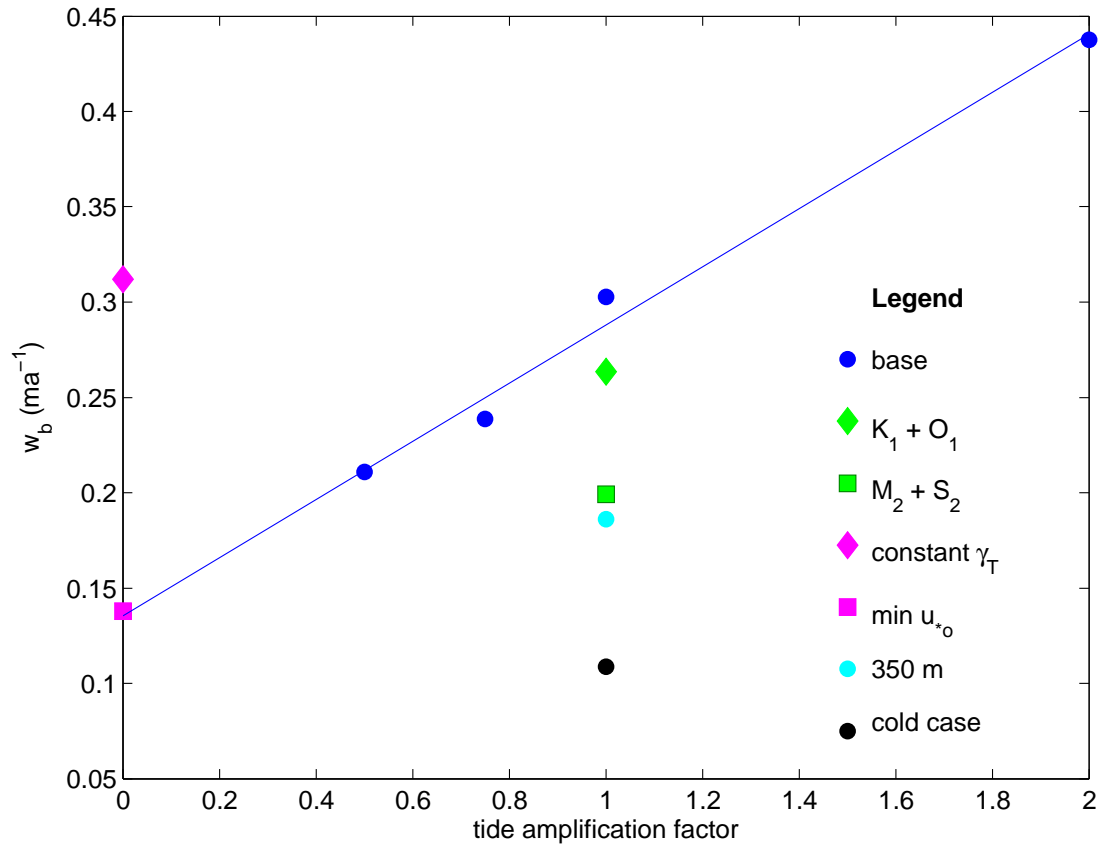


Figure 4.10: LCIS-averaged values for w_b from the same time interval shown in Figure 4.7. See Table 4.3 for details of each of these runs. All values shown here are from model run time 345-375. Blue dots are for the base setup, varying the amplification of the tide heights and currents at the forced open boundaries by tide amplification factors of 0.5, 0.75, 1 (“base case”), and 2. The blue line represents a linear least square fit through the various degrees of tide amplification.

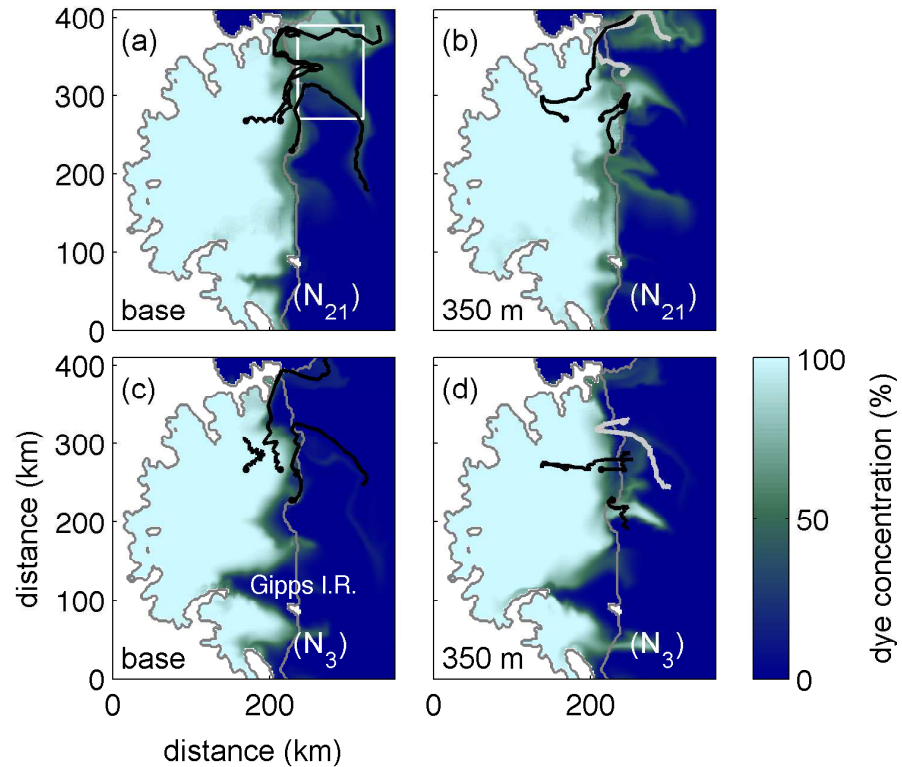


Figure 4.11: Dye concentration 180 days after being “released” at model run time of 10 years with 100% concentration beneath LCIS and 0% concentration elsewhere. (a, b) Results for the surface (N_{21}) σ -level from the base case and 350 m case, respectively. (c, d) Results for the near-bottom (N_3) σ -level from the base case and 350 m case, respectively. The black lines are float trajectories that were initialized at the same time as the dye release. These float initialized at the surface level at locations $[x,y]=[168,270]$, $[214,270]$, and $[228,230]$ km; they followed the Lagrangian flow path after release. The thick lined gray float in (b) and (d) were initialized just in front of the ice shelf at $[x,y]=[248,328]$ km.

Table 4.1: Parameter definitions used in the numerical model and abbreviations adopted in this paper.

Parameter	Symbol	Units	Value
Ocean heat flux	Q_o^T	C m s^{-1}	
Heat flux through ice shelf	Q_i^T	C m s^{-1}	0
Specific heat capacity (ocean)	c_{pw}	$\text{J kg}^{-1} \text{C}^{-1}$	3985
Latent heat	L	J kg^{-1}	3.34×10^5
Meltwater equivalent for basal melt rate	w_b	m s^{-1}	
Ice density	ρ_i	kg m^{-3}	920
Mixed layer ocean density	ρ_o	kg m^{-3}	
Drag coefficient	C_d		2.5×10^{-3}
Thermal exchange coefficient	α_h		5×10^{-3}
Double diffusion ratio	R		33
Mixed layer ocean temperature	T_o	$^{\circ}\text{C}$	
Initial ocean potential temperature	θ_0	$^{\circ}\text{C}$	
Temperature of the ice at the ice-ocean interface (equivalent to the freezing point temperature)	T_b	$^{\circ}\text{C}$	
Salinity of ice at the ice-ocean interface	S_b		
Mixed layer ocean salinity	S_o		
Ice elevation above sea level	h_{elev}	m	> 0
Ice draft below mean sea level	h_{draft}	m	< 0
Total ice thickness	$H = h_{elev} - h_{draft}$	m	> 0
Sea floor depth	D	m	> 0
Water column thickness	wct	m	> 0
Time averaged barotropic tidal current	U_{tide}	m s^{-1}	
Residual barotropic velocity vector	\mathbf{u}_{res}	m s^{-1}	

Table 4.2: Amplitude (m) and phase (degrees) values for the M_2 tidal constituent at three locations on LCIS. These locations are selected to compare with the GPS data from *King et al.* (2011); locations shown in Figure 4.1. GPS data shown in the top row. The $1 \times$ to $3 \times wct$ test cases use the forward-only (no data assimilation) mode of the barotropic tide model CATS2008a and uniformly multiply the wct by a factor of 1-3. $1 \times wct$ test case differs from the CATS2008a case in that the latter utilizes data assimilation; however, the bathymetry is the same for each of these two cases.

	LAR1		LAR2		LAR3	
	[−67.01°N, 298.49°E]		[−68.00°N, 295.71°E]		[−68.50°N, 298.00°E]	
	amplitude	phase	amplitude	phase	amplitude	phase
GPS	0.8976	250.9100	0.9654	245.2500	0.8854	242.1500
$1 \times wct$	0.9371	255.3083	1.1030	248.5347	0.9288	240.7234
$2 \times wct$	0.8918	251.3053	0.9760	245.6854	0.8847	241.3558
$3 \times wct$	0.8710	249.9547	0.9292	245.2029	0.8641	241.7842
ROMS3.2	0.7344	246.1846	0.7995	238.5865	0.7139	236.2718
CATS2008a	0.8973	255.3183	1.0386	248.7382	0.8909	240.8185

Table 4.3: An overview of tide forcing scenarios for the different runs shown in this paper.

Reference name	tidal constituents	amplification factor	θ_0	other
base	M ₂ , S ₂ , K ₁ , O ₁	1	-1.7°C	10 year plus 180 day run 30 day avg (< 10 yr) 2 day avg (> 10 yr)
cold case	M ₂ , S ₂ , K ₁ , O ₁	1	-1.9°C	600 day run
350 m	M ₂ , S ₂ , K ₁ , O ₁	1	-1.7°C	Imposed min(D) = 350 m in LCIS 10 year plus 180 day run 30 day avg (<10 yr) 2 day avg (>10 yr)
no thermo	M ₂ , S ₂ , K ₁ , O ₁	1	-1.7°C	40 day run 2 hour avg output no thermodynamics
0.5×tides	M ₂ , S ₂ , K ₁ , O ₁	0.5	-1.7°C	600 day run 30 day avg output
0.75×tides	M ₂ , S ₂ , K ₁ , O ₁	0.75	-1.7°C	600 day run 30 day avg output
2×tides	M ₂ , S ₂ , K ₁ , O ₁	2	-1.7°C	600 day run 30 day avg output
M ₂ +S ₂	M ₂ , S ₂	1	-1.7°C	400 day run 2 day avg output
K ₁ +O ₁	K ₁ , O ₁	1	-1.7°C	400 day run 2 day avg output
min u_{*o}	closed boundaries	none	-1.7°C	min(u_{*o}) = 0.0001 m s ⁻¹ 400 day run 2 day avg output
constant γ_T	closed boundaries	none	-1.7°C	$\gamma_T = 1 \times 10^{-4}$ m s ⁻¹ $\gamma_S = 5.05 \times 10^{-7}$ m s ⁻¹ 400 day run 2 day avg output

Table 4.4: Estimates of wct in meters from seismic data and an aircraft gravity survey compared to the base case bathymetry and the CATS2008a bathymetry. Location A refers to -67.98°N, 62.63°W. Location B refers to -67.50°N, 64.33°W. Location C refers to -66.92°N, 60.56°W (within high melt region in the northeast LCIS). Locations A and B are shown, respectively, as J10 and JK93 in Figure (4.1). Location C is near LAR1 of Figure (4.1) but situated within the region of high melt shown in Figure 4.5a

source	mean wct	Location A	Location B	Location C	accuracy (m)
base grid	211	284	294	100	unknown
CATS2008a	133	150	149	160	unknown
<i>Cochran and Bell</i> (2012)	376	336	315	151	
Bernd Kulesa*		412			1
<i>Jarvis and King</i> (1993)			362		

*This value is averaged between -67.95°N, 62.62°W and -68.00°N, 62.64°N to yield J10 “Location A” (B. Kulesa, personal communication, 06/16/2009).

Nonlocal effects of an evolving ice shelf topography on basal melting of the
Filchner-Ronne Ice Shelf, Antarctica

Rachael D. Mueller

Chapter 5

Abstract

Ocean heat fuels Antarctic Ice Sheet mass loss (*Rignot et al.*, 2013). This mass loss is very localized and regionally dependent with half of this mass loss occurring in regions that combine to make up only 8% of the total floating area created by “ice shelves” that float over the surrounding oceans, seaward of where the meteoric ice flows off the continent. These ice shelves that loss mass disproportionately in access of their area are in regions where warmer ocean water has access to the continental ice (*Rignot et al.*, 2013; *Pritchard et al.*, 2012) and it appears that this ocean heat is driving the mass loss. In contrast, only 15% of mass loss occurs where the continental ice overlays cooler ocean waters—with temperatures near the surface freezing point—in the Weddell and Ross seas, where the large Filchner-Ronne and Ross ice shelves reside and together make up 77% of the total area of the ocean/ice-sheet interface. However, this regional melting bias may shift in the near future. *Hellmer et al.* (2012) demonstrate that a change in atmospheric conditions within this century may shift this imbalance in melting regions by redirecting ocean currents in the Weddell Sea and allowing warmer waters to gain access the Filchner-

Ronne Ice Shelf cavity. This chapter explores the impact of this change in ocean currents using the Regional Ocean Modeling System (ROMS 3.2) to model the ocean circulation beneath the Filchner-Ronne Ice Shelf and to predict basal melting. Tidal forcing was applied at the open boundaries and two grids were used to explore tidal forcing under modern and warmer ocean conditions. The latter was created by adjusting the modern ice draft according to a map of melt rate changes, applied over a fifty year period. Results from these different grids show that cavity shape strongly affects the map of tidal currents and, hence, regional characteristics of basal melting. On average, the change in Filchner-Ronne cavity shape due to a warming ocean introduces a negative feedback where increased melting reduces the overall magnitude of tidal currents (by increasing the thickness of the water column) which then results in less basal melting; however, there are large regional variations in these results. In one region, the change in cavity shape reduces basal melting from 5 m a^{-1} to 1.5 m a^{-1} due to the corresponding change in tidal forcing; in another region, basal melting increases from 1 m a^{-1} to 1.5 m a^{-1} owing to a reduction in the upstream basal melting and, hence, a warming of inflowing water. These large regional differences in tidal forcing and basal melting in response to warmer ocean conditions and a change in ice shelf topography demonstrate that accurate maps of topography beneath ice shelves combined with the inclusion of tidal forcing in models is necessary for predictions of ice-sheet evolution under the influence of future atmosphere and ocean conditions.

5.1 Introduction

The Filchner-Ronne Ice Shelf (FRIS) in the Weddell Sea, Antarctica, accounts for 28% of the total ice shelf area surrounding Antarctica but only 10% of ice shelf basal melting, according to observations taken between 2003-2009 (*Rignot et al.*, 2013). Most melting of Antarctic ice shelves occur in the Amundsen Sea where, for example, Pine Island Glacier contributes 6% of the net Antarctic ice shelf mass loss while representing only 0.4% of total ice shelf area (*Rignot et al.*, 2013). The difference between these two regions and their corresponding contributions to melt water can be explained by the proximity of the Circumpolar Deep Water (CDW) that circulates around the entire Antarctic continent as an intermediate water within the Antarctic Circumpolar Current. This water mass, with a temperature $\sim +1^\circ\text{C}$, has direct access to the ice shelves in the Amundsen Sea while the Weddell Sea ice shelves are surrounded by colder, $\sim -1.9^\circ\text{C}$, water masses (*Pritchard et al.*, 2012).

Water mass modifications within the Weddell Sea Gyre converts the CDW that gains access in the northwest sector of the Weddell Sea into Warm Deep Water (WDW, *Fahrbach et al.* (1994)). This WDW circulates along the southern arm of the Weddell Sea Gyre, along the continental slope (*Fahrbach et al.*, 1992; *Árthun et al.*, 2012); it sits below the seasonal Antarctic Surface Water and above Weddell Sea Deep Water (*Orsi et al.*, 1993; *Fahrbach et al.*, 1994). These water masses are separated by the colder, fresher water on the continental shelf by the Antarctic Slope Front.

The combination of the Antarctic Slope Front and a wind-driven coastal current create the Antarctic Coastal Current (ACoC, *Heywood et al.* (1998)). Branches of the ACoC

transport relatively warm shelf-modified WDW (MWDW, with $T \sim -1.76^{\circ}\text{C}$ and $S < 34.50$ *Nicholls et al.* (2009)) at 32°W (*Foldvik et al.*, 1985) and 44°W (*Nicholls et al.*, 2008). As MWDW transverses the continental shelf, it is further modified into High Salinity Shelf Water (HSSW, with $T \sim -1.9^{\circ}\text{C}$ and $S < 34.75$ *Nicholls et al.* (2009)) that gains access to the FRIS sub ice shelf cavity.

The broad continental shelf in the southern Weddell Sea extends 500 km north of the FRIS ice shelf cavity with typical depths of 300-500 m and an area of around 370,000 km² (*Nicholls et al.*, 2009). In the troughs, such as the Filchner Depression, depths increase to 1800 m, serving as conduits for the landward transport of MWDW. It is over this continental shelf that contributions from the atmosphere, ice shelves and oceans align to form Weddell Sea Deep Water, the Weddell Sea source of Antarctic Bottom Water. Changes in sea ice production, ice shelf basal melting or ocean circulation can ultimately affect the production of Antarctic Bottom Water by modifying the process or the contribution(s) leading to this bottom water formation.

Changes in Weddell Sea water mass properties are already underway. Ocean temperatures in the Weddell Sea have been observed to be steadily increasing (*Robertson et al.*, 2002; *Fahrbach et al.*, 2004; *Jacobs*, 2006). This trend is likely to continue.

Hellmer et al. (2012) used two scenarios from HadCM3 model (*Gordon*, 2000) predictions to explore the impact of these changes on Weddell Sea ocean circulation. Their model results show that sea ice production decreases with warmer air temperatures, leaving the surface ocean more exposed to wind forcing. This increase in surface ocean wind stress results in a redirection of the coastal current southward toward the Filchner Ice Shelf (FIS).

By their model year 2081 (81 years after initialization), the FIS cavity interior is flooded by water with a temperatures of $> 0^{\circ}\text{C}$ while the Ronne Ice Shelf (RIS) cavity remains at cool temperature, below -1.8°C . By 2095, however, much of the RIS is also flooded with this warmer ocean water, leaving only smaller regions of colder, $< -1.8^{\circ}\text{C}$, ocean temperatures along the RIS front and some isolated grounding line regions.

The purpose of this study is to investigate the effect of this future scenario of warmer waters intruding into the FRIS cavity. Model results presented here are designed to represent how warmer waters beneath FRIS may alter cavity circulation by melting the ice shelf base and modifying tidal currents within the cavity as a result of the change in water column thickness (wct). wct is equivalent to bathymetry (h) in the open ocean and is defined as the space between h and ice draft z_{ice} within the ice shelf cavity. The hypothesis explored here is that a change in wct due to basal melting from a change in ocean temperatures introduces a feedback to ice shelf basal melting due to the influence of tidal currents on ocean and ice shelf interactions.

5.2 Methods

We use a version of the Regional Ocean Modeling System (ROMS 3.2, *Shchepetkin and McWilliams* (2009)) that has been modified to include pressure, friction and surface fluxes of heat and salt imposed by sub ice shelf cavity environments (following *Mueller et al.* (2012)). ROMS 3.2 is a hydrostatic, 3D primitive equation model with a terrain-following (σ -level) coordinate system and Arakawa-C staggered grid. Our 5 km horizontally-spaced grid covers the Weddell Sea, Antarctica, extending from 84°S to 62°S and from 99°E to

14.5°W . This domain (Figure 5.1) incorporates both the Filchner and Ronne ice shelves (FIS and RIS) in the southern portion of the domain as well as Larsen-C Ice Shelf (LCIS) along the western boundary of the domain, though the focus of this paper is on the Filchner-Ronne Ice Shelf (FRIS).

Ocean boundaries are open along the north and east, where tidal forcing is imposed using CATS_2008b (*Padman et al.*, 2002) with Flather boundary conditions for the barotropic velocity (*Flather*, 1976) and Chapman boundary conditions for the free surface height (*Chapman*, 1985). As in *Mueller et al.* (2012), Chapter 4, we impose four tidal constituents consisting of K_1 , O_1 , M_2 , and S_2 .

The bathymetry (h) over the entire domain is interpolated from RTOPO (*Timmermann et al.*, 2010). The sub ice shelf cavity environment has a static surface boundary of ice with a draft (z_{ice}) that is derived from RTOPO for FRIS and that follows *Mueller et al.* (2012) for LCIS. Two grid cells were masked to land in the NW region of LCIS as a simple modification to introduce the Bawden Ice Rise (Bawden I.R.).

Two geometries are explored in this study. One will be referred to as the “standard geometry.” This geometry represents our modern day cavity topography. The second run, referred to as “modified geometry,” represents a hypothetical future cavity shape that is adjusted from the standard geometry in response to changes in basal melting resulting from warmer ocean conditions. Both geometries are discussed in more detail below.

Standard-geometry h and z_{ice} are both smoothed to minimize pressure gradient errors. In the standard geometry, the smoothed ice draft beneath FRIS extends from -1500 m at the deepest part of the grounding line to -102 m at the most shallow region of the ice

shelf front. The water column thickness wct , defined as $h + z_{ice}$ ($z_{ice} < 0$), ranges from 50 m to 841 m. In the open ocean, wct is equivalent to h . A list of these symbols and others used through this chapter is provided in Table 5.1.

Neither wind forcing nor sea ice formation are included in this model setup. Ocean circulation is forced solely by buoyancy changes to the surface ocean from basal melting beneath the ice shelf cavity and by tidal forcing along the open boundaries. The thermohaline structure evolves from an initially uniform temperature and salinity.

The standard geometry was initialized with a uniform ocean temperature of $T_{init} = -1.9^\circ\text{C}$ and salinity of $S_{init} = 34.65$ to represent modern day conditions (this case is here after referred to as the “standard case”). Another standard geometry run was initialized with $T_{init} = -1.4^\circ\text{C}$ (no change in S_{init}) to represent a change in FRIS cavity temperatures over the coming century. This change is modest compared to the 2°C increase in T_{init} shown to penetrate FRIS by the end of this century in *Hellmer et al.* (2012); the 0.5 increase over the entire cavity represents a mean value somewhere between the 2081 and 2095 predictions shown in their Figure 2c and 2d. This standard geometry run with warmer ocean conditions will be referred to as the “standard warm case”.

Difference in melt between the standard case run and the standard warm case run is used to calculate the adjustment in ice draft due to the change in basal melting under initial conditions of a 0.5°C warmer ocean. A qualitative description of this difference in basal melting is provided in the results section (Section 5.3); here, I will simply describe how these differences were used in the method of creating a modified cavity geometry to represent an evolution in FRIS under warming conditions. The adjustment in z_{ice} due to

a change in basal melting from warmer ocean conditions assumes that other environmental changes occur over longer time scales and have a negligible impact on ice shelf mass balance for the time scales we are considering. Under this assumption, the standard geometry z_{ice} was adjusted based on 50 years of change at a fixed rate equal to the difference in basal melt/freeze between standard and standard warm cases. The resulting geometry is referred to as the modified geometry. It has a range of z_{ice} from -1452 m to -43 m and a maximum wct of 919 m (Figure 5.2).

A “modified warm case” is run with the modified geometry, $T_{init} = -1.4^{\circ}\text{C}$, and $S_{init} = 34.65$. The boundary values of h remain the same in the modified-grid as the standard-grid, so tidal forcing along boundaries is applied to the modified warm case without any modifications. Any difference in tidal currents between the standard and modified geometries is due to the effect of differences in ice draft alone. The modified warm case is used to demonstrate how warming conditions may change cavity circulation and basal melt through the influence of an evolving ice shelf topography.

The primary simulations used for analysis were run for 10 years with 30-day averaged output, a baroclinic time step of 200 s and barotropic time step of 6.7 s. Tidal currents for both the modified and standard geometries were evaluated using “tides-only” cases that were run for 40 days with 2-hour averaged output. All surface fluxes, including heat and freshwater fluxes at the base of the ice shelves, were set to zero for these “tides-only” runs, which used T_{init} and S_{init} of the standard case. Table 5.2 provides an overview of the model runs presented here.

5.3 Results

5.3.1 Tidal forcing

Tidal currents are evaluated using the barotropic current from the tides-only runs. The spatial characteristics of tidal currents are calculated as the time- and depth-averaged tidal current speed U_{tide} , as in *Mueller et al.* (2012) Figure 3, determined from

$$U_{tide} = \left\langle \sqrt{u_b^2 + v_b^2} \right\rangle_t, \quad (5.1)$$

where $u_b(x, y, t)$ and $v_b(x, y, t)$ are orthogonal components of modeled, depth-averaged current and $\langle \rangle_t$ represents temporal averaging over 35 days. A map of U_{tide} for the standard and modified tides-only runs is shown in Figure 5.3.

In general, standard geometry U_{tide} is largest (in both magnitude and extent) along a ~ 200 km band of the RIS front, where the standard geometry barotropic current reaches a maximum of 0.53 m s^{-1} in the core of the peak current (Figure 5.3a). A secondary local maximum is predicted in the South Channel (S. Channel), between Henry Ice Rise (Henry I.R.) and the Bungenstock Ice Rise (Bungenstock I.R.). The regional average here is 0.26 m s^{-1} . The average U_{tide} over the entire RIS is 0.14 m s^{-1} .

The tidal current speeds for FIS are slightly smaller, with an average of 0.12 m s^{-1} . Similar to RIS, the tides here are greatest at the ice shelf front and weakest around the Support Force and Recovery Ice Stream inlet grounding lines. In general, tidal currents are weakest along most of the grounding lines and there is a region of minimum current speeds in the channel between Berkner Is. and Henry I.R.

The barotropic currents predicted with the modified geometry differ substantially from those predicted using the standard geometry (compare Figures 5.3(a,b) and 5.4). The difference is most striking in the S. Channel region. Here, the barotropic current is reduced from a maximum of 0.54 m s^{-1} to a maximum value of 0.38 m s^{-1} , with the regional average reduction in current speed of 23%. In contrast, the northeast RIS current speeds are amplified to a maximum of 0.63 m s^{-1} in the core of the peak current. These large regional changes between the two grids are reduced in the shelf-averaged values, which is the same between the two cases: Both the standard- and modified-geometries produces shelf-averaged values of 0.14 m s^{-1} for RIS and 0.12 m s^{-1} for FIS. These equivalent magnitudes are likely coincidental and explained by a balance between a decrease in tidal currents in the S. Channel region and an increase in tidal currents in the northeast corner of RIS.

Most of the changes in tidal currents from the modified geometry occur in the RIS cavity. Not surprisingly, these changes correspond to regions of amplified basal melt (Figure 5.5a). These regions include: the S. Channel, the Carlson inlet, the region north of Doake I.R., the northeast RIS front, and the coast of the Coatsland Peninsula (along the northeastern FIS). The water column thickness increases by 64% in the S. Channel region (with a maximum change of 290% along the northeast grounding line bordering the Bungenstock I.R.), corresponding to a change in barotropic current of 0.06 m s^{-1} (a 23% reduction, as described above). The change in wct is associated with a relatively larger change in tidal currents along the northeast RIS where there is a $\sim 1\%$ increase in regional wct and a 0.06 m s^{-1} ($\sim 10\%$) increase in tidal currents.

5.3.2 General characteristics of basal melt

In all runs, shelf averaged melt rate reached a steady state within ten years, with less than 1% change in shelf-averaged melt between time steps (specifically, 0.2 - 0.7%). Ice shelf averaged melting for the standard case is 0.20 m a^{-1} (Figure 5.9). Averaged melt rates are -0.32 m a^{-1} in accretion-only areas and 0.52 m a^{-1} in ablation-only areas. The ice shelf averaged value increases to 0.72 m a^{-1} for the standard warm case (Figure 5.9). Averaged values for accretion-only regions increase by $\sim 20\%$ to -0.25 m a^{-1} while the ablation-only region doubles to 1.00 m a^{-1} . The change in cavity shape reduces the shelf averaged melt rates from 0.72 m a^{-1} in the standard warm case to 0.65 m a^{-1} in the modified warm case (Figure 5.9). Basal accretion is only slightly diminished in the modified warm case to -0.22 m a^{-1} while ablation is reduced to 0.86 m a^{-1} . In general, FRIS-averaged melt rates increased by $\sim 260\%$ with a change in T_{init} from -1.9°C to -1.4°C and by $\sim 230\%$ with a change in both T_{init} and cavity geometry.

Warming the ocean from $T_{init} = -1.9^\circ\text{C}$ to -1.4°C leads to a 25% reduction in freezing rates in accretion regions. Warming the ocean together with changing the cavity shape leads to a 30% reduction in freezing rates in accretion-only regions. A much greater difference between grids is demonstrated by the averaged melt rates in the ablation regions. Melt in ablation regions increases by 95% when T_{init} is increased by 0.5°C and by only 64% when both T_{init} is increased by this amount and cavity geometry has been modified in response to melting.

Near grounding lines, the pressure dependence of basal melting acts to enhance melting independent of the weak tidal currents in these areas (Figure 5.5). For example,

near a deep grounding line such as in the Foundation embayment, the pressure-dependent melt is of a similar magnitude to that in regions with tidal currents around $\sim 0.2 \text{ m s}^{-1}$ within FIS. In other areas, such as the S. Channel, strong tidal currents (Figure 5.6a) result in enhanced melt rates (Figures 5.6b). Large areas of basal accretion (melt rates < 0) exist in the central cavity of RIS, along the northwest flank of RIS, and along the northeast RIS front (Figures 5.5(a,b,c)).

The northeast RIS cavity also supports a region of amplified tidal currents (Figure 5.6a), but strong tidal currents in this region do not correlate with amplified melt rates (Figure 5.6b). Thermal forcing in this region is much less than in the S. Channel region ($\sim 0.45^\circ\text{C}$ in northeast RIS compared to $\sim 1.0^\circ\text{C}$ in S. Channel). The amplified tidal currents in the northeast RIS are not sufficiently large to amplify basal melt under these thermal forcing conditions.

The spatial distribution of basal melt for the standard warm case is similar to the melt distribution of the standard case, except that the extent of accretion is smaller and the melt rates are larger in the standard warm case (compare Figures 5.5(a) and 5.5(b)). This melt distribution changes when an increase in T_{init} is also accompanied by a melt-adjusted geometry (compare Figures 5.5(b) and 5.5(c)). Although accretion regions remain largely the same, the regions of strong basal melting in the S. Channel and northeast FIS are significantly reduced (Figures 5.8). Figure 5.6 shows maps of (a) the barotropic tidal current and (b) and basal melt, demonstrating the relationship between tidal currents and melting in the S. Channel. Comparing this figure to Figure 5.7 shows how a reduction in basal melt in the S. Channel can be attributed to the reduction in tidal currents. In some

regions, such as the Rutford inlet, basal melting increases with the modified geometry (see Section 5.3.3 for further explanation).

5.3.3 Regional melt characteristics

The affect of grid modification on steady state solutions varies greatly between different regions (Figure 5.10). For example, in the Foundation inlet region, melt rates increases by 216% when the standard case T_{init} is increased from -1.9°C to -1.4°C but then shows very little change when the -1.4°C case is repeated using the modified geometry (Figure 5.11). This effect differs from that predicted in the Institute, Möller, and Rutford regions, which show an increased in basal melting under warm conditions that is then reinforced (doubled) when the grid is modified (Figure 5.11). Much larger changes in melt rates are introduced by the modified geometry in the S. Channel region. Here, the melt rate is doubled under warmer T_{init} conditions but then decreased to almost half the value of the -1.9°C case in the modified geometry case (Figure 5.11). The positive feedback between change in cavity geometry and basal melting along grounding lines west of the S. Channel (e.g. Rutford) is attributed to reduced tidal mixing and an increase in stratification that allows temperatures near the value of T_{init} to flow through the S. Channel in the bottom 100 meters (not shown). The S. Channel serves as a “bottleneck” in our runs in which down stream melting is strongly influenced by the tidal currents and mixing in this region.

In addition to the differences in magnitude of melt rates, there are also significant differences in the length of time required to reach regional steady state. The region around the Möller inlet reaches a steady state in under one year (Figure 5.10c) while the Rutford inlet region never reaches steady state for the standard geometry (Figure 5.10f). Although

not shown here, the Rutford inlet region melt levels out just after 10 years and reaches steady state in a model run extended to 15 years. In general, the melt characteristics do not differ significantly at fifteen years as from those shown here but the melt rate magnitude for the Rutford inlet region is less at 15 years than 10 years for both the standard and standard warm cases.

These differences in regional melt and steady state solutions indicate that there is a large, dynamic feedback between ocean temperature, cavity geometry and melt rate, which includes both local and non-local effects. Large regional differences in ocean temperatures or ice-ocean feedbacks for individual ice streams are important because they may impact outflow of grounded ice from specific catchments.

5.3.4 Regional heat flux and flow

Differences in average temperature, velocity, and heat flux across six different transects are used to evaluate local and non-local effects from the changes in T_{init} and the modified grid on cavity circulation. The six transects are located at or near (1) The FIS front (*FIS*), (2) Across the Filchner channel south of Berkner Is. (*S. Berkner*), (3) Between Henry I.R. and Berkner Is. (*Henry to Berkner*), (4) across the S. Channel at a location north of the eastern part of Bungenstock I.R. (*E. BIR*), (5) across the S. Channel at a location north of the western side of Bungenstock I.R. (*W. BIR*), and (6) across the RIS (*RIS*). The locations of these transects are shown in Figure 5.12.

The heat flux across the transects (Q_T^{trans}) was calculated according to

$$Q_T^{trans} = \left\langle \sum_x \sum_z \rho_o c_{po} (T_o - T_{ref}) u_{\perp} A \right\rangle_t \quad (5.2)$$

where $u_{\perp}(x, z, t)$ is the velocity perpendicular to the transect and $A(x, z)$ is the cross-sectional area of each grid cell. Values of $\rho_o(x, z, t)$, c_{po} , and A are always positive, $T_o(x, z, t)$ is always negative, and u_{\perp} is either positive or negative. The reference temperature, T_{ref} , is set to 0°C. The magnitude of the heat flux increases as temperature becomes more negative due to surface cooling, and a positive heat flux indicates that velocity is negative as well and that the direction of flow is either south or west. After the heat flux is calculated for every grid cell, it is then summed across the transect for every time step. This integrated value is then averaged over the last year of the model run to yield a representative value of net heat flux across the transects. Figure 5.12 shows the direction of the heat transport in green arrows. The magnitude of heat flux is shown within the green arrows in Figure 5.12 and in Figure 5.13. Larger values of heat flux magnitude indicates either cooler ocean temperatures and/or an increase in southward or westward velocities.

Heat flux across transects for all model runs is shown in Figure 5.13. The flux through *FIS* is relatively unaffected by changes in T_{init} and cavity geometry, though the flux through *RIS* is strengthened by an increase in T_{init} , indicating more cold meltwater advection. The greatest variability between cases is in the interior transects *Henry to Berkner*, *E. BIR*, and *W. BIR*. This regional sensitivity is more clearly demonstrated in Figure 5.14, which shows the transect fluxes normalized by transect area. Percent change in transect area between the standard and modified cases is shown for each transect in Table 5.6 (transect area being the same for the standard cases). Per unit area, the heat

is similarly concentrated and the transport is greatest across *W. BIR* with *E. BIR*. The change in geometry reinforces the effect of warmer T_{init} on heat flux for the *Henry to Berkner* and *E. BIR* transects. In all other cases, the change in cavity shape changes either the magnitude or direction of the feedback from an increased T_{init} on the cross-transect fluxes.

The influence of T_{init} alone vs. T_{init} and modified geometry is more clearly shown in reference to the standard case (Figure 5.15). This figure shows the difference in normalized fluxes between the two -1.4°C cases (with different geometries) and the -1.9°C case. The differences at *FIS* and *RIS* are much smaller than the differences in the interior transects. The normalized heat flux across *Henry to Berkner* is nearly doubled by a change in cavity shape and of opposite sign (direction) as the standard case (see Figure 5.13). At *E. BIR*, the heat flux is made more negative by more than 10 times the reduction produced by increase in temperature alone. Along *W. BIR*, the change in T_{init} strengthens the heat flux by $\sim 15 \text{ kW m}^{-2}$ but a change in ice draft reverses this increase and reduces the heat flux below the standard case values by -50 kW m^{-2} .

These regional difference in heat flux across transects between the two -1.4°C cases is best explained by changes in advection. Figure 5.16 shows the deviations in transect average temperature between the standard -1.9°C case and the two -1.4°C cases, using both standard- and modified- geometries. Both cases show that the average inflowing temperature across *FIS* is 0.42°C higher than the $T_{init} = -1.9^{\circ}\text{C}$ case. This difference is 84% the 0.5°C difference in T_{init} . The temperature difference from the -1.9°C case becomes larger at *S. Berkner* and *Henry to Berkner* with the latter demonstrating a temperature

difference that is greater than the difference in T_{init} . Both a change in advection pathways and relative contribution of meltwater and lower layer “warm” water contribute to this larger increase in temperature. The temperature differences from the standard case decreases as circulation continues westward through the S. Channel, bordered by *E. BIR* and *W. BIR*, on toward the *RIS* transect. The biggest difference in average temperature between the standard and modified cases is seen at the *W. BIR* transect, where the average temperature of the standard warm case is warmer than the $T_{init} = -1.9^{\circ}\text{C}$ standard case by 0.39°C and the average temperature of the modified warm case is warmer than the $T_{init} = -1.4^{\circ}\text{C}$ standard case by 0.12°C . This 0.12°C change in the average temperature at *W. BIR* between standard- and modified-geometries is a steep increase from the $0 - 0.04^{\circ}\text{C}$ differences seen in the transects upstream of *W. BIR*. The difference between these cases reduces back down to 0.03°C across the *RIS*, where the temperature difference between the standard and -1.4°C cases is only $\sim 0.1^{\circ}\text{C}$, much reduced from the 0.42°C difference in inflow temperatures across *FIS*. This small difference in average temperature across the *RIS* transect, compared to the larger difference across the *FIS* front, demonstrates the efficiency of this ice shelf in “absorbing” most of the inflowing oceanic heat by converting sensible heat to latent heat via melting at the ice shelf base.

The average velocities across the transects are much more variable within the cavity than the average temperatures (Figures 5.17). Velocities across *FIS* are reduced and, in fact, change direction from the -1.9°C case to have, on average, a net inflow rather than outflow. This difference is evident in comparing the 12-month average barotropic current between the two cases, as in Figure 5.18; the inflow (blue) along the eastern *FIS* is strengthened

with the 0.5°C increase in initial temperature, and the outflow along Berkner Is. is less affected by the change in initial temperature (Figure 5.19(a,b)). This increase in inflow may account for why the heat transport across the *FIS* is relatively stable in spite of the increase in T_{init} (Figures 5.14). In other words, the change to less negative (warmer) ocean temperatures is compensated by the more negative (stronger) inflowing velocities. This change persists with the modified geometry, although the strength of the inflowing current is reduced compared to the standard geometry case with comparable initial temperature (compare Figure 5.19(b,c)).

Further south in FIS, average velocities show a stronger westward flow at *S. Berkner* in both cases with $T_{init} = -1.4^{\circ}\text{C}$, with average flow reversing from southward to northward across the *Henry to Berkner* transect (Figure 5.17). Figure 5.19 shows that the westward(d,e) and northward(a,b) currents in the channels to the south and west of Berkner are strengthened when the initial ocean temperature increases by 0.5°C using the standard geometry. The effect of the modified geometry is to amplify the affect of increased T_{init} on the mean velocity across these transects (Figure 5.18), however, the circulation dynamics behind this change are different for the standard- and modified-geometries. In the standard geometry, the circulation pathways of the -1.9°C case are strengthened by an increase in ocean temperature (Figure 5.19(a,b) and (d,e)); in the modified warm case, the circulation pathways change in comparison to those of the standard warm case, with an introduction of recirculating flow in the channel between Berkner Is. and Henry I.R. (Figure 5.19(c,f)).

The result that the change in cavity shape reinforces the influence of an increased

T_{init} in the fluxes across *S. Berkner* and *Henry to Berkner* is unique to these transects. Along the S. Channel, the change in ice draft has the opposite affect on average velocities than an increase in T_{init} . On average, the westward velocities are strengthened by 0.27 cm s^{-1} across *E. BIR* and 0.47 cm s^{-1} across *W. BIR* with an increase in T_{init} from -1.9°C to -1.4°C (Figure 5.18). The mean velocity then reduces in westward magnitude by almost 1 cm s^{-1} and 0.61 cm s^{-1} across *E. BIR* and *W. BIR* in the case of the modified ice draft grid. The flow across the *RIS* is strengthened in the northward direction for both the -1.4°C cases but less so for the modified geometry than the standard geometry (Figure 5.17).

In general, the change in heat flux across the transects is more strongly affected by the change in average velocity (compare Figures 5.14 and 5.17) than temperature (Figure 5.16). For example, both the average velocity and the heat flux across *Henry to Berkner* changes sign and increases in magnitude with increased T_{init} and grid modification. The pattern is similar at *W. BIR* and *RIS*. These consistencies between changes in velocity and fluxes indicate that circulation pathways dominate the change in magnitude of heat transport more than changes in temperature due to basal melting.

5.3.5 Mass balance along flow lines

The affect of T_{init} , tides, or advection on ice shelf stability is explored here by evaluating the change in ice shelf mass along the ice flow lines shown in Figure 5.20¹. Given that most of the melt occurs at or near the grounding line, this value is used here as a proxy for how change in basal melt at the grounding line might affect ice shelf rheology.

¹Flow lines were provided by Dr. Geir Moholdt on May 31, 2013 (*Moholdt et al.*, in review)

Mass change from basal melt (w_b , m a^{-1}) was calculated according to $M_b = (w_b A \rho_i) 1 \times 10^{-12} \text{ Gt a}^{-1}$. Maps of mass change for the standard case, the standard warm case, and the modified warm case are shown in Figure 5.20. These maps were then integrated along the black flow lines in Figure 5.20 to yield a value for net mass adjustment along streamlines. The integrated values, numbered according to the flow lines shown in Figure 5.20, are shown (Figure 5.21).

The total mass accumulation or loss along streamlines was calculated for all three cases (Figure 5.21). Negative values indicate that there is a net mass loss along the flow lines that could contribute to a draw down of the upstream glaciers and ice streams. This study assumes that any change in ice thickness from basal melt or freeze is compensated by mass accumulation, advection, convergence or divergence such that the ice shelf draft remains steady in time. These results are described with the same assumption applied. As such, an increase in ice shelf mass is considered to have a stabilizing affect on the upstream ice while a decrease in mass is considered to have destabilizing affect on the upstream ice.

Figure 5.21 shows distinct regions where ice shelf mass loss and gain could have a significant influence on ice shelf stability (e.g. calving). In order to better represent the influence of T_{init} vs. cavity shape on this influence, the values were differenced between: (1) the standard case (blue in Figure 5.21) and standard warm case (magenta in Figure 5.21), and (2) between the standard warm case (magenta) and the modified warm case (green). These results are shown in Figure 5.22, where the difference between the standard case and the standard warm case is shown by the purple dots while the difference between the standard warm case and the modified warm case is shown in light green. Positive values

for purple dots indicate that more mass is accumulated along flow lines in the standard case than in the standard warm case. These positive values indicate the degree to which an increase in T_{init} will enhance melt and affect ice rheology. Positive values for the green dots indicate stream lines where there is more accumulation for the standard warm case than for the modified warm case. Positive values in this case indicate that a change in geometry will enhance melt and affect ice rheology. Given that most basal melting occurs in the grounding line region, these values are considered a proxy for the influence of grounding line melt on ice shelf stability.

Change in T_{init} has a significant effect on the mass balance along flow lines extending from the Carlson Ice Stream, Rutford Ice Stream, Institute Ice Stream, Möller Ice Stream and Foundation Ice Stream (Figure 5.22). The Carlson and Rutford flow lines show a variable response to increasing T_{init} by 0.5°C , with mass loss ranging from $\sim 1-5 \text{ Gt a}^{-1}$. The influence of the change in ice draft amplifies this response by the same magnitude, although the degree of sensitivity varies from one stream line to the next in this region. The two flow lines extending from the Institute Ice Stream both show a $\sim 5 \text{ Gt a}^{-1}$ increase in mass loss with the 0.5°C increase in T_{init} but a negligible change in mass loss due to change in ice draft. The Möller Ice Stream flow lines show a similar sensitivity to T_{init} as the Institute flow lines, but a variable sensitivity to change in ice draft; some flow lines extending from Möller are stabilized by a change in ice draft while others are further destabilized by a change in ice draft, all within a range of $\pm 3 \text{ Gt a}^{-1}$. The Foundation Ice Stream flow lines are split into those that flow to the west of Berkner Is. and those that flow to the east of Berkner Is. The flow lines on the western side are quite sensitive to change in T_{init} ,

with a $\sim 7 \text{ Gt a}^{-1}$ response to change in T_{init} , but they are not sensitive to a change in ice draft. The eastern flow lines have the greatest sensitivity, with a change of $\sim 10 \text{ Gt a}^{-1}$ in response to the 0.5°C increase in T_{init} and a variable response due to the change in ice draft. Lastly, the Filchner flow lines are unique in that they show a rather uniform response of $\sim 2 \text{ Gt a}^{-1}$ mass loss with increased T_{init} and a somewhat mirrored response of $\sim 1 \text{ Gt a}^{-1}$ mass gain with a change in ice draft that suggests that a change in cavity shape due to basal melting will help to buffer the Filchner Ice Shelf from the destabilizing effect of a warming ocean.

There are three regions that are distinctly insensitive to either a change in T_{init} or ice draft. These regions are labeled in Figure 5.22 as “Evans”, “Ice Rise shadow” and “Berkner”. They correspond to ice flow lines that originate at the Evans Ice Stream inlet, the northern part of the “island” in the central RIS and the northern part of Berkner Is. Among these, the most meaningful result is that of the Evans Ice Stream, where changes in T_{init} and ice draft have little effect on mass balance along flow lines. The lack of response in the Ice Rise “shadow” indicates that the central RIS is not sensitive to a change in ocean inflow temperatures or cavity shape but our model “island” blocks streamlines that likely extend all the way to the back of the cavity. The “island” is a conglomerate of Korff Ice Rise, Doake Ice Rumples and Henry Ice Rise. The ice rumples in the middle of the two ice rises is a region where the ice shelf is grounded on bedrock to the degree that it deflects flow direction from surrounding ice but not to the degree of the two ice rises, which decouple and possibly reverse the flow direction from the adjacent ice. As such, it’s hard to interpret the flow of ice through this region and how it relates to the grounded ice in the back of

the cavity. The information presented here of mass balance along flow lines in this region is incomplete. The other region of little effect includes the very short flow lines around Berkner Is. (Figure 5.20).

This wide range in mass loss and accumulation along flow lines suggests that a change in ocean temperature may affect ice sheet dynamics through changes in grounding line melt and also through changes in internal strain and shear within the ice, leading to spatially variable distribution of change in the ice shelf buttressing effect on the upstream, grounded ice.

5.4 Discussion

The results presented here demonstrate that shelf-averaged basal melt is strongly affected by T_{init} but weakly affected by changes in cavity geometry (Figure 5.9). Shelf-averaged melt rate values are a common metric for evaluating ice shelf mass balance and are useful for comparing with a wide range of observations and other modeling studies (Figure 5.23). However, shelf-averaged values don't capture the significant, variable regional responses in basal melt that are introduced by the change in cavity geometry. These regional-melt characteristics are important for predicting ice sheet dynamics as well as the water mass characteristics of the meltwater outflow that serves as a precursor to Antarctic Bottom Water production. This section describes both general and regional characteristics of basal melting.

5.4.1 Ice-shelf-averaged basal melt

The model results presented here show FRIS-averaged basal melting of 0.20 m a^{-1} for the standard case. The range of plausible values reported by other studies extends from the lower bound in *Depoorter et al.* (2013) of 0.03 m a^{-1} to 0.55 m a^{-1} (*Jenkins, 1991; Jacobs et al., 1992*) (Figure 5.23). Our value is most closely approximated by *Joughin and Padman* (2003), *Makinson et al.* (2011), *Foldvik et al.* (2001) and the upper bound of *Gammelsrød et al.* (1994). It falls within the lower bounds of the recent estimates derived from satellite observations that are described in *Moholdt et al.* (in review) and *Rignot et al.* (2013) and at the upper bound of the estimate given by *Depoorter et al.* (2013).

FRIS-averaged values increase from 0.20 m a^{-1} to 0.72 m a^{-1} when T_{init} increases from -1.9°C to -1.4°C for the standard warm case. Changing the cavity shape for the modified warm case has a small (10%) affect on the shelf-averaged basal melting rate, reducing it by 0.06 m a^{-1} to 0.66 m a^{-1} .

5.4.2 Regional basal melt, with implications for ice sheet mass balance

Of the four grounding line (GL) regions explored in this study, the Foundation Ice Stream GL region has the highest averaged melt rate of $\sim 1.5 \text{ m a}^{-1}$ (Figure 5.10b). Basal melt there is highly sensitive to a change in T_{init} from -1.9°C to -1.4°C ; it doubles from $\sim 1.5 \text{ m a}^{-1}$ to $\sim 3.3 \text{ m a}^{-1}$ (Figure 5.11). This sensitivity to T_{init} is consistent for both the standard- and modified-geometries, with little difference in basal melting between the two grids. This sensitivity to change in initial ocean temperatures but insensitivity to cavity shape is also apparent in the change in mass balance along the western Foundation flow lines.

The eastern Foundation flow lines show a sensitivity to both T_{init} and grid modification. This degree of basal melting is much less than the basal melting demonstrated by Wright et al. (in review) to be required to accelerate a change in GL retreat at Foundation. The model results presented here show that the Foundation Ice Stream inlet has a prominent role in converting FRIS ocean heat to meltwater. This result, combined with the Wright et al. (in review) result that the Foundation Ice Stream GL is insensitive to melting, suggests that basal melting in this region is important for how it preconditions ocean temperatures and, hence, GL melt in down-stream locations rather than having a direct impact on local GL retreat.

Both Institute and Möller show the least amount of basal melting (around 0.3 m a^{-1}) for the standard case with $T_{init} = -1.9^\circ\text{C}$ (Figure 5.10c,e, 5.11). The 0.5°C increase in T_{init} increases the Institute GL region melt rate to $\sim 1 \text{ m a}^{-1}$ and the Möller GL region melt rate to $\sim 0.6 \text{ m a}^{-1}$ (Figure 5.11). Modifying the ice draft augments melting further to 1.75 m a^{-1} and 1 m a^{-1} , respectively. The grounding lines in these regions appear to be very sensitive to changes in T_{init} and changes in the cavity ocean circulation imposed by a change in model geometry. Change in T_{init} introduces a 2- to 3-fold increase in melt at Möller and Institute while a change in both T_{init} and cavity geometry introduces a 3- to 6-fold increase (Institute being the more strongly affected of the two).

This regional sensitivity to T_{init} for both Institute and Möller is further demonstrated by the integrated mass accumulation along the streamlines that originate at these ice stream grounding line regions (Figure 5.20). All flow lines to these ice streams seem to increase mass by $\sim 5 \text{ Gt a}^{-1}$ from the standard case. The accumulation over the Institute

flow lines is more variable than over the Möller flow lines, but the change in ice geometry has negligible effect on mass accumulation along these flow lines. This result suggests that, although the Institute GL melt rate is sensitive to both T_{init} and a change in cavity shape, the impact of this change on the downstream rheology of the ice shelf is only sensitive to T_{init} .

The Möller Ice Stream, on the other hand, shows a fairly uniform response to T_{init} along flow lines but a variable response to a change in ice draft (Figure 5.20). The flow lines on the western side of Möller Ice Stream are buffered against basal mass loss with a change in cavity shape of the modified-grid. These flow lines go near the south channel; hence, the difference between standard- and modified-grids for these flow lines is likely from the the reduction in basal melting with the south channel alone. The more eastern flow lines, on the other hand, experience more mass loss due to the change in cavity-shape.

Rutford Ice Stream GL melt rate is amplified both by an increase in T_{init} and the change in cavity shape between standard- and modified-grids (Figure 5.10f). Although the increase in T_{init} between the standard and standard warm case increases melt to $\sim 2.5 \text{ m a}^{-1}$, melt values remain below those at Foundation. A significant effect of the change in cavity with the modified-grid is to amplify melt in the Rutford Ice Stream region to $\sim 4 \text{ m a}^{-1}$, which is greater than the $\sim 3.25 \text{ m a}^{-1}$ predicted around Foundation. This result is robust out to a steady state at 15 years although the standard case and standard geometry with $T_{init} = -1.4^\circ\text{C}$ has less melt and, hence, a larger difference between these and the modified-grid with $T_{init} = -1.4^\circ\text{C}$ (not shown). Mass balance along the flow lines originating from the Rutford GL demonstrate a similar change to that of regional melt in

which mass loss is reinforced both by the increase in T_{init} and change in cavity geometry (Figure 5.20).

In general, the model results presented here demonstrate that changes in cavity-geometry, and the corresponding affect on tidal current speeds, have a large impact on grounding line basal melt and the buttressing of ice streams near or down-stream of the S. Channel. Evans Ice Stream is the exception in that it is not affected by either T_{init} or cavity geometry (Figure 5.23); change in ocean heat within the Evans Ice Stream inlet is buffered by efficiency of the ice shelf in converting ocean heat to meltwater (e.g. Figure 5.16). Part of this buffering is from the increased melt in the Institute and Rutford grounding zones. The temperature of the water inflowing to the Institute GL changes from -2.4°C to -2.1°C and -1.8°C from the standard case to the standard geometry with $T_{init} = -1.4^{\circ}\text{C}$ and modified geometry with $T_{init} = -1.4^{\circ}\text{C}$ (not shown. Values approximated from transect graphic).

The spatial distribution of GL melt response to T_{init} and cavity shape is important because Wright et al. (in review) use the BISICLES ice sheet model to demonstrate that the ice streams tributaries flowing into FRIS respond differently to changes in GL melt. They found that the Institute and Möller ice streams are most sensitive to changes in basal mass balance due to a warmer ocean. These two ice streams rest on top of steep reverse bed slopes with low basal roughness, conditions which have been shown to contribute to grounding line instability and retreat (Schoof, 2007). Wright et al. (in review) verify this destabilizing effect for Institute and Möller. Not only were these two ice streams sensitive to changes in basal melting due to increased ocean temperatures, but they were also sensitive to changes in the buttressing effect from melting around Henry and Korff Ice Rises and an

increase in basal sliding over these ice rises. The sensitivity of these ice streams to changes in basal conditions was diminished by an increase in surface accumulation, although grounding line retreat persisted, demonstrating that basal melting at the grounding lines of these two ice streams is a dominant factor in determining the rate and degree of grounding line retreat. The other ice streams flowing into FRIS were shown to be less sensitive to changes in basal melting in their model results.

These results combined with those from Wright et al. (in review) indicate that correctly predicting the evolution of the Antarctic Ice Sheet in response to oceanic warming will require not only accurate assessments of inflow temperatures but also an understanding of how these changes in inflow temperatures affect basal melting and wct within the ice shelf cavity. Changes in wct in response to increased basal melting from warming ocean temperatures were shown here to have a buffering or amplifying affect on both basal melting and ice stream buttressing that is location-dependent. It will be impossible to predict the true affect of oceanic warming on grounding line retreat and ice stream velocities without a better understanding of the cavity shape and its evolution.

5.5 Conclusions

The aim of this study was to demonstrate how plausible changes in ocean heat in response to climate change may influence Filchner-Ronne Ice Shelf cavity circulation due to the feedback between ice shelf topography and tidal currents. The standard case runs utilized a geometry based on modern estimates of ice draft and bathymetry. Two cases were run with this geometry, one with $T_{init} = -1.9^{\circ}\text{C}$ (“standard case”) and another

with $T_{init} = -1.4^{\circ}\text{C}$ (“standard warm case”). The difference in basal melting between these two cases was used to evolve the sub ice shelf topography to create a geometry that could represent the result of 50 years of melting under warmer ocean conditions. The new “modified” geometry was run with $T_{init} = -1.4^{\circ}\text{C}$ (“modified warm case”) to ascertain the effect of topography changes on cavity circulation by comparing these results with those from the standard warm case.

Some assumptions inherent in this approach are that: (1) changes in cavity shape due to ocean warming will affect sub ice shelf topography over much shorter time scales than ice shelf advection into and in the ice shelf, and (2) surface accumulation varies over time scales much longer than ocean warming.

Model results presented here demonstrate that a change of 0.5°C in ocean temperature has a significant influence on FRIS-averaged basal melt rate, which increases from 0.2 m a^{-1} to 0.72 m a^{-1} . Changing the cavity shape introduces a negative feedback that reduces the shelf-averaged melt rate by about 10% to 0.66 m a^{-1} . In spite of this small difference in shelf-averaged melt rates between standard warm and modified warm case results, regional changes in basal melting are strongly affected by change in cavity shape.

The most striking differences in basal melt between the standard warm and modified warm cases are in channel south of Henry Ice Rise (“S. Channel”). Here, increased wct leads to a 23% reduction in tidal forcing. This reduction in tidal forcing is accompanied by reduction in melt rates in this region by 70% (Figure 5.11). This localized change in basal melting, ocean mixing and advection creates a more stratified water column with warm ocean temperatures in the lower 100 m that are near the values of T_{init} and cooler tempera-

tures in the surface 100 m that are close to the in-situ freezing point. This changes opens up the S. Channel as a conduit for warmer water to gain access to the Western Ronne ice stream inlets, with the consequence of nearly doubling the regionally-averaged melt rates around the downstream grounding lines of the Institute and Rutford glacier tributaries. Möller Ice Stream is similarly affected. The only region showing little change in basal melting between standard and modified cases is the Foundation inlet region.

Regional changes in basal melting in response to changes in cavity geometry are shown to have a variable impact ice shelf mass balance along flow lines. Evans Ice Stream and west Foundation ice stream flow line mass balances are the least affected by the change in topography. Other tributaries show variable changes. Some ice flow lines in the Möller and western Foundation Ice Streams show that a change in topography further enhances the loss of mass due to temperature increase while other flow lines show that the change in topography buffers then change in mass along flow lines. The FIS is the only region where a change in cavity shape buffers the ice shelf from mass loss due to ocean warming along all flow lines, suggesting that the ice sheet flowing into FIS may be more insulated from the effect of ocean warming than the ice sheet flowing into the RIS.

Wright et al. (in review) used an ice sheet model to demonstrate that grounding line mass loss has a variable affect on ice sheet dynamics owing to regional differences in bed topography. Their results indicate that the Institute and Möller ice streams are most sensitive to grounding line basal mass loss. Our results suggest that these grounding lines are susceptible to enhanced basal melting not only from warming ocean conditions but also from the change in ocean circulation that may result as a consequence of enhanced melting

from this increase in ocean heat.

The Rutford Ice Stream is of particular importance to predicting ocean-ice-sheet interactions because it is the Weddell Sea end member of the Amundsen-Weddell through-flow passage that connects the Weddell Sea to the Amundsen Sea via the bedrock topography channel connecting Rutford Ice Stream and Pine Island Glacier Ice Stream (*Vaughan et al.*, 2011). Our results suggest that tide-topography interactions may enhance basal melting at the grounding line of the Rutford Ice Stream with a plausible consequence of accelerating the process of un-freezing the through flow between the Amundsen and Weddell Seas.

Accurate and repeated mapping of ice shelf topography as well as the inclusion of tidal forcing in numerical models is necessary for producing accurate predictions of how ocean and ice shelf interactions influence on ice-sheet dynamics.

Table 5.1: Symbols definitions used throughout this chapter.

Definition	Symbol	Units	Value
Ice draft below mean sea level	z_{ice}	m	< 0
Sea floor depth	h	m	> 0
Water column thickness	wct	m	> 0
Potential temperature of ocean	T_o	$^{\circ}\text{C}$	
Initial potential temperature	T_{init}	$^{\circ}\text{C}$	-1.4 or -1.9
Initial salinity	S_{init}		34.65
Meltwater equivalent for basal melt rate	w_b	m s^{-1}	
Change in ice mass	M_b	Gt a^{-1}	
Transect heat flux	Q_T^{trans}	kW/m^2	
Ocean density	ρ_o	kg m^{-3}	
Specific heat capacity (ocean)	c_{po}	$\text{J kg}^{-1} \text{C}^{-1}$	3985
Velocity perpendicular to transect	u_{\perp}	m s^{-1}	
Transect area	A	m^2	
Time averaged barotropic tidal current	U_{tide}	m s^{-1}	

Table 5.2: An overview of the five model runs presented in this paper and the name that is used to reference them throughout this paper.

case name	cavity geometry	T_{init}
standard	standard	-1.9°C
standard warm	standard	-1.4°C
modified warm	modified	-1.4°C
standard tides-only	standard	-1.9°C
modified tides-only	modified	-1.4°C

Table 5.3: Regional characteristics of heat flux balance for the standard case with $T_{init} = -1.9^{\circ}\text{C}$, showing: the convergence or divergence of heat [tW] across the transects shown in Figure 5.12, the net surface heat flux in the region, averaged over one year [tW], and the combined effect of these heat exchanges.

region	convergence	divergence	surface	net
Filchner		-0.16	0.4	0.24
Foundation-Möller	0.41		0.19	0.6
S. Channel		-1.51	0.23	-1.28
FRIS		-0.62	0.77	0.15

Table 5.4: Same as Table 5.3 but for the standard case with $T_{init} = -1.4^{\circ}\text{C}$.

region	convergence	divergence	surface	net
Filchner		-0.61	0.86	0.25
Foundation-Möller	1.05		0.49	1.54
S. Channel		-1.92	0.43	-1.49
FRIS		-2.34	2.33	-0.01

Table 5.5: Same as Tables 5.3 and 5.4 but for the modified case with $T_{init} = -1.4^{\circ}\text{C}$.

region	convergence	divergence	surface	net
Filchner		-0.21	0.79	0.58
Foundation-Möller	0.87		0.54	1.41
S. Channel		-1.73	0.15	-1.58
FRIS		-1.72	2.10	0.38

Table 5.6: Overview of changes (%) in transect dimensions and predicted values between the standard -1.4°C and the modified -1.4°C case. Values shown in brackets “[]” reflect change between the standard -1.9°C and standard -1.4°C cases. The negative value for *FIS* reflect a change in velocity direction between warm and cold cases while the negative value for *Henry to Berkner* reflects a change in both velocity and heat flux direction. In general, a negative value indicates a change to a lesser or more negative magnitude.

transect name	area	area-normalized heat flux	average velocity
<i>FIS</i>	10%	0.6% [-1%]	-90% [-183%]
<i>S. Berkner</i>	5%	-32% [17%]	9% [67%]
<i>Henry to Berkner</i>	16%	-103% [-1245%]	191% [-343%]
<i>E. BIR</i>	37%	-73% [-6%]	-70% [34%]
<i>W. BIR</i>	15%	-41% [11%]	-34% [35%]
<i>RIS</i>	2.7%	10% [-55%]	6% [123%]

Table 5.7: Publication sources and abbreviations used in Figure 5.23. Method of calculating melt rates is summarized as Ocean Model (OM), Standard Glaciological Method (GM), Ocean Observation (OO), Geophysical Tracer (GT), following Table S2 in *Rignot et al.* (2013) supplementary document. The time period of observation(s) or forcing files are listed together with source of data or model output. Publication abbreviations with “*”

pub. abbr.	method	reference	time period	source
TS	OM	this study	NA	
Mrev*	GM	<i>Moholdt et al.</i> (in review)	2003-2009	
R13*	GM	<i>Rignot et al.</i> (2013)	2003-2009 2007-2008 1979-2010	ICESat ALOS PALSAR InSAR RACMO2 Operation IceBridge BEDMAP
D13	GM	<i>Depoorter et al.</i> (2013)	2003-2009 1994-2002 2007-2009 2007-2009 1979-2010	ICESat ERS-1 ERS-2 InSAR RACMO2
T12	OM	<i>Timmermann et al.</i> (2012)	1958-2010 2001	NCEP winds T_{init} , S_{init}
M11	OM	<i>Makinson et al.</i> (2011)	NA	
H04	OM	<i>Hellmer</i> (2004)	1978-1997	NCEP 10-m winds, 2-m air temperature, specific humidity, cloudiness, and net precipitation
JP03	GM	<i>Joughin and Padman</i> (2003)	1997	RADARSAT InSAR
N03	OO	<i>Nicholls et al.</i> (2003)	1995-1999	CTD
F01*	OO	<i>Foldvik et al.</i> (2001)	1992-1993	CTD & mooring
G99*	OM	<i>Gerdes et al.</i> (1999)	NA	
G94	GT	<i>Gammelsrød et al.</i> (1994)	Feb. 1993	CFC-11, CFC-12, O ₂ , Si
J92	GM	<i>Jacobs et al.</i> (1992)		
JD91	GM	<i>Jenkins</i> (1991)	1985-1988	Radar echo sounding
S90	GT	<i>Schlosser et al.</i> (1990)	Jan-Mar. 1985	$\delta^{18}O$, He

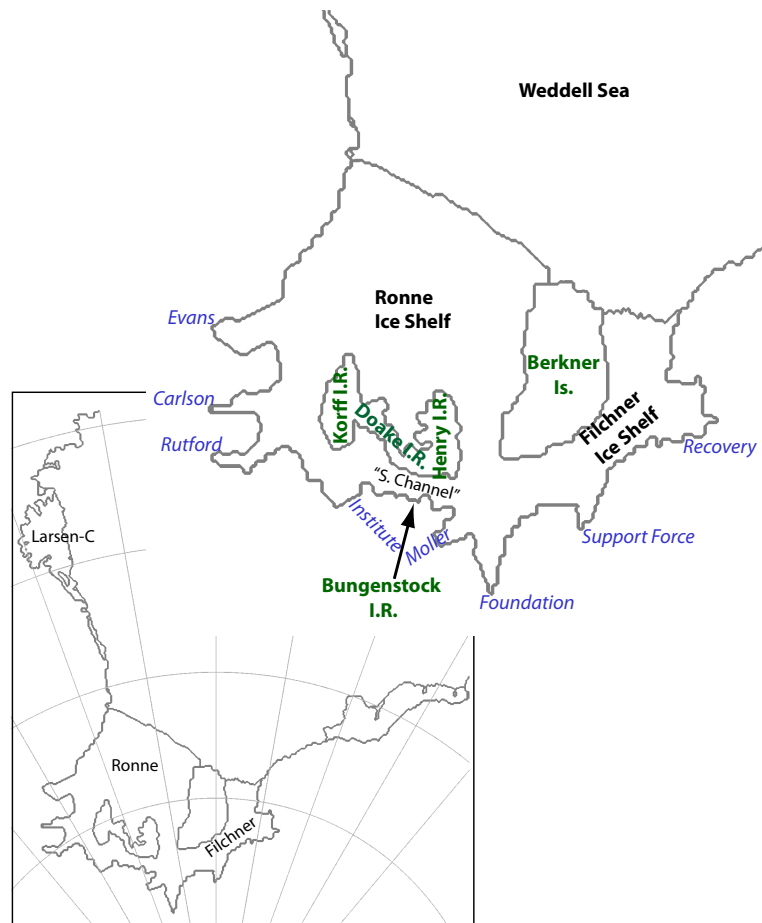


Figure 5.1: Model domain (lower left) and insert showing important geographic references for FRIS (upper right). Black labels are used for names of ice shelves and ocean. Green labels are used for names of geographic features. Blue labels are used for the names of the Ice Stream, located at the grounding lines of the glacier inlets.

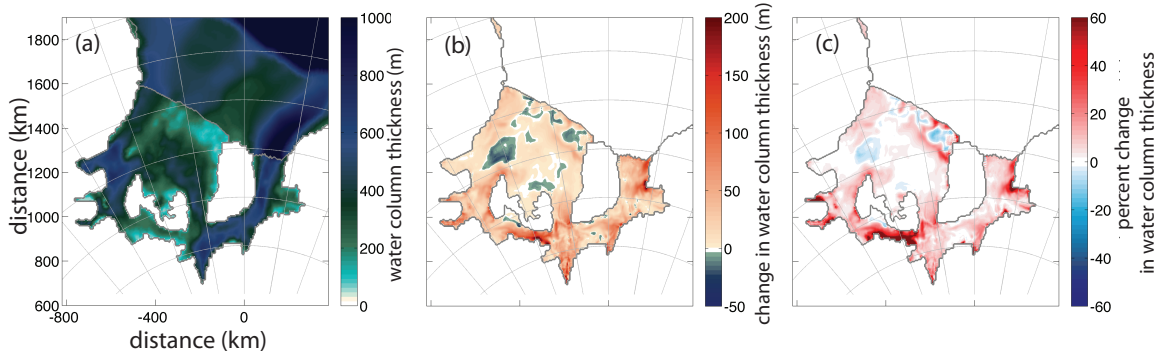


Figure 5.2: An overview of the grid geometry adjustments between the standard and modified grids. (a) $wct (h + z_{ice})$ used for the standard geometry. (b) Difference in wct between the standard- and modified-geometries (modified - standard), where positive indicates that a larger wct in the modified geometry. (c) Percent change in wct (modified - standard)/(standard), where positive values indicate a larger wct in the modified geometry,

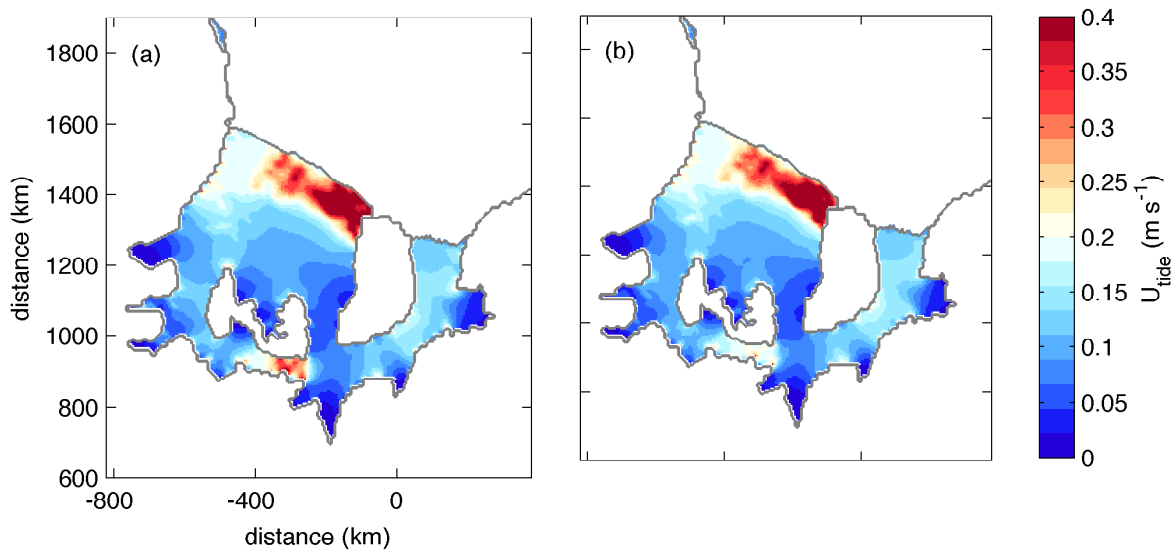


Figure 5.3: Barotropic current beneath FRIS, as calculated by Equation 5.1, for (a) the standard-grid, tides-only run, time averaged over 35 days; and (b) the modified-grid.

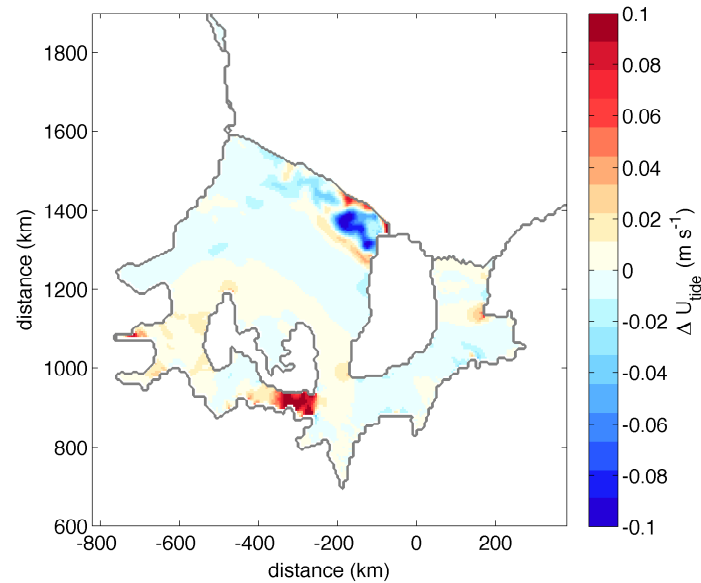


Figure 5.4: Difference in barotropic currents, $\Delta U_{tide} = U_{tide}^s - U_{tide}^m$, where U_{tide}^s is the standard case current shown in Figure 5.3a and U_{tide}^m is the modified case current shown in Figure 5.3b. Positive (red) values show where the modified geometry has weaker currents than the standard geometry, while negative (blue) values indicate regions where the modified geometry has a stronger currents.

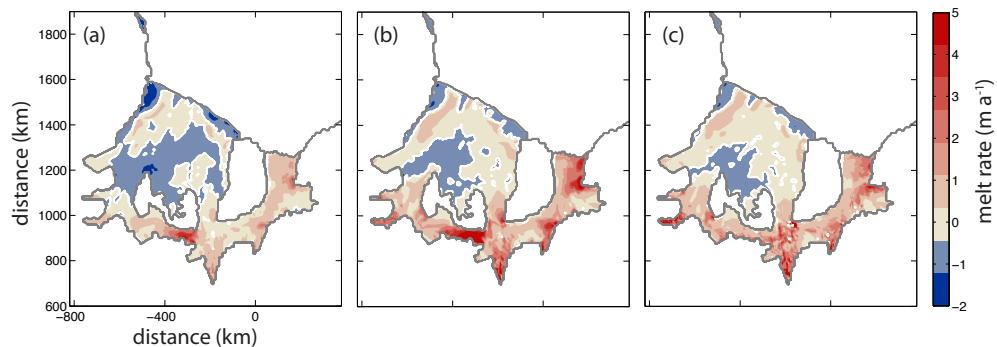


Figure 5.5: Meltrates for the standard cold, standard warm and modified warm cases. (a) Meltrates averaged over the last year of the standard cold case, with $T_{init} = -1.9^\circ\text{C}$. The white contour lines mark the transition between regions of accretion (blue) and ablation (red). (b) Meltrates averaged over the last year of the standard warm case, with $T_{init} = -1.4^\circ\text{C}$. (c) Meltrates averaged over the last year of the modified warm case, with $T_{init} = -1.4^\circ\text{C}$.

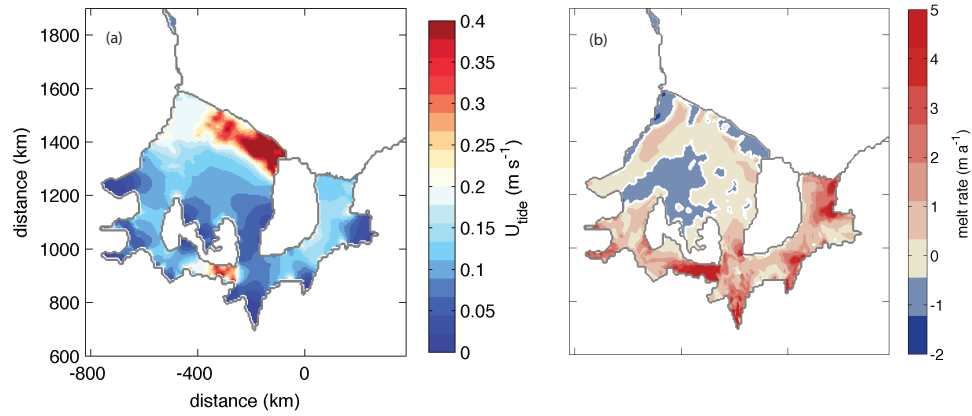


Figure 5.6: Comparison between tidal current and melt rates for the standard case. (a) U_{tide} for the standard case, as in Figure 5.3a. (b) Melt rate for the standard warm case, as in Figure 5.5b.

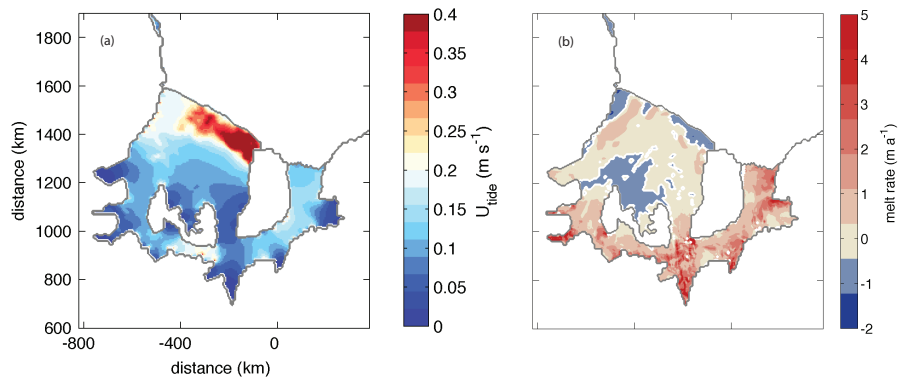


Figure 5.7: Comparison between tidal current and melt rates for the modified case. (a) U_{tide} for the modified case, as in Figure 5.3b. (b) Melt rate for the modified warm case, as in Figure 5.5c.

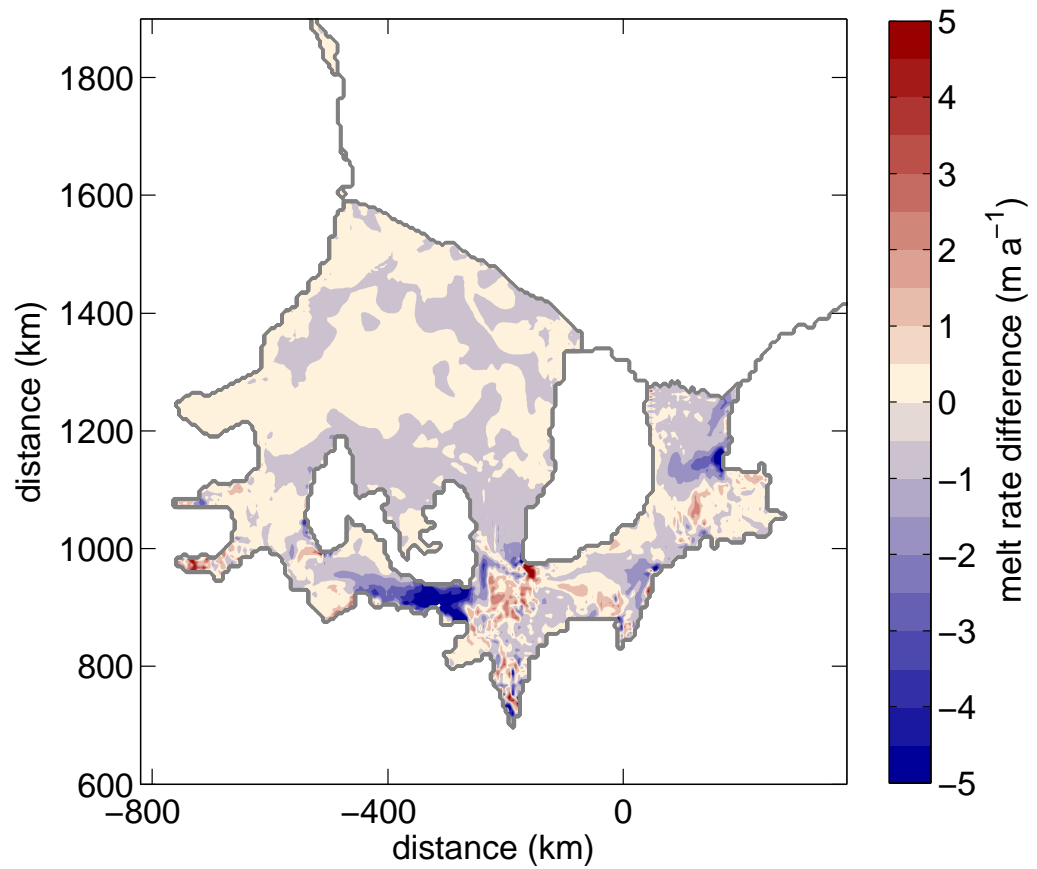


Figure 5.8: Difference between year averaged melt rates of modified warm case (Figure 5.5(c)) and standard warm case(Figure 5.5(b)). Negative values (blue) indicate that the modified warm case has less melt than the standard warm case.

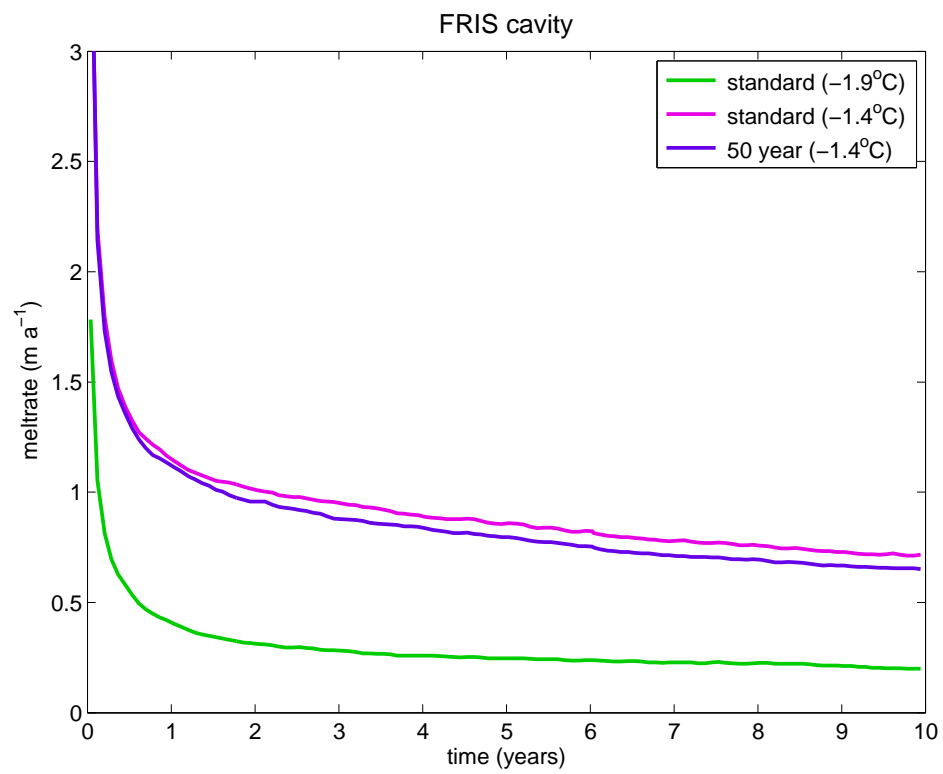


Figure 5.9: FRIS-averaged melt rates over model runtime, with values averaged over 30-day intervals.

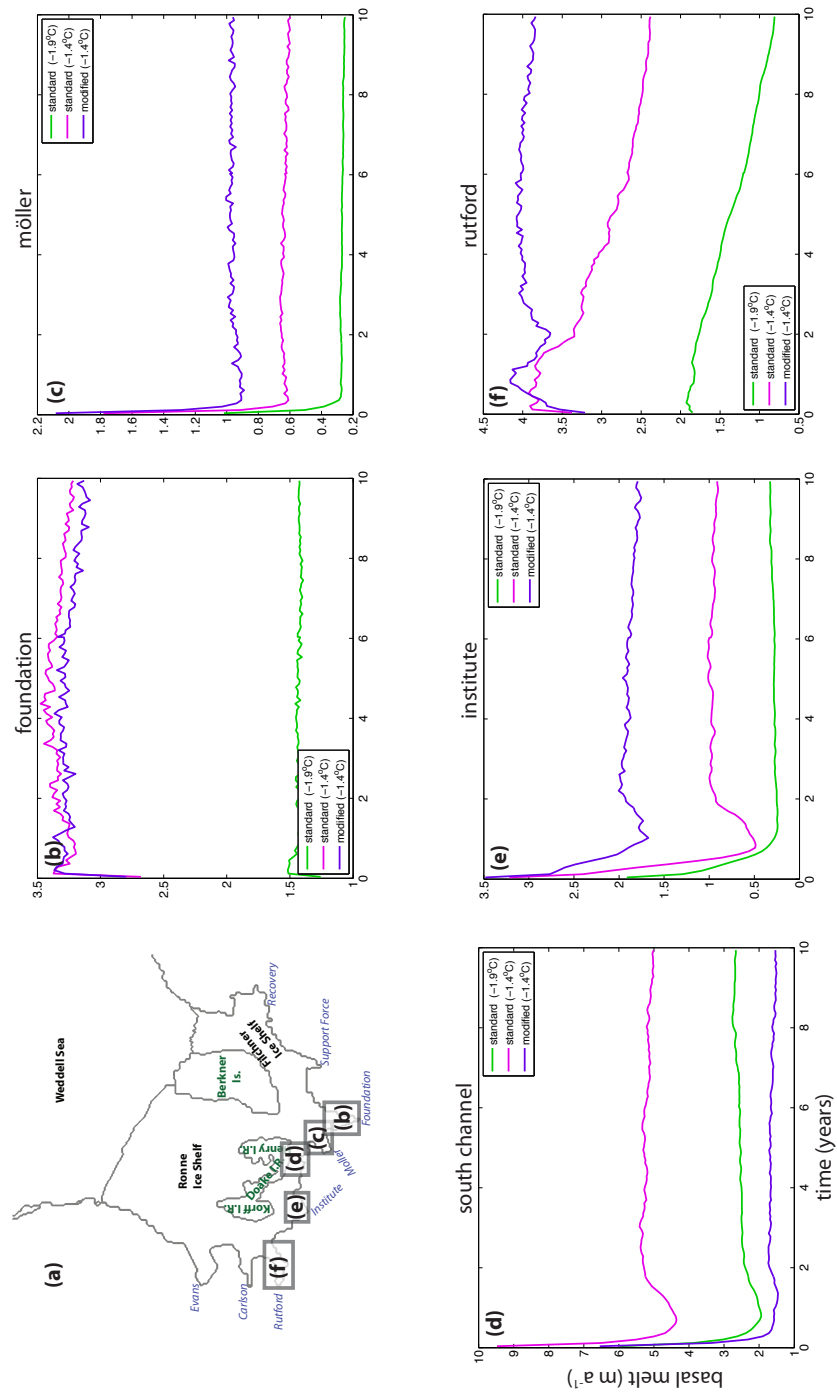


Figure 5.10: Regionally averaged values of melt rates over time with (a) showing the locations of the regionally averaged values of melt rate for: (b) Foundation inlet, (c) Möller inlet, (d) S. Channel, (e) Institute inlet, and (f) Rutford embayment.

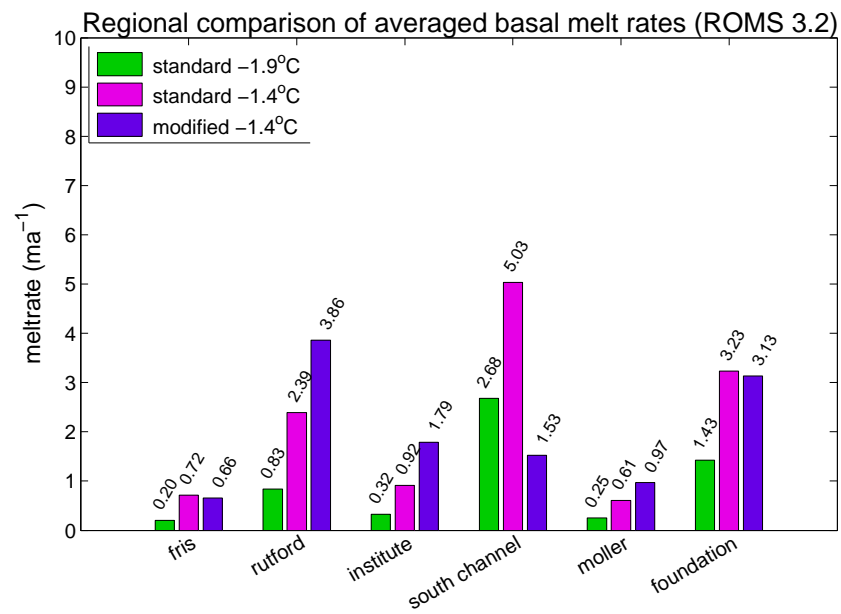


Figure 5.11: Steady state regionally averaged values, as shown in Figure 5.10, averaged over the last year.

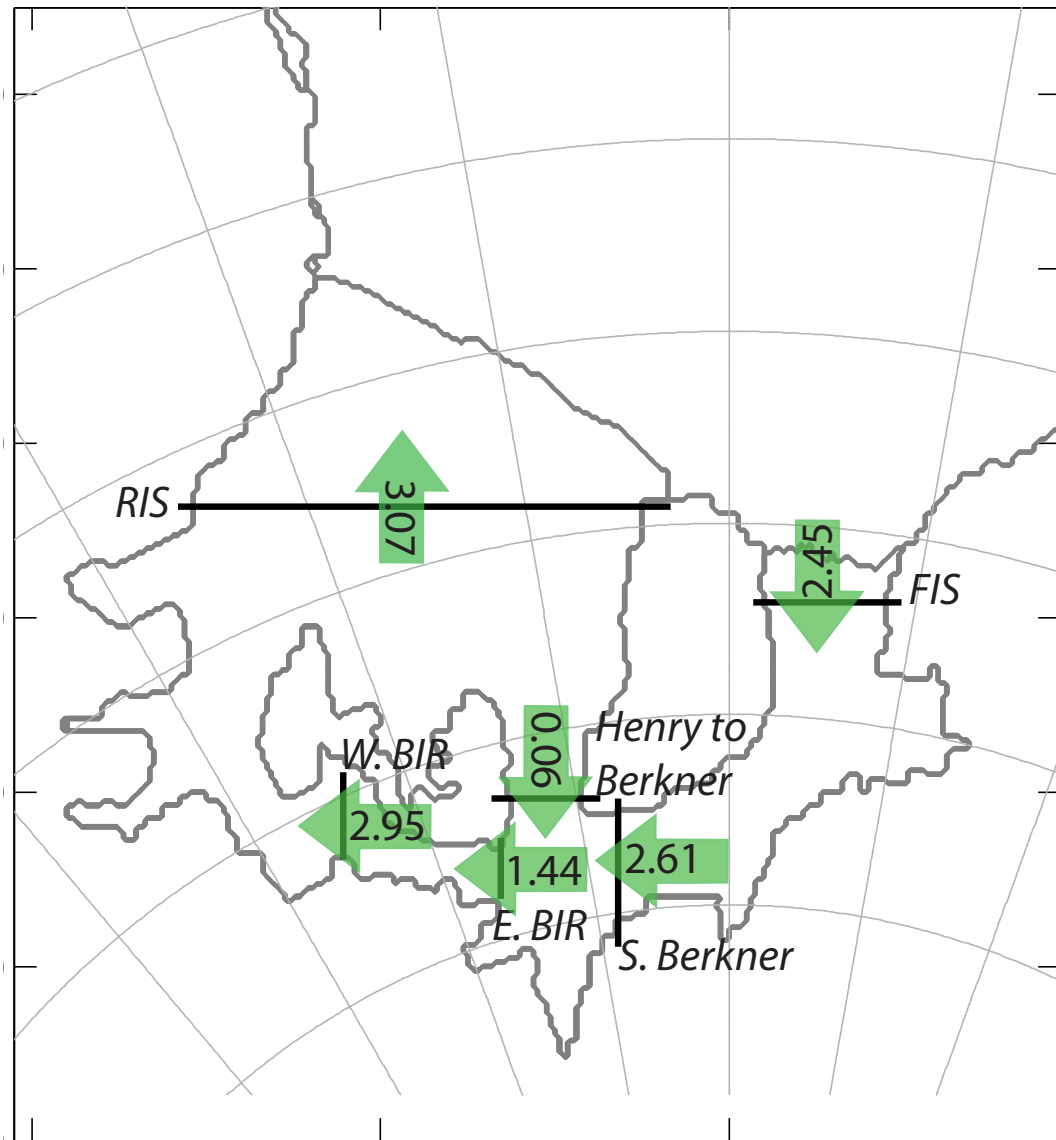


Figure 5.12: Map of heat flux magnitudes across transect locations shown as solid black lines. Transects are labeled according to location: across FIS (*FIS*), the channel south of Berkner Is. (*S. Berkner*), the channel between Henry I.R. and Berkner Is. (*Henry to Berkner*), the channel between East Bungenstock I.R. and Henry I.R. (*E. BIR*), the channel between West Bungenstock I.R. and Doake Ice Rumpel (*W. BIR*), and across RIS (*RIS*). The corresponding magnitudes of heat fluxes across these transects are shown in units of teraWatts within the green arrows, which point in the direction of transport. Heat flux values shown here are for the standard case with $T_{init} = -1.9^{\circ}\text{C}$.

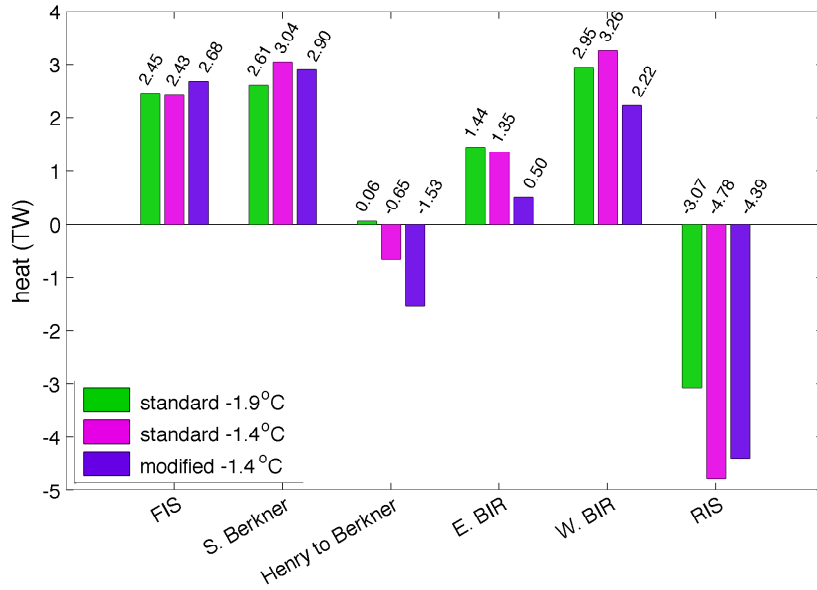


Figure 5.13: Heat flux across transects shown in Figure 5.12.

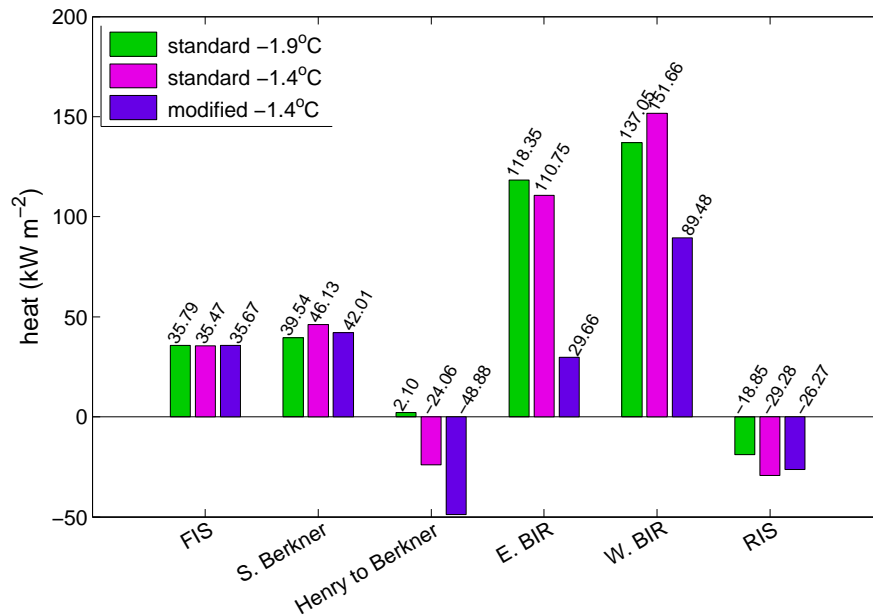


Figure 5.14: Heat flux normalized by transect area for transects shown in Figure 5.12. Percent change in transect area between modified and standard cases shown in Table 5.6.

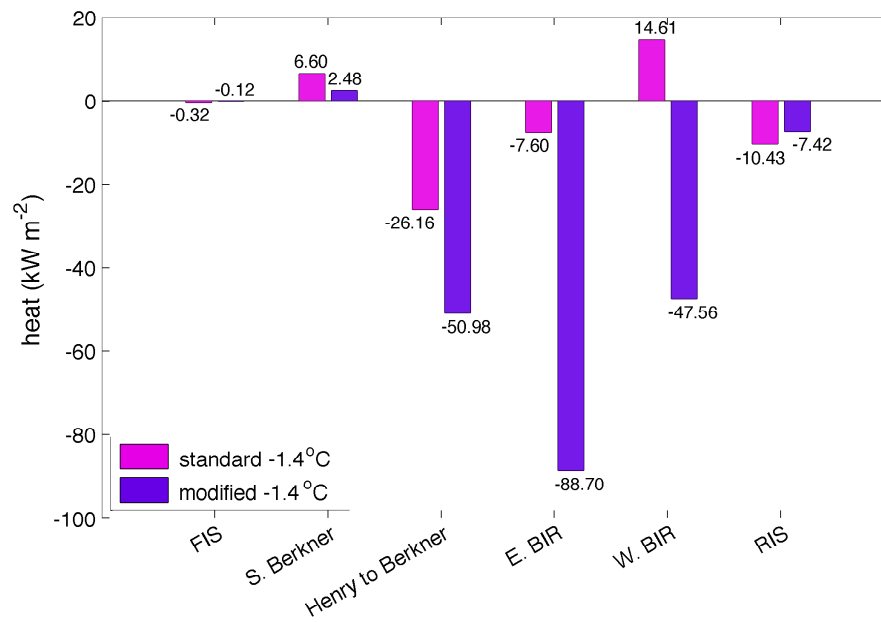


Figure 5.15: Difference in area-normalized heat fluxes between the two cases with $T_{init} = -1.4^{\circ}\text{C}$ and the $T_{init} = -1.9^{\circ}\text{C}$ standard case, as shown in Figure 5.15.

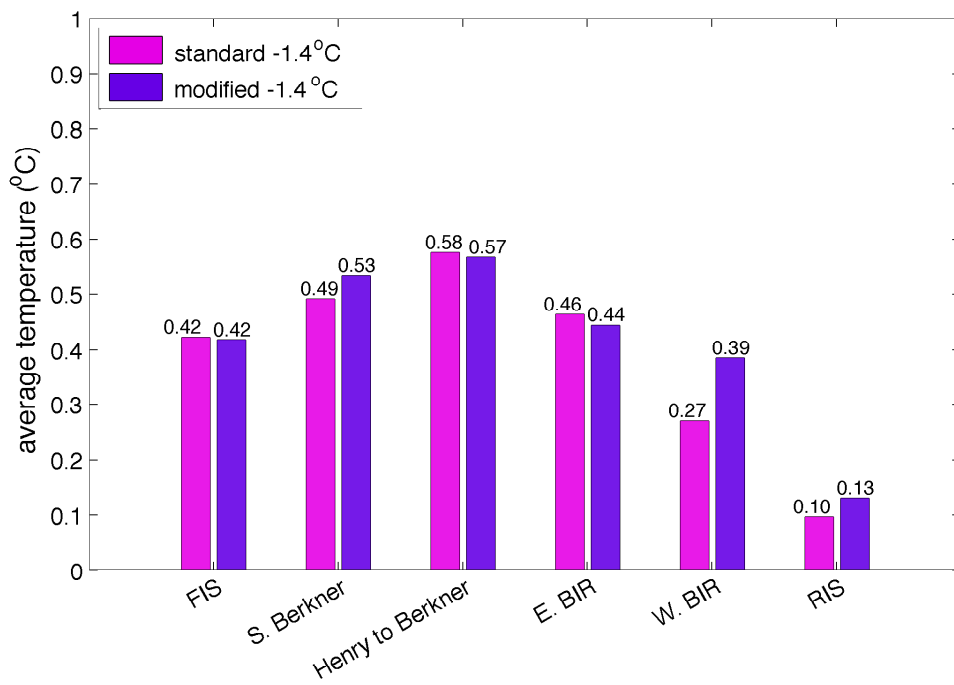


Figure 5.16: Deviations of average temperatures from standard -1.9°C case for transects shown in Figure 5.12.

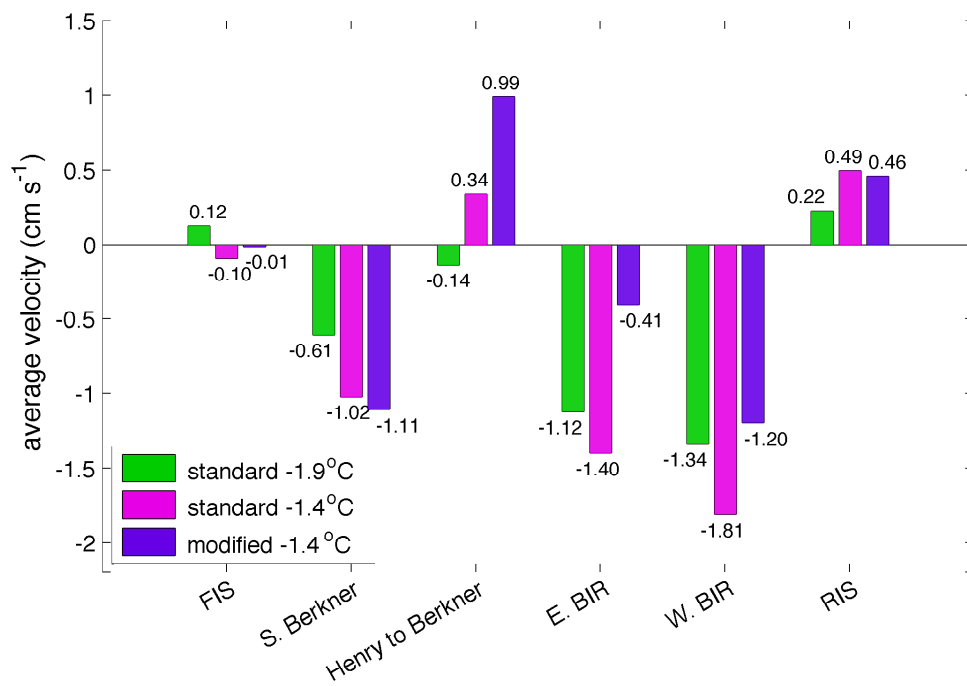


Figure 5.17: Average perpendicular velocities for transects shown in Figure 5.12.

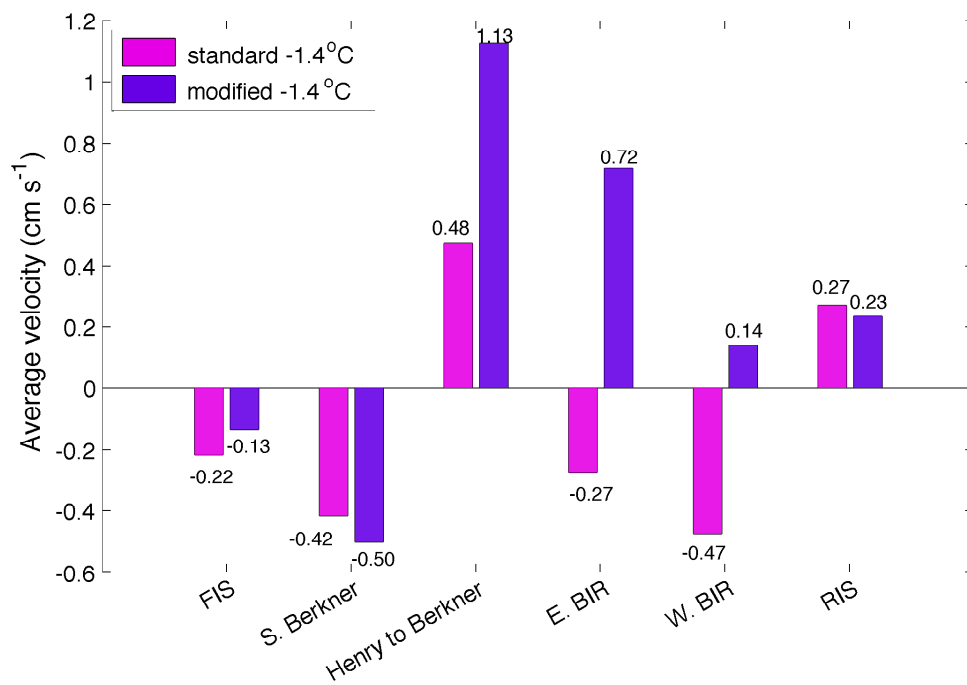


Figure 5.18: Deviations of average perpendicular velocity (Figure 5.17) from standard -1.9°C case for transects shown in Figure 5.12.

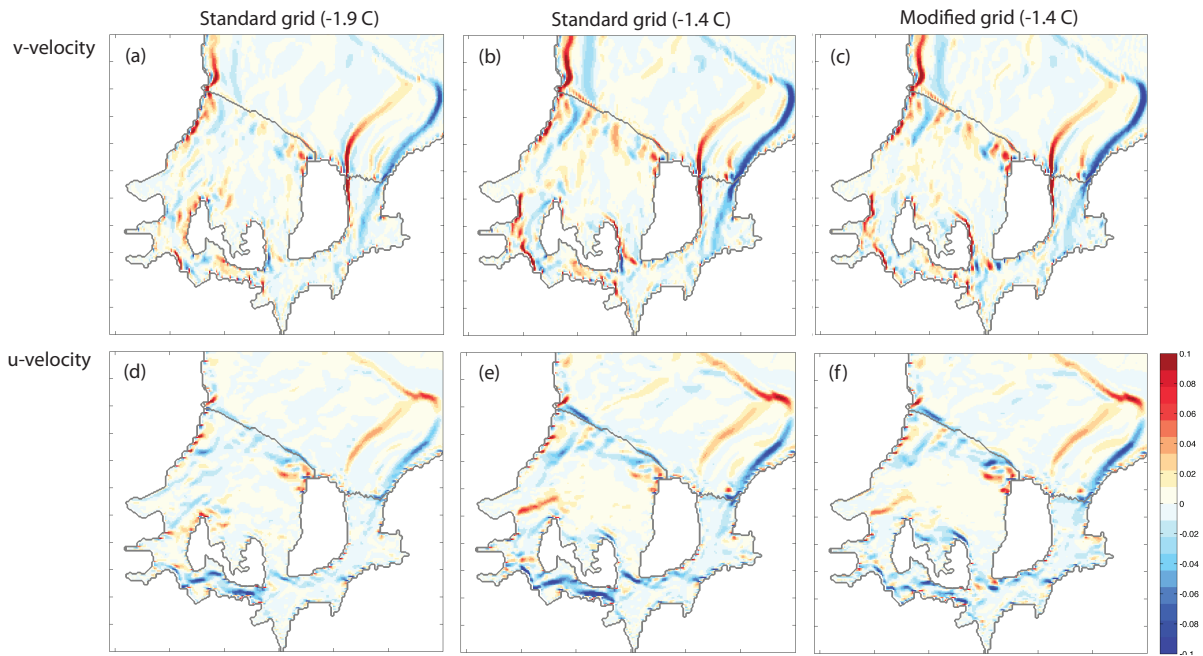


Figure 5.19: Barotropic velocities (m s⁻¹) averaged over the last 12-months of model run time. Upper panels show v-velocities for (a) standard geometry with $T_{init} = -1.9^{\circ}\text{C}$, (b) standard geometry with $T_{init} = -1.4^{\circ}\text{C}$, and (c) modified geometry with $T_{init} = -1.4^{\circ}\text{C}$. Bottom panels show u-velocity for the same progressions of runs in (d), (e), and (f).

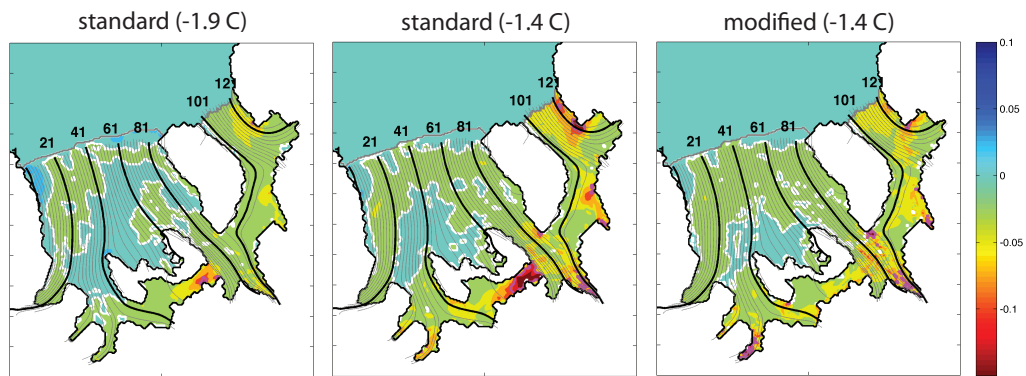


Figure 5.20: Map of basal ice mass loss or gain (Gt a⁻¹) with white contours showing transition from loss (green to red) and gain (blue). Black lines indicate ice shelf flow lines, calculated from particle tracking by Dr. Geir Moholdt (May 31, 2013). Numbers along ice shelf front correspond to flow line numbers used in Figure 5.21 and 5.22.

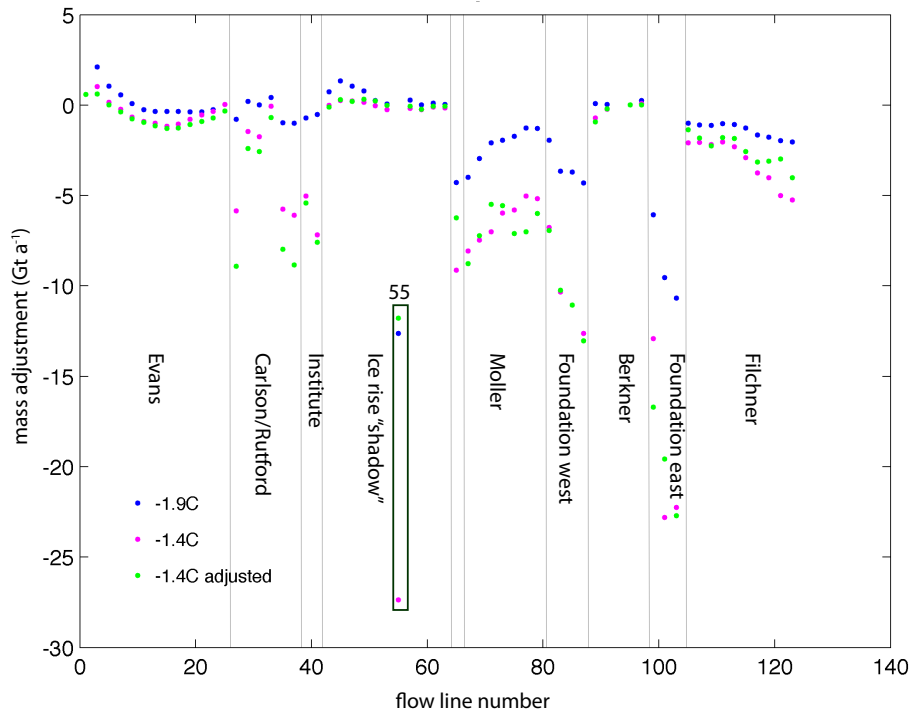


Figure 5.21: Integrated mass loss or gain along the flow lines shown in Figure 5.20. Blue points represent standard case, magenta represents standard warm case and green represents modified warm case. Vertical black lines are used to differentiate regions based on the ice stream of origin. Foundation ice stream is split into an east and west component as some flow lines flow to the east of Berkner Is. and others to the west of Berkner Is. In between these two are shorter flow lines with origins in the northern regions (both east and west) of Berkner Is.

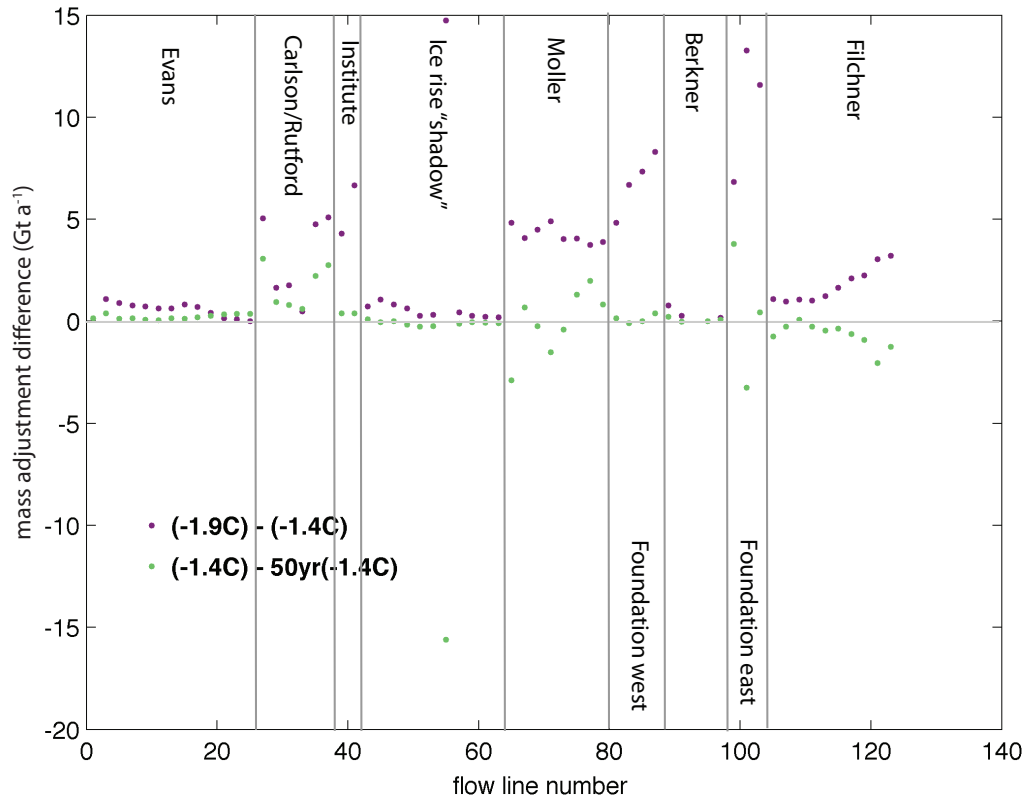


Figure 5.22: Difference in integrated mass loss or gain along the flow lines shown in Figure 5.20. Magenta points show the difference between the standard case with $T_{init} = -1.9^{\circ}\text{C}$ and $T_{init} = -1.4^{\circ}\text{C}$. Green points show the difference between the standard case with $T_{init} = -1.4^{\circ}\text{C}$ and the modified case with $T_{init} = -1.4^{\circ}\text{C}$. Vertical grey lines are used to differentiate regions based on the ice stream of origin. Foundation ice stream is split into an east and west component as some flow lines flow to the east of Berkner Is. and others to the west of Berkner Is. In between these two are shorter flow lines with origins in the northern regions (both east and west) of Berkner Is.

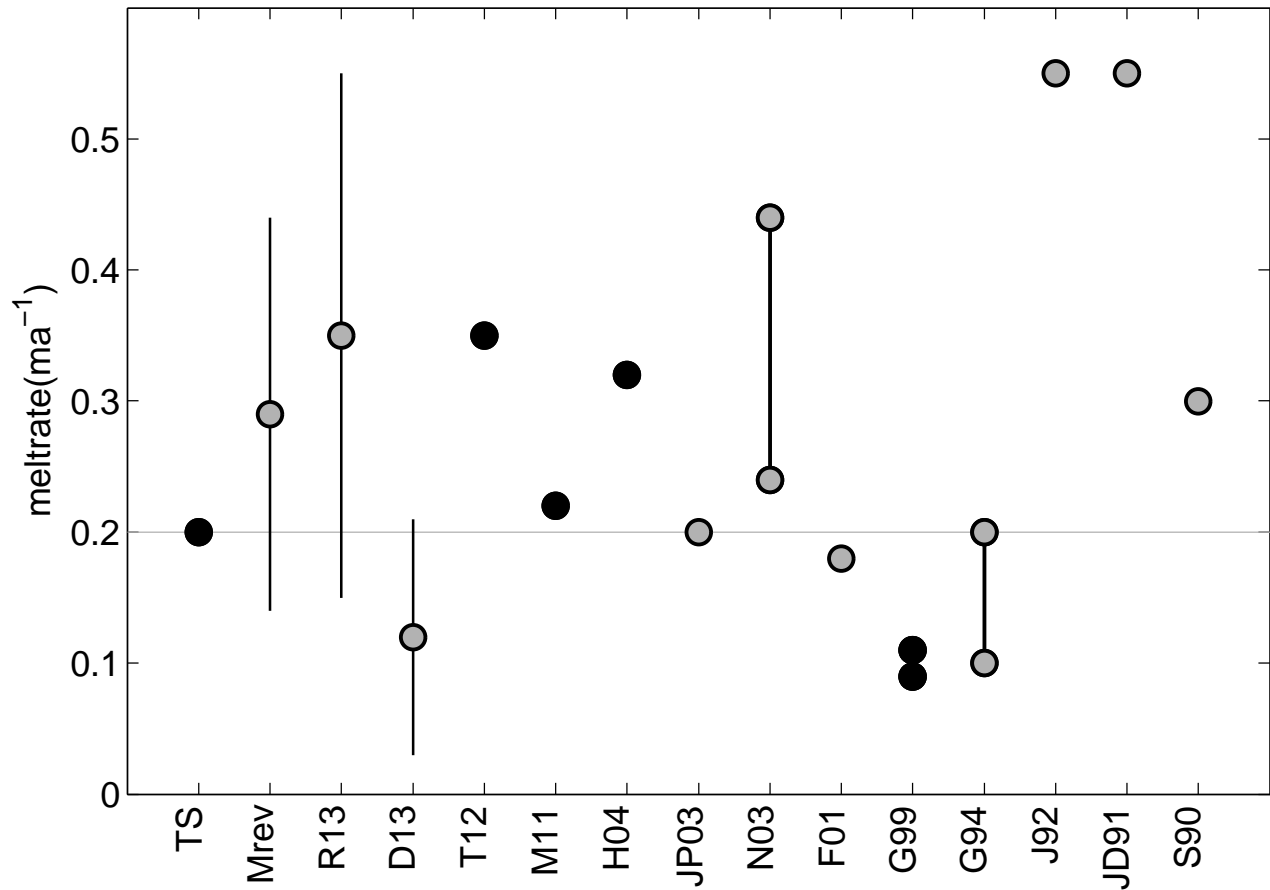


Figure 5.23: a

nd others.]FRIS-averaged basal melt rate comparison between this study [TS] and others. Model results are shown as black dots while observations are shown as grey dots. Error bars for remote sensing observations are shown as black lines for Mrev (*Moholdt et al.*, in review), R13 (*Rignot et al.*, 2013) and D13 (*Depoorter et al.*, 2013). Min and max values are connected by thick, solid, black lines to show the range of values reported by N03 (*Nicholls et al.*, 2003) and G94 (*Gammelsrød et al.*, 1994). A summary of the studies presented here and their abbreviations is provided in Table 5.7.

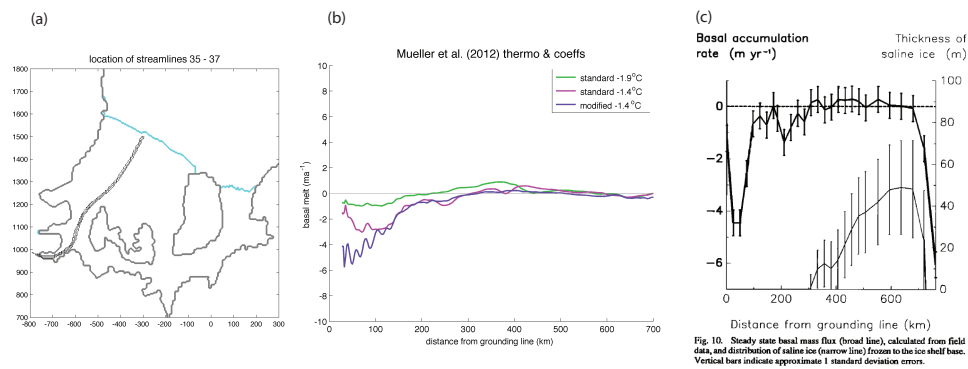


Figure 5.24: Comparison of estimated basal melt to observations from the western RIS. (a) Location of streamlines along which basal melt is averaged. (b) Basal melt along streamline for the standard case, the standard warm case and the modified warm case. (c) Figure 10 from *Jenkins* (1991) showing basal melt estimates derived from radar observations.

Chapter 6

General Conclusions

The purpose of this dissertation was to explore how uncertainties in sub-ice-shelf topography influence predictions of basal melting in the Larsen-C and Filchner-Ronne ice shelves of the Weddell Sea, Antarctica. Uncertainties in sub-ice-shelf topography include both the uncertainty of the sub-ice-shelf bathymetry as well as the uncertainty in ice draft estimates. The combined uncertainty can lead to errors in estimates of water column thickness on the order of 100 m, although sometimes much more. This difference can have a significant impact on tidal currents and, hence, basal melting. This dissertation explores the uncertainty of this error both in modern day estimates and in future conditions where ice draft topography changes in response to increased ocean warming.

This dissertation is divided into four main sections. Chapter 2 explores the underlying thermodynamic assumptions and the range of basal melt estimates that result from various choices in thermodynamic parameters. Chapter 3 describes the methodology used in creating the ice draft and bathymetry grids used in the modeling study of Larsen-C Ice

Shelf. Chapter 4 reports on basal melt estimates for the Larsen-C Ice Shelf using the model geometry described in Chapter 3. Chapter 5 shows how future changes in ocean temperatures can affect basal melting of the Filchner-Ronne ice shelf due to a feedback between changes in sub-ice-shelf topography and tidal currents.

The main conclusions of this dissertation include:

1. The sensitivity of w_b and tide-induced mean circulation to the energetics of Diurnal Topographic Vorticity Waves implies that high-resolution grids of ice draft and seabed bathymetry will be required to minimize uncertainties in w_b . A conservative estimate of required grid resolution is the ability to resolve the baroclinic Rossby radius of deformation, ~ 5 km in high latitude seas, implying a model grid spacing of $\delta x \sim 1$ km.
2. The accuracy of w_b predictions is undermined by potential errors in sub ice shelf geometry and ocean hydrography such that there is an urgent need for new data sets to adequately constrain models of ice shelf and ocean interactions.
3. Changes in ocean temperature and ice shelf topography have a significant affect on basal melting of FRIS.
4. The overall tide-topography feedback from ice shelf basal melting reduces the average melt rate of FRIS.
5. Regional variations in the tide-topography feedback are significant. In some regions of FRIS, this feedback leads to an increase in basal melting of $\sim 100\%$ while in other regions the feedback reduces basal melting by $\sim 70\%$.

6. Topographic changes in the S. Channel of FRIS (imposed by an increased of basal melting in response to warmer ocean waters) changes tidal currents and stratification in such a way as to significantly affect down stream grounding line melt. This “bottleneck” characteristic of the S. Channel indicates that changes in ice shelf cavity geometry can have both local and non-local affect on basal melting.
7. Global models aimed at providing estimates of future sea level rise using coupled ice-sheet/ocean/atmosphere models will need to include tides in the sub-ice-shelf cavity in order to render accurate predictions.

The accuracy of topographic datasets ought to be considered when interpreting results from numerical studies of ice shelf basal melting. It is likely that basal melting predictions will continue to be undermined not only by errors in topography (and, hence, tidal currents) but also by uncertainties in thermal exchange and drag coefficients. Field studies aimed at providing maps of these parameters as well as water column thickness will continue to be imperative to our collective ability to provide meaningful model results. Advances in grid resolution (or adaptive grid methods) in addition to the inclusion of tides in ocean/ice-sheets modeling will also be important for reducing uncertainties in the future evolution of the Antarctic Ice Sheet.

Bibliography

Alley, R. B., H. J. Horgan, I. Joughin, K. M. Cuffey, T. K. Dupont, B. R. Parizek, S. Anandakrishnan, and J. Bassis (2008), A simple law for ice-shelf calving, *Science*, *322*, 1344–1344, doi:10.1126/science.1162543.

Årthun, M., K. W. Nicholls, K. Makinson, M. A. Fedak, and L. Boehme (2012), Seasonal inflow of warm water onto the southern Weddell Sea continental shelf, Antarctica, *Geophys. Res. Lett.*, *39*, L17601, doi:10.1029/2012GL052856.

Bamber, J., and R. Bindshadler (1997), An improved elevation dataset for climate and ice-sheet modelling: validation with satellite imagery, *Ann. Glaciol.*, *25*, 438–444.

Bathmann, U., V. Smetacek, H. de Baar, E. Fahrbach, and G. Krause (1994), The expeditions ANTARKTIS X/6-8 of the research vessel “POLARSTERN” in 1992/1993., *Tech. rep.*, Alfred-Wegener-Institute for Polar and Marine Research.

Beckmann, A., and D. B. Haidvogel (1993), Numerical simulation of flow around a tall isolated seamount. Part 1: Problem formulation and model accuracy, *J. Phys. Oceanogr.*, *23*, 1736–1753.

Beckmann, A., H. H. Hellmer, and R. Timmermann (1999), A numerical model of the

- Weddell Sea: Large-scale circulation and water mass distribution, *J. Geophys. Res.-Ocean.*, *104*(C10), 23,375–23,391.
- Bindschadler, R., D. G. Vaughan, and P. Vornberger (2011), Variability of basal melt beneath the Pine Island Glacier Ice Shelf, West Antarctica, *J. Glaciol.*, *57*(204), 581–595.
- Cartwright, D. E. (1969), Extraordinary tidal currents near St. Kilda, *Nature*, *223*, 928–930.
- Chapman, D. (1985), Numerical treatment of cross-shelf open boundaries in a barotropic coastal ocean model, *J. Phys. Oceanogr.*, *19*, 384–391.
- Chelton, D. B., and D. Enfield (1986), Ocean signals in tide gauge records, *J. Geophys. Res.*, *91*(B9), 9081–9098.
- Cochran, J., and R. Bell (2012), Inversion of IceBridge gravity data for continental shelf bathymetry beneath the Larsen Ice Shelf, Antarctica, *J. Glaciol.*, *58*(209), 540–552, doi:10.3189/2012JoG11J033.
- Comiso, J. (2000), Variability and trends in Antarctic surface temperatures from in situ and satellite infrared measurements, *J. Climate.*, *13*, 1674–1696.
- Cook, A. J., and D. G. Vaughan (2010), Overview of areal changes of the ice shelves on the Antarctic Peninsula over the past 50 years, *The Cryosphere*, *4*, 77–98.
- Craven, M., I. Allison, H. Fricker, and R. Warner (2009), Properties of a marine ice layer under the Amery Ice Shelf, East Antarctica, *J. Glaciol.*, *55*(192), 717–728.
- De Angelis, H., and P. Skvarca (2003), Glacier surge after ice shelf collapse, *Science*, *299*, 1560–1562.

- Depoorter, M., J. Bamber, J. Griggs, J. Lenaerts, S. Ligtenberg, M. van den Broeke, and G. Moholdt (2013), Calving fluxes and basal melt rates of Antarctic ice shelves, *Nature*, *502*, 89–92, doi:doi:10.1038/nature12567.
- Dinniman, M., J. Klinck, and W. Smith (2011), A model study of Circumpolar Deep Water on the West Antarctic Peninsula and Ross Sea continental shelves, *Deep Sea Res. II*, *58*, 1508–1523, doi:10.1016/j.dsr2.2010.11.013.
- Dinniman, M. S., J. M. Klinck, and W. O. Smith Jr (2007), Influence of sea ice cover and icebergs on circulation and water mass formation in a numerical circulation model of the Ross Sea, Antarctica, *J. Geophys. Res.*, *112*, C11013, doi:10.1029/2006JC004036.
- Drewry, D., S. Jordan, and E. Jankowski (1982), Measured properties of the Antarctic Ice Sheet: Surface configurations, ice thickness, volume and bedrock characteristics, *Ann. Glaciol.*, *3*, 83–91.
- Egbert, G., and S. Erofeeva (2002), Efficient inverse modeling of barotropic ocean tides, *J. Atmos. Oceanic Technol.*, *19*(2), 183–204.
- Egbert, G., A. Bennett, and M. Foreman (1994), TOPEX/POSEIDON tides estimated using a global inverse model, *J. Geophys. Res.-Ocean.*, *99*(C12), 24,821–24,852.
- Fahrbach, E., G. Rohardt, and G. Krause (1992), The Antarctic Coastal Current in the southeastern Weddell Sea, *Polar Biology*, *12*, 171–182.
- Fahrbach, E., G. Rohardt, M. Schröder, and V. Strass (1994), Transport and structure of the Weddell Gyre, *Ann. Geophys.*, *12*, 840–855, doi:10.1007/s00585-994-0840-7.

- Fahrbach, E., M. Hoppema, G. Rohardt, M. Schröder, A. Wisotzki, and J.-O. Wolff (2004), Decadal-scale variations of water mass properties in the deep Weddell Sea, *Ocean Dynamics*, *54*(1), 77 – 91.
- Flather, R. (1976), A tidal model of the northwest European continental shelf, *Memoires de la Société Royale des Sciences de Liège*, *6*, 141–164.
- Foldvik, A., and T. Kvinge (1974), Conditional instability of sea water at the freezing point, *Deep Sea Res.*, *21*, 169–174.
- Foldvik, A., T. Gammelsrød, and T. Tørresen (1985), Circulation and water masses on the southern weddell sea shelf, *Antarctic Research Series*, *43*, 1–53.
- Foldvik, A., T. Gammelsrød, E. Nygaard, and S. Østerhus (2001), Current meter measurements near Ronne Ice Shelf, Weddell Sea: Implications for circulation and melting underneath the Filchner-Ronne ice shelves, *J. Geophys. Res.*, *106*(C3), 4463–4477.
- Fricker, H. A., and L. Padman (2002), Tides on Filchner-Ronne Ice Shelf from ERS radar altimetry, *Geophys. Res. Lett.*, *29*(12), doi:10.1029/2001GL014175.
- Fricker, H. A., and L. Padman (2012), Thirty years of elevation change on Antarctic Peninsula ice shelves from multi-mission satellite radar altimetry, *J. Geophys. Res.*, *117*, C02,026, doi:10.1029/2011JC007126.
- Fricker, H. A., R. Coleman, L. Padman, T. A. Scambos, J. Bohlander, and K. M. Brunt (2009), Mapping the grounding zone of the Amery Ice Shelf, East Antarctica using InSAR, MODIS and ICESat, *Antarct. Sci.*, *21*(5), 515–532, doi:10.1017/S095410200999023X.

- Gade, H. G. (1979), Melting of ice in sea water: A primitive model with application to the Antarctic Ice Shelf and icebergs, *J. Phys. Oceanogr.*, *9*(1), 189–198.
- Galton-Fenzi, B. K. (2009), Modelling ice-shelf/ocean interaction, Ph.D. dissertation in Quantitative Marine Science, Commonwealth Science and Industry Research Organisation and the University of Tasmania, Hobart, Australia.
- Galton-Fenzi, B. K., C. Maraldi, R. Coleman, and J. Hunter (2008), The cavity under the Amery Ice Shelf, East Antarctica, *J. Glaciol.*, *54*(188), 881–887.
- Gammelsrød, T., et al. (1994), Distribution of water masses on the continental shelf in the southern Weddell Sea, in *Polar oceans and their role in shaping the global environment*, edited by M. Johannessen, R. D. Muench, and J. E. Overland, pp. 159–175, American Geophysical Union, Washington, D. C.
- Gerdes, R., J. Determann, and K. Grosfeld (1999), Ocean circulation beneath Filchner-Ronne Ice Shelf from three-dimensional model results, *J. Geophys. Res.*, *104*(C7), 15,827–15,842.
- Gill, A. E., and E. H. Schumann (1974), The generation of long shelf waves by the wind, *J. Phys. Oceanogr.*, *4*(1), 83–90.
- Glasser, N., B. Kulesa, A. Luckman, D. Jansen, E. King, P. Sammonds, T. Scambos, and K. Jezek (2009), Surface structure and stability of the larsenc ice shelf, antarctic peninsula, *J. Glaciol.*, *55*(191), 400–410.
- Gordon, C. (2000), The simulation of SST, sea ice extents and ocean heat transports in a

- version of the hadley centre coupled model without flux adjustments., *Climate Dynamics*, *16*, 147–168.
- Gray, A., K. Matter, and G. Sofko (2000), Influence of ionospheric electron density fluctuations on satellite radar interferometry, *Geophys. Res. Lett.*, *27*, 1451–1454, doi:10.1029/2000GL000016.
- Greischar, L., and C. Bentley (1980), Isostatic equilibrium grounding line between the West Antarctic inland ice sheet and the Ross Ice Shelf, *Nature*, *283*, 641–654, doi:10.1038/283651a0.
- Griggs, J. A., and J. Bamber (2009), A new 1 km Digital Elevation Model of Antarctica derived from combined radar and laser data — Part 2: Validation and error estimates, *The Cryosphere*, *3*, 113–123.
- Grosfeld, K., R. Gerdes, and J. Determann (1997), Thermohaline circulation and interaction between ice shelf cavities and the adjacent open ocean, *J. Geophys. Res.*, *102*(C7), 15,595–15,610.
- Haidvogel, D. B., and A. Beckmann (1999), *Numerical Ocean Circulation Modeling, Series on Environmental Science and Management*, vol. 2, Imperial College Press, London.
- Hall, J. (2006), GEBCO Centennial Special Issue—Charting the secret world of the ocean floor: the GEBCO project 1903–2003, *Mar. Geophys. Res.*, *27*, 1–5, doi:10.1007/s11001-006-8181-4.
- Haney, R. L. (1991), On the pressure-gradient force over steep topography in sigma coordinate ocean models, *J. Phys. Oceanogr.*, *21*(4), 610–619.

- Hellmer, H. H. (2004), Impact of antarctic ice shelf basal melting on sea ice and deep ocean properties, *Geophys. Res. Lett.*, *31*(10), L10307, doi:0094-8276/04/2004GL019506.
- Hellmer, H. H., and D. J. Olbers (1989), A two-dimensional model for the thermohaline circulation under an ice shelf, *Antarct. Sci.*, *1*(4), 325–336.
- Hellmer, H. H., F. Kauker, R. Timmermann, J. Determann, and J. Rae (2012), Twenty-first-century warming of a large Antarctic ice-shelf cavity by a redirected coastal current, *Nature*, *485*, 225–228, doi:10.1038/nature11064.
- Heywood, K. J., R. A. Locarnini, R. D. Frew, P. F. Dennis, and B. A. King (1998), Transport and water masses of the Antarctic Slope Front system in the eastern Weddell Sea, in *Ocean, Ice, and Atmosphere: Interactions at the Antarctic Continental Margin*, *Antarctic Research Series*, vol. 75, pp. 203–214, American Geophysical Union.
- Holland, D. M., and A. Jenkins (1999), Modeling thermodynamic ice-ocean interactions at the base of an ice shelf, *J. Phys. Oceanogr.*, *29*(8), 1787–1800.
- Holland, P. R. (2008), A model of tidally dominated ocean processes near ice shelf grounding lines, *J. Geophys. Res.-Ocean.*, *113*, C11002, doi:10.1029/2007JC004576.
- Holland, P. R., and D. L. Feltham (2006), The effect of rotation and ice shelf topography on frazil-laden ice shelf water plumes, *J. Phys. Oceanogr.*, *36*(12), 2312–2327, doi:10.1175/JPO2970.1.
- Holland, P. R., D. L. Feltham, and A. Jenkins (2007), Ice Shelf Water plume flow beneath Filchner-Ronne Ice Shelf, Antarctica, *J. Geophys. Res.-Ocean.*, *112*(C7), C05044, doi:10.1029/2006JC003915.

- Holland, P. R., H. F. J. Corr, D. G. Vaughan, and A. Jenkins (2009), Marine ice in Larsen Ice Shelf, *Geophys. Res. Lett.*, *36*, L11604, doi:10.1029/2009GL038162.
- Holland, P. R., H. F. J. Corr, H. D. Pritchard, D. G. Vaughan, R. J. Arthern, A. Jenkins, and M. Tedesco (2011), The air content of Larsen Ice Shelf, *Geophys. Res. Lett.*, *38*, L10503, doi:10.1029/2011GL047245.
- Horgan, H. J., R. T. Walker, S. Anandakrishnan, and A. R. B. (2011), Surface elevation changes at the front of the Ross Ice Shelf: Implications for basal melting, *J. Geophys. Res.*, *116*, C02005, doi:10.1029/2010JC006192.
- Hunkins, K. (1986), Anomalous diurnal tidal currents on the Yarmak Plateau, *J. Mar. Res.*, *44*, 51–69.
- Jacobs, S. (2006), Observations of change in the Southern Ocean, *Philosophical Transactions of the Royal Society a-Mathematical Physical and Engineering Sciences*, *364*(1844), 1657–1681.
- Jacobs, S. S. (2004), Bottom water production and its links with the thermohaline circulation, *Antarctic Science*, *16*(4), 427–437, doi:10.1017/S095410200400224X.
- Jacobs, S. S., H. H. Helmer, C. S. M. Doake, A. Jenkins, and R. M. Frolich (1992), Melting of ice shelves and the mass balance of Antarctica, *J. Glaciol.*, *38*(130), 375–387.
- Jansen, D., B. Kulesa, P. Sammonds, A. Luckman, E. King, and N. Glasser (2010), Present stability of the Larsen C Ice Shelf, Antarctic Peninsula, *J. Glaciol.*, *56*(198), 593–600.

- Jarvis, E., and E. King (1993), The seismic wavefield recorded on an Antarctic ice shelf, *J. Seis. Explor.*, *2*, 69–86.
- Jenkins, A. (1991), A one-dimensional model of ice shelf-ocean interaction, *J. Geophys. Res.-Ocean.*, *96*(C11), 20,671–20,677.
- Jenkins, A. (2011), Convection-driven melting near the grounding lines of ice shelves and tidewater glaciers, *J. Phys. Oceanogr.*, *41*, 2279–2294, doi:10.1175/JPO-D-11-03.1.
- Jenkins, A., and A. Bombosch (1995), Modeling the effects of frazil ice crystals on the dynamics and thermodynamics of ice shelf water plumes, *J. Geophys. Res.*, *100*, 6967–6981.
- Jenkins, A., H. H. Hellmer, and D. M. Holland (2001), The role of meltwater advection in the formulation of conservative boundary conditions at an ice-ocean interface, *J. Phys. Oceanogr.*, *31*(1), 285–296.
- Jenkins, A., K. W. Nicholls, and H. F. J. Corr (2010), Observations and parameterization of ablation at the base of Ronne Ice Shelf, Antarctica, *J. Phys. Oceanogr.*, *40*, 2298–2312.
- Johnson, M. R., and A. M. Smith (1997), Seabed topography under the southern and western Ronne Ice Shelf, derived from seismic surveys, *Antarct. Sci.*, *9*(2), 201–208.
- Joughin, I. (2002), Ice-sheet velocity mapping: a combined interferometric and speckle-tracking approach, *Ann. Glaciol.*, *34*, 195–201.
- Joughin, I., and L. Padman (2003), Melting and freezing beneath Filchner-Ronne Ice Shelf, Antarctica, *Geophys. Res. Lett.*, *30*(9), 1477, doi:10.1029/2003GL016941.

- Joughin, I., B. E. Smith, I. M. Howat, T. Scambos, and T. Moon (2010), Greenland flow variability from ice-sheet-wide velocity mapping, *J. Glaciol.*, *56*(197), 415–430.
- Kader, B. A., and A. M. Yaglom (1972), Heat and mass-transfer laws for fully turbulent wall flows., *International Journal of Heat and Mass Transfer*, *15*(12), 2329–2351.
- Kader, B. A., and A. M. Yaglom (1977), Turbulent heat and mass-transfer from a wall with parallel roughness ridges., *International Journal of Heat and Mass Transfer*, *20*(4), 345–357.
- Khazendar, A., E. Rignot, and E. Larour (2011), Acceleration and spatial rheology of Larsen C Ice Shelf, Antarctic Peninsula, *Geophys. Res. Lett.*, *38*, L09502, doi:10.1029/2011GL046775.
- King, M. A., L. Padman, K. Nicholls, P. J. Clarke, G. H. Gudmundsson, B. Kulesa, and A. Shepherd (2011), Ocean tides in the Weddell Sea: new observations on the Filchner-Ronne and Larsen C ice shelves and model validation, *Geophys. Res. Lett.*, *116*, C06006, doi:10.1029/2011JC006949.
- King, M. A., L. Padman, K. Nicholls, P. J. Clarke, G. H. Gudmundsson, B. Kulesa, A. Shepherd, and N. Gourmelen (in press), Correction to “Ocean tides in the Weddell Sea: New observations on the Filchner-Ronne and Larsen C ice shelves and model validation”, *J. Geophys. Res.*, doi:10.1029/2011JC007463.
- Lewis, E. L., and R. G. Perkin (1986), Ice pumps and their rates, *J. Geophys. Res.-Ocean.*, *91*(C10), 11,756–11,762.

- Little, C. M., A. Gnanadesikan, and R. Hallberg (2008), Large-scale oceanographic constraints on the distribution of melting and freezing under ice shelves, *J. Phys. Oceanogr.*, *38*(10), 2242–2255.
- Little, C. M., A. Gnanadesikan, and M. Oppenheimer (2009), How ice shelf morphology controls basal melting, *J. Geophys. Res.*, *114*, C12007, doi:10.1029/2008JC005197.
- Little, C. M., D. Goldberg, A. Gnanadesikan, and M. Oppenheimer (2012), On the coupled response to ice shelf basal melting, *J. Glaciol.*, *58*(208), 203–215, doi:10.3189/2012JoG11J037.
- Loder, J. (1980), Topographic Rectification of tidal currents on the sides of Georges Bank, *J. Phys. Oceanogr.*, *10*(9), 1399–1416.
- Losch, M. (2008), Modeling ice shelf cavities in a z-coordinate ocean general circulation model, *J. Geophys. Res.-Ocean.*, *113*, C08043, doi:10.1029/2007JC004368.
- Luckman, A., L. Padman, and D. Jansen (2010), Persistent iceberg groundings in the western Weddell Sea, Antarctica, *Rem. Sens. Environ.*, *114*(2), 385–391, doi:10.1016/j.rse.2009.09.009.
- Lytche, M. B., D. G. Vaughan, and the BEDMAP Consortium (2001), BEDMAP: A new ice thickness and subglacial topographic model of Antarctica, *J. Geophys. Res.-Solid Earth.*, *106*, 11,335–11,351.
- MacAyeal, D. (1985a), Tidal rectification below the Ross Ice Shelf, Antarctica, in *Oceanology of the Antarctic Continental Shelves*, *Antarctic Research Series*, vol. 43, edited by S. Jacobs, pp. 133–144, American Geophysical Union, Washington, DC.

- MacAyeal, D. R. (1984), Thermohaline circulation below the Ross Ice Shelf: A consequence of tidally induced vertical mixing and basal melting, *J. Geophys. Res.*, *89*(C1), 597–606.
- MacAyeal, D. R. (1985b), Evolution of tidally triggered meltwater plumes below ice shelves, in *Oceanology of the Antarctic Continental Shelves, Antarctic Research Series*, vol. 43, edited by S. Jacobs, pp. 109–132, American Geophysical Union, Washington, DC.
- Mackensen, A. (2001), Oxygen and carbon stable isotope tracers of Weddell Sea water masses: new data and some paleoceanographic implications, *Deep Sea Res. I*, *48*(6), 1401–1422, doi:10.1016/S0967-0637(00)00093-5.
- Makinson, K. (2002), Modeling tidal current profiles and vertical mixing beneath Filchner-Ronne Ice Shelf, Antarctica, *J. Phys. Oceanogr.*, *32*(1), 202–215.
- Makinson, K., and K. Nicholls (1999), Modeling Tidal currents beneath Filchner-Ronne Ice Shelf and on the adjacent continental shelf: their effect on mixing and transport, *J. Geophys. Res.*, *104*(C6), 13,449–13,465.
- Makinson, K., M. Schröder, and S. Østerhus (2006), Effect of critical latitude and seasonal stratification on tidal current profiles along Ronne Ice Front, Antarctica, *J. Geophys. Res.-Ocean.*, *111*(C3), C03022, doi:10.1029/2005JC003062.
- Makinson, K., P. Holland, A. Jenkins, K. W. Nicholls, and D. M. Holland (2011), Influence of tides on melting and freezing beneath Filchner-Ronne Ice Shelf, Antarctica, *Geophys. Res. Lett.*, *38*, L06601, doi:10.1029/2010GL046462.
- Marchesiello, P., L. Debreu, and X. Couvelard (2009), Spurious diapycnal mixing in terrain-

- following coordinate models: The problem and a solution, *Ocean Modeling*, *26*, 156–169, doi:10.1016/j.ocemod.2008.09.004.
- Marshall, G. J., P. A. Stott, J. Turner, W. M. Connolley, J. C. King, and T. A. Lachlan-Cope (2004), Causes of exceptional atmospheric circulation changes in the southern hemisphere, *Geophysical Research Letters*, *31*(14), L14205, doi:10.1029/2004GL019952.
- McPhee, M. G. (1981), An analytic similarity theory for the planetary boundary layer stabilized by surface buoyancy, *Boundary-Layer Meteorology*, *21*, 325–339.
- McPhee, M. G. (1983), Turbulent heat and momentum transfer in the oceanic boundary layer under melting pack ice, *J. Geophys. Res.*, *88*, 2827–2835.
- McPhee, M. G. (1987), A time-dependent model for turbulent transfer in a stratified oceanic boundary-layer, *J. Geophys. Res.-Ocean.*, *92*(C7), 6977–6986.
- McPhee, M. G. (1992), Turbulent heat flux in the upper ocean under sea ice, *J. Geophys. Res.-Ocean.*, *97*(C4), 5365–5379.
- McPhee, M. G. (1999), Parameterization of mixing in the ocean boundary layer, *J. Mar. Sys.*, *21*(1-4), 55–65.
- McPhee, M. G. (2008), *Air-Ice-Ocean Interaction: Turbulent Ocean Boundary Layer Exchange Processes*, Springer Science + Business Media B.V.
- McPhee, M. G., and J. D. Smith (1976), Measurements of the turbulent boundary layer under pack ice, *J. Phys. Oceanogr.*, *6*, 696–711.

- McPhee, M. G., G. A. Maykut, and J. H. Morison (1987), Dynamics and thermodynamics of the ice/upper ocean system in the marginal ice zone of the Greenland Sea, *J. Geophys. Res.-Ocean.*, *92*(C7), 7017–7031.
- McPhee, M. G., C. Kottmeier, and J. H. Morrison (1999), Ocean Heat Flux in the Central Weddell Sea during Winter, *J. Phys. Oceanogr.*, *29*, 1166–1179.
- McPhee, M. G., T. Kikuchi, J. H. Morison, and T. P. Stanton (2003), Ocean-to-ice heat flux at the north pole environmental observatory, *Geophys. Res. Lett.*, *30*(24), 2274, doi:10.1029/2003GL018580.
- McPhee, M. G., J. H. Morison, and F. Nilsen (2008), Revisiting heat and salt exchange at the ice-ocean interface: Ocean flux and modeling considerations, *J. Geophys. Res.-Ocean.*, *113*, C06014, doi:10.1029/2007JC004383.
- Mellor, G., and T. Yamada (1974), A hierarchy of turbulence closure models for planetary boundary layers, *J. Atmos. Sci.*, *13*, 1791–1806.
- Mellor, G., and T. Yamada (1982), Development of a turbulence closure model for geophysical fluid problems, *Rev. Geophys.*, *20*, 851–875.
- Middleton, J., T. Foster, and A. Foldvik (1987), Diurnal shelf waves in the southern Weddell Sea, *J. Phys. Oceanogr.*, *17*, 784–791.
- Millero, F. J. (1978), *Annex 6: Freezing point of seawater. Eighth report of the Joint Panel of Oceanographic Tables and Standards*, pp. 29–31, no. 28 in UNESCO Marine Science Tech. Paper, UNESCO.

- Moholdt, G., L. Padman, and H. Fricker (in review), Basal mass budget of Ross and Filchner-Ronne ice shelves, Antarctica, derived from Lagrangian analysis of ICESat altimetry, *J. Geophys. Res.*
- Morris, E. M., and D. G. Vaughan (2003), Spatial and temporal variation of surface temperature on the antarctic peninsula and the limit of viability of ice shelves, in *Antarctic Peninsula Climate Variability: Historical and Paleoenvironmental Perspectives*, *Antarctic Research Series*, vol. 79, edited by E. Domack, A. Leventer, A. Burnett, R. Bindshadler, P. Convey, and M. Kirby, pp. 61–68, American Geophysical Union, Washington, DC.
- Motyka, R., M. Truffer, M. Fahnestock, J. Mortensen, S. Rysgaard, and I. Howat (2011), Submarine melting of the 1985 Jakobshavn Isbræ floating tongue and the triggering of the current retreat, *J. Geophys. Res.*, *116*, F01007, doi:10.1029/2009JF001632.
- Motyka, R., L. Hunter, K. Echelmeyer, and C. Connor (2003), Submarine melting at the terminus of a temperate tidewater glacier, LeConte Glacier, Alaska, USA, in *Ann. Glaciol.*, vol. 36, edited by Raymond, CF, pp. 57–65, International Glaciological Society.
- Mueller, R. D., L. Padman, M. S. Dinniman, S. Y. Erofeeva, H. A. Fricker, and M. A. King (2012), Impact of tide-topography interactions on basal melting of Larsen C Ice Shelf, Antarctica, *J. Geophys. Res.*, *117*, C05005, doi:10.1029/2011JC007263.
- Nicholls, K. W., K. Makinson, and M. R. Johnson (1997), New oceanographic data from beneath Ronne Ice Shelf, Antarctica, *Geophys. Res. Lett.*, *24*(2), 167–170.
- Nicholls, K. W., S. Østerhus, K. Makinson, and M. R. Johnson (2001), Oceanographic

- conditions south of Berkner Island, beneath Filchner-Ronne Ice Shelf, Antarctica, *J. Geophys. Res.-Ocean.*, *106*(C6), 11,481–11,492.
- Nicholls, K. W., L. Padman, M. Schröder, R. A. Woodgate, A. Jenkins, and S. Østerhus (2003), Water Mass Modification Over the Continental Shelf North of Ronne Ice Shelf, Antarctica, *J. Geophys. Res.-Ocean.*, *108*(C8), 3260.
- Nicholls, K. W., C. J. Pudsey, and P. Morris (2004), Summertime water masses off the northern Larsen C Ice Shelf, Antarctica, *Geophys. Res. Lett.*, *31*, L09309, doi:10.1029/2004GL019924.
- Nicholls, K. W., L. Boehme, M. Biuw, and M. A. Fedak (2008), Wintertime ocean conditions over the southern Weddell Sea continental shelf, Antarctica, *Geophys. Res. Lett.*, *35*, L21605, doi:10.1029/2008GL035742.
- Nicholls, K. W., S. Østerhus, K. Makinson, and G. T. (2009), Ice-ocean processes over the continental shelf of the southern Weddell Sea, Antarctica: A review, *Rev. Geophys.*, *47*, RG3003, doi:10.1029/2007RG000250.
- Nicholls, K. W., K. Makinson, and E. J. Venables (2012), Ocean circulation beneath larsen c ice shelf, antarctica from in situ observations, *Geophysical Research Letters*, *39*(19), L19608, doi:10.1029/2012GL053187.
- Notz, D., M. G. McPhee, M. G. Worster, G. A. Maykut, K. H. Schlünzen, and H. Eicken (2003), Impact of underwater-ice evolution on Arctic summer sea ice, *J. Geophys. Res.*, *108*(C7), 3223, doi:10.1029/2001JC001173.

- Orr, A., G. J. Marshall, J. C. R. Hunt, J. Sommeria, C.-G. Wang, N. P. M. van Lipzig, D. Cresswell, and J. C. King (2008), Characteristics of summer airflow over the Antarctic Peninsula in response to recent strengthening of westerly circumpolar winds, *Journal of the Atmospheric Sciences*, *65*(4), 1396–1413, doi:{10.1175/2007JAS2498.1}.
- Orsi, A. H., W. D. Nowlin, and T. Whitworth (1993), On the circulation and stratification of the Weddell Gyre, *Deep Sea Res. I*, *40*, 169–203, doi:10.1016/0967-0637(93)90060-G.
- Owen, P. R., and W. R. Thomson (1963), Heat transfer across rough surfaces, *J. Fluid. Mech.*, *15*, 321–334.
- Padman, L., and C. Kottmeier (2000), High-frequency ice motion and divergence in the Weddell Sea, *J. Geophys. Res.-Ocean.*, *105*(C2), 3379–3400.
- Padman, L., A. J. Plueddemann, R. D. Muench, and R. Pinkel (1992), Diurnal tides near the Yermak Plateau, *J. Geophys. Res.*, *97*(C8), 12,639–12,652.
- Padman, L., H. A. Fricker, R. Coleman, S. Howard, and S. Erofeeva (2002), A new tidal model for the Antarctic ice shelves and seas, *J. Glaciol.*, *34*, 247–254.
- Padman, L., M. King, D. Goring, H. Corr, and R. Coleman (2003), Ice shelf elevation changes due to atmospheric pressure variations, *J. Glaciol.*, *49*(167), 521–526.
- Padman, L., S. Y. Erofeeva, and H. A. Fricker (2008), Improving Antarctic tide models by assimilation of ICESat laser altimetry over ice shelves, *Geophys. Res. Lett.*, *35*, L22504, doi:10.1029/2008GL035592.
- Padman, L., S. L. Howard, A. H. Orsi, and R. D. Muench (2009), Tides of the northwestern

- Ross Sea and their impact on dense outflows of Antarctic Bottom Water, *Deep Sea Res. II*, 56(13-14), 818–834, doi:10.1016/j.dsr2.2008.10.026.
- Pavlis, N. K., S. A. Holmes, S. C. Kenyon, and J. K. Factor (2008), An earth gravitational model to degree 2160: EGM2008, in *General Assembly of the European Geosciences Union*, Vienna, Austria.
- Payne, A., A. Vieli, A. Shepherd, D. Wingham, and E. Rignot (2004), Recent dramatic thinning of largest West Antarctic ice stream triggered by oceans, *Geophys. Res. Lett.*, 31(23), L23401, doi:{10.1029/2004GL021284}.
- Payne, A. J., P. R. Holland, A. P. Shepherd, I. C. Rutt, A. Jenkins, and I. Joughin (2007), Numerical modeling of ocean-ice interactions under Pine Island Bay's ice shelf, *J. Geophys. Res.-Ocean.*, 112(C10), C10019, doi:10.1029/2006JC003733.
- Pollard, D., and R. M. DeConto (2009), Modelling West Antarctic ice sheet growth and collapse through the past five million years, *Nature*, 458, 329–332, doi:10.1038/nature07809.
- Potter, J., and J. Paren (1985), Interaction between ice shelf and ocean in George VI Sound, Antarctica, *Antarctic Research Series*, 43, 35–58.
- Pritchard, H. D., S. R. M. Ligtenberg, H. A. Fricker, D. G. Vaughan, M. R. van den Broeke, and L. Padman (2012), Antarctic ice-sheet loss driven by basal melting of ice shelves, *Nature*, 484, 502–505, doi:10.1038/nature10968.
- Rignot, E., and S. S. Jacobs (2002), Rapid bottom melting widespread near Antarctic Ice Sheet grounding lines, *Science*, 296(5575), 2020–2023, doi:10.1126/science.1070942.

- Rignot, E., and K. Steffen (2008), Channelized bottom melting and stability of floating ice shelves, *Geophys. Res. Lett.*, *35*(2), doi:10.1029/2007GL031765.
- Rignot, E., G. Casassa, P. Gogineni, W. Krabill, A. Rivera, and R. Thomas (2004), Accelerated ice discharge from the Antarctic Peninsula following the collapse of Larsen B Ice Shelf, *Geophys. Res. Lett.*, *31*, L18401.
- Rignot, E., J. L. Bamber, M. R. Van Den Broeke, C. Davis, Y. H. Li, W. J. Van De Berg, and E. Van Meijgaard (2008), Recent Antarctic ice mass loss from radar interferometry and regional climate modelling, *Nat. Geo.*, *1*(2), 106–110.
- Rignot, E., J. Mouginot, and B. Scheuchl (2011), Antarctic grounding line mapping from differential satellite radar interferometry, *Geophys. Res. Lett.*, *38*, L10504, doi:10.1029/2011GL047109.
- Rignot, E., J. Mouginot, and B. Scheuchl (2013), Ice-shelf melting around Antarctica, *Science*, *341*(6143), 266–270, doi:10.1126/science.1235798.
- Rignot, E., M. Koppes, and I. Velicogna (2010), Rapid submarine melting of the calving faces of West Greenland glaciers, *Nature Geosciences*, *3*(3), 187–191, doi:10.1038/NGEO765.
- Robertson, R., L. Padman, and G. Egbert (1998), Tides in the Weddell Sea, in *Oceanology of the Antarctic Continental Shelf*, *Antarctic Research Series*, vol. 75, edited by S. Jacobs and R. Weiss, American Geophysical Union, Washington, DC.
- Robertson, R., M. Visbeck, A. L. Gordon, and E. Fahrbach (2001), Internal tides and baro-

- clnicity in the Southern Weddell Sea 2. Effects of the critical latitude and stratification, *J. Geophys. Res.*, *106*(C11), 27,017–27,034.
- Robertson, R., M. Visbeck, A. L. Gordon, and E. Fahrbach (2002), Long-term temperature trends in the deep waters of the weddell sea, *Deep Sea Res. II*, *49*(21), 4791–4806.
- Robinson, I. (1981), Tidal vorticity and residual circulation, *Deep Sea Res.*, *28a*(3), 195–212.
- Robinson, N., M. Williams, P. Barrett, and A. Pyne (2010), Observations of flow and ice-ocean interaction beneath the McMurdo Ice Shelf, Antarctica, *J. Geophys. Res.*, *115*, C03,025, doi:10.1029/2008JC005255.
- Scambos, T., C. Hulbe, and M. Fahnestock (2004a), Climate-induced ice shelf disintegration in the Antarctic Peninsula, in *Antarctic Peninsula Climate Variability: Historical and Paleoenvironmental Perspectives*, edited by E. Domack, A. Laventer, A. Burnett, R. Bindshadler, P. Convey, and M. Kirby, pp. 79–92, American Geophysical Union.
- Scambos, T. A., J. A. Bohlander, C. A. Shuman, and P. Skvarca (2004b), Glacier acceleration and thinning after ice shelf collapse in the Larsen B embayment, Antarctica, *Geophys. Res. Lett.*, *31*, L18402, doi:10.1029/2004GL020670.
- Scambos, T. A., T. M. Haran, M. A. Fahnestock, T. H. Painter, and J. Bohlander (2007), MODIS-based Mosaic of Antarctica (MOA) data sets: Continent-wide surface morphology and snow grain size, *Remote Sensing of Environment*, *111*(2-3), 242–257.
- Schlosser, P., R. Bayer, A. Foldvik, T. Gammelsrød, G. Rohardt, and K. Otto Münnich (1990), Oxygen 18 and Helium as tracers of ice shelf water and water/ice interaction in the Weddell Sea, *J. Geophys. Res.*, *95*(C3), 3253–3263.

- Schmidt, G. A., C. M. Bitz, U. Mikolajewicz, and L. B. Tremblay (2004), Ice-ocean boundary conditions for coupled models, *Ocean Modeling*, *7*(1-2), 59–74.
- Shaw, W. J., T. P. Stanton, M. G. McPhee, and T. Kikuchi (2008), Estimates of surface roughness length in heterogeneous under-ice boundary layers, *J. Geophys. Res.*, *113*(C08030).
- Shchepetkin, A. F., and J. C. McWilliams (2003), A method for computing horizontal pressure-gradient force in an oceanic model with a nonaligned vertical coordinate, *J. Geophys. Res.-Ocean.*, *108*(C3), doi:10.1029/2001JC001047.
- Shchepetkin, A. F., and J. C. McWilliams (2009), Correction and commentary for “Ocean forecasting in terrain-following coordinates: Formulation and skill assessment of the regional ocean modeling system” by Haidvogel et al., *J. Comp. Phys.* *227*, pp. 3595–3624), *J. Comp. Phys.*, *228*(24), 8985–9000, doi:10.1016/j.jcp.2009.09.002.
- Shepherd, A., D. Wingham, T. Payne, and P. Skvarca (2003), Larsen Ice Shelf has progressively thinned, *Science*, *302*(5646), 856–859, doi:10.1126/science.1089768.
- Shepherd, A., D. Wingham, T. Payne, and P. Skvarca (2004), Correction and clarification to “Larsen Ice Shelf has progressively thinned”, *Science*, *303*(5664), 1612, doi:10.1126/science.303.5664.1612b.
- Sirevaag, A. (2009), Turbulent exchange coefficients for the ice/ocean interface in case of rapid melting, *Geophys. Res. Lett.*, *36*, L04606, doi:10.1029/2008GL036587.
- Skvarca, P., W. Rack, H. Rott, and T. I. Y. Donangelo (1998), Evidence of recent climatic

- warming on the Eastern Antarctic Peninsula, in *Ann. Glaciol.*, vol. 27, edited by W. Budd, pp. 628–632, International Glaciological Society.
- Skvarca, P., W. Rack, H. Rott, and T. I. Y. Donangelo (1999), Climatic trend and the retreat and disintegration of ice shelves on the Antarctic Peninsula: an overview, *Polar Res.*, 18, 151–157.
- Smith, W. H. F., and D. T. Sandwell (1997), Global seafloor topography from satellite altimetry and ship depth soundings, *Science*, 277, 1957–1962, doi:10.1126/science.277.5334.1956.
- Stanton, T. P., W. J. Shaw, M. Truffer, H. F. J. Corr, L. E. Peters, K. L. Riverman, R. Bindshadler, D. M. Holland, and S. Anandakrishan (2013), Channelized ice melting in the ocean boundary layer beneath pine island glacier, antarctica, *Science*, 341, 1236–1239, doi:10.1126/science.1239373.
- Suginohara, N., S. Aoki, and M. Fukasawa (1991), Comments on “On the importance of vertical resolution in certain oceanic general circulation models”, *J. Phys. Oceanogr.*, 21(11), 1699–1701.
- Thompson, D. W. J., and S. Solomon (2002), Interpretation of recent southern hemisphere climate change, *Science*, 296(5569), 895–899, doi:10.1126/science.1069270.
- Thompson, D. W. J., S. Solomon, P. J. Kushner, M. H. England, K. M. Grise, and D. J. Karoly (2011), Signatures of the antarctic ozone hole in southern hemisphere surface climate change, *Nat. Geo.*, 4(11), 741–749, doi:10.1038/ngeo1296.

- Thomson, R. E., and W. A. Crawford (1982), The generation of diurnal period shelf waves by tidal currents, *J. Geophys. Res.*, *12*, 635–643.
- Timmermann, R., et al. (2010), A consistent dataset of Antarctic ice sheet topography, cavity geometry, and global bathymetry, *Earth System Science Data*, *2*, 261–273, doi:doi:10.5194/essd-2-261-2010.
- Timmermann, R., Q. Wang, and H. H. Hellmer (2012), Ice-shelf basal melting in a global finite-element sea-ice/ice-shelf/ocean model, *Ann. Glaciol.*, *53*(60), 303–314, doi:doi:10.3189/2012AoG60A156.
- van de Berg, W., M. van den Broeke, C. Reijmer, and E. van Meijgaard (2006), Reassessment of the Antarctic surface mass balance using calibrated output of a regional atmospheric climate model, *J. Geophys. Res.*, *111*, D11104, doi:10.1029/2005JD006495.
- van den Broeke, M., W. J. van de Berg, and E. van Meijgaard (2008), Firn depth correction along the Antarctic grounding line, *Antarct. Sci.*, *20*, 513–517, doi:10.1017/S095410200800148X.
- Vaughan, D. G., and C. S. M. Doake (1996), Recent atmospheric warming and retreat of ice shelves on the Antarctic Peninsula, *Nature*, *379*, 328–331.
- Vaughan, D. G., D. K. A. Barnes, P. T. Fretwell, and R. G. Bingham (2011), Potential seaways across west antarctica, *Geochemistry, Geophysics, Geosystems*, *12*(10), n/a–n/a, doi:10.1029/2011GC003688.
- Vieli, A., A. J. Payne, A. Shepherd, and Z. Du (2007), Causes of pre-collapse changes of the

- Larsen B ice shelf: Numerical modelling and assimilation of satellite observations, *Earth Planet. Sci. Lett.*, 259(3-4), 297–306, doi:10.1016/j.epsl.2007.04.050.
- von Kármán, T. (1930), “Mechanische Ähnlichkeit und Turbulenz”, Nachrichten von der Gesellschaft der Wissenschaften zu Göttingen, Fachgruppe 1, *Mathematik*, 5, 58–76.
- Weaver, A., and E. Sarachik (1991), Reply, *J. Phys. Oceanogr.*, 21(11), 1702–1707.
- Weaver, A. J., and E. S. Sarachik (1990), On the importance of vertical resolution in certain ocean general circulation models, *J. Phys. Oceanogr.*, 20(4), 600–609.
- Yaglom, A. M., and B. A. Kader (1974), Heat and mass transfer between a rough wall and turbulent fluid flow at high Reynolds and Peclet numbers, *J. Fluid. Mech.*, 62(03), 601–623.
- Zwally, H. J., M. B. Giovinetto, J. Li, H. G. Cornejo, M. A. Beckley, A. C. Brenner, J. L. Saba, and D. Yi (2005), Mass changes of the Greenland and Antarctic ice sheets and shelves and contributions to sea-level rise: 1992–2002., *J. Glaciol.*, 51, 509–527, doi: 10.3189/172756505781829007.